NORTHWESTERN UNIVERSITY

Quantitative Analysis of Complex Three-Dimensional Microstructures

A DISSERTATION

SUBMITTED TO THE GRADUATE SCHOOL

IN PARTIAL FULFILLMENT OF THE REQUIREMENTS

for the degree

DOCTOR OF PHILOSOPHY

Field of Materials Science and Engineering

By

Amber Lynn Genau

EVANSTON, ILLINOIS

December 2008

ABSTRACT

Quantitative Analysis of Complex Three-Dimensional Microstructures

Amber Lynn Genau

The morphological evolution due to coarsening is analyzed for two distinctive types of microstructure. First, the feasibility of characterizing spatial correlations of interfacial curvature in topologically complex structures is demonstrated with the analysis of bicontinuous two-phase mixtures produced using phase field modeling. For structures produced with both conserved and nonconserved dynamics, new characteristic length scales are identified. In the nonconserved case, despite the local evolution law governing interfacial motion, long-range correlations develop that lead to a characteristic length scale associated with the distance between high curvature tunnels. In the conserved case the diffusional dynamics leads to a length scale that is related to correlations and anticorrelations between regions of curvature of opposite sign. Positive correlations due to this length scale can be measured out to seven times the characteristic length of the system. Spatial correlations are also compared for symmetric and asymmetric mixtures produced with conserved dynamics.

In addition, the microstructure of directionally solidified and isothermally coarsened Pb-Sn samples are examined at various coarsening times. The samples, composed of Pb-69.1wt%Sn, have an overall volume fraction of 22% solid which is not uniformly distributed through the sample but clustered into regions of approximately 37% solid separated by empty eutectic regions. The morphology of the dendrites, both in the dense regions and at the edge of the eutectic spaces is analyzed using three-dimensional reconstructions, Interface Shape Distributions and Interface Normal Distributions. These methods are used to track the evolution of the structures from being dominated by secondary and tertiary arms in the plane perpendicular to the solidification direction to predominance of the primary stalks running in the solidification direction.

Finally, the method of characterizing spatial correlations introduced above is applied to the experimentally obtained dendritic structures. For these samples, changes to the correlations are found due to increased coarsening time, changes in volume fraction, and whether the sample comes from a dense or non-dense region. This technique proves to be a method of broad applicability that has the potential to unlock valuable details about a variety of different systems and phenomena.

Acknowledgements

Tremendous thanks to my advisor, Prof. Peter Voorhees. It is remarkable how much I have learned working with him over the last four years. I am continually astonished by the depth and breadth of his knowledge. He is a conscientious researcher and highly dedicated to the success of his students. It has been a privilege to work with such an outstanding person and scholar. I only regret not being able to experience him in his full splendor as a non-department chair advisor.

I would like to thank my committee members from Northwestern: Professors Ken Shull and Greg Olson, for their critiques and suggestions, and for their willingness to share their expertise. Thanks to my outside committee member, Iver Anderson of Iowa State University and Ames Lab. I am so pleased that he could continue to be part of my graduate studies. I would also like to express my most sincere gratitude to Peggy Adamson, without whom my time at Northwestern would have been a much stormier place.

I am indebted to all Voorhees group members, past and present, with whom I have interacted: Dimitris, Yongwoo, Roberto, Dave, Katsuyo, Jian, Julie, Megna, Ian, Eddie, Larry, Guru, Susan, Kuo-an and Brad. I am particularly grateful to Dimitris for teaching me everything I know about the experimental setup, and modeling the best kind of mentoring. I couldn't have had a better teacher. Yongwoo, once roused, was also unfailingly helpful and patient with my questions. I don't think Megna will ever understand how

much I have appreciated her good advice and common sense. (She may appreciate how glad I was to have someone to turn to and check, "Did he really just say that?") Thanks to Larry for his help preparing the samples last summer. Memories of the swager will always keep us together. I am so grateful that Dave and Roberto were willing and able to maintain their ties with the group even after they left Northwestern. My research experience would have been far less productive without their help and continuing availability. I am also grateful to Katsuyo for her help on the paper. Her incredible work ethic and meticulous attention to detail inspire me to a higher standard.

A special thank you to everyone who listened to my meltdowns and convinced me that it probably wasn't quite time to run away and join the circus, although I could if I really wanted to. I can't imagine a better set of classmates and friends. I would never have gotten through the CORE courses without you all. And to the gentlemen of the Waldorf: thank you for letting me stay in your extra bedroom. It was fun.

Thank you to my parents, my first and most enthusiastic supporters. I appreciate more every day that I would not be where I am without you. Thanks to Joe, who was rooting for graduate school in Chicago from the beginning. I am so grateful for your patience, yet again. Your support, love and sense of humor make my life a better place.

Finally, I would like to express my thanks to NASA for continuing the CSLM-2 project, despite the many setbacks along the way. It was an adventure to work with the agency and its people, and I am pleased to have been able to do so. This work was supported by NASA under Grant No. NNX07-AW01G.

Contents

List of Figures

List of Tables

CHAPTER 1

Introduction

Although we have always lived in a three-dimensional world, materials science has only recently entered the three-dimensional realm. It is within the last two decades that the techniques for acquiring 3D images, and the computing power necessary to handle the vast quantities of resulting data, have been available, making 3D analysis practical or even possible. This advance has opened up new possibilities for exploring the many natural structures of extraordinary morphological and topological complexity which require a fully three-dimensional analysis. If we are to take full advantage of the explosion in the availability of 3D data, new methods of quantifying complex structures are necessary.

One type of such a complex structure is composed of two or more interconnected domains and posses spatially varying interfacial curvature. Examples of such structures include trabecular bone [**1**], two-phase mixtures produced following spinodal decomposition [**2**], ordering in ferromagnetic materials [**3**,**4**], solid-liquid mixtures following dendritic solidification [**5**], solid-oxide fuel cells [**6**,**7**], and phase separation in polymer blends [**8**,**9**]. The morphology of the interfaces in these structures plays a major role in setting their unique properties. The topology and morphology of the tribeculae contribute to the mechanical properties of bone [**10**]. The morphology of bicontinuous structures may play an important role in improving the efficiencies of organic solar cells [**11**]. The ease with which gas flows through solid-oxide fuel cells is strongly related to the morphology of the pores in these structures [**12**]. Similarly, fluid flow through dendritic solid-liquid mixtures

is connected with the morphology of the two-phase mixture and hence the presence of deleterious casting defects.

In past these structures have been characterized using a two-point correlation function or its Fourier transform, the structure function [**2**], which can be determined from x-ray analysis. This provides some information on the structure, but a measure in Fourier space cannot provide an accurate picture of the interfacial morphology. One recently developed method for partially determining the morphology of these structures is called the Interface Shape Distribution (ISD) [**1**, **13**, **14**], which is determined by measuring the probability of finding a patch of interface with a certain mean and Gaussian curvature. The ISD is the counterpart to particle size distributions for systems consisting of spherical particles embedded in a matrix. Another measurement is the Interface Normal Distribution (IND) [**14**], which determines directionality of a structure. The topology of these systems have been characterized by measures such as the Genus, Euler characteristic, and Betti numbers [**8**, **15**–**17**].

However, these works provide only a partial picture of the structure of these morphologically complicated systems since the manner in which the interfacial curvatures are distributed spatially in the system is unknown. In particular, it is possible for two structures to have the same interface shape distribution, but to have the curvatures distributed differently in space. Moreover, in many cases interfacial curvature itself drives the evolution of the structure. For example, in a two-phase system the chemical potential is a function of the local mean curvature, so the spatial distribution of the mean curvature can provide important information on the manner in which the structure evolves.

Thus an important piece of information is missing that is needed to both characterize the morphology of the interfaces and, in some cases, predict its evolution.

The spatial correlation of spherical (or assumed spherical) particles has been directly measured in two dimensional systems [**18**,**19**] and on planar slices taken from three dimensional systems [**20**, **21**]. The 2D techniques have also been extended to obtain correlation data about fibers [**22**] and non-spherical particulate matter [**23**]. Spatial correlation information can also be extracted from three-dimensional systems using x-ray or other scattering data via the structure function [**24**, **25**], but as mentioned above, this is an indirect measurement requiring a number of assumptions such as particle shape and the particle size distribution. In addition, a few studies have measured three-dimensional correlations in real space using confocal microscopy [**26**] and simulated particle systems [**27**–**29**]. I will present a new method which I have developed that can be used to quantify the spatial distribution of interfacial curvature in systems of any morphology and topology by calculating the radial distribution function (RDF).

An excellent example of the usefulness of quantifying complex microstructures is the field of coarsening. Coarsening is a widespread phenomenon which occurs in nearly all two phase systems, whether metal, ceramic or polymer, and in solids, liquids and gases. Driven by the desire to reduce the excess free energy associated with interfacial area, the system works to decrease the amount of interface, resulting in an increasing length scale within the system. The evolution of the microstructure during coarsening is highly dependent on both the type of curvature present (measured by ISD) and the arrangement of that curvature (measured by RDF).

In the first section, I will examine the spatial correlations of bicontinuous structures produced following phase separation by spinodal decomposition and phase ordering, in particular focusing on the late-stages of the transformations, or coarsening regime, where the interfaces are well developed and the structures are evolving under the influence of interfacial energy. During phase ordering, the order parameter, whose value changes from one phase to another, is not conserved, whereas during spinodal decomposition the order parameter is conserved. This critical difference leads to markedly different spatial distributions in the mean curvature of the system. In the second section, I will apply this method of analyzing spatial distributions to examine the differences between symmetric and asymmetric two-phase mixtures produced using conserved kinetics.

This work was done in conjunction with NASA and the Coarsening in Solid-Liquid Mixtures 2 project, which studies coarsening of spherical particles in liquid in the microgravity environment of the international Space Station. The microgravity environment avoids material transport effects due to sedimentation or convection currents, allowing the fundamental aspects of coarsening to be probed, particularly the assumptions of LSW Theory (discussed further in Chapter 2). Lead-tin was chosen as a model system because of its isotropic interfacial energy, well known parameters and fast coarsening rate. While the CSLM-2 project is ongoing, it did not proceed on a time-scale conducive to inclusion in this dissertation, particularly because of lingering delays after the crash of the space shuttle Columbia. Therefore, in order to supplement the work being done in microgravity, an experimental component was developed which could be carried out on the ground. Using the same Pb-Sn system and many of the same techniques and equipment, directionally solidified dendrites were isothermally coarsened and analyzed using ISDs, INDs

and RDFs. The structural nature of dendrites makes it possible to coarsen them without significant gravity-induced sedimentation, at least within a range of volume fractions and coarsening times.

Dendritic coarsening is an area of particular technological importance, because dendrites form in all metal alloys, and the coarsening of these structures, both in the mushy zone during solidification and potentially afterwards while the part is in service, has a significant impact on the properties of the metal. In the third section, I particularly look at dendrites grown in systems with a low volume fraction of solid, allowing individual dendrites to develop more fully. The fourth section I will examine the patterns of spatial correlations of dendritic samples, looking at the correlations change with volume fraction solid and coarsening time. An improved understanding of coarsening and its effect on microstructure will help us better exploit the link between processing and structure, tailoring the properties of a material to fit specific needs.

CHAPTER 2

Coarsening

2.1. Coarsening in Systems with Spherical Particles

For the simplest systems, specifically two phase systems with spherical particles, coarsening, also known as Ostwald ripening, is quite well understood. In an attempt to minimize surface energy in such a system, small spheres shrink while large spheres grow, maintaining a nearly constant volume of the second phase while decreasing the surface area to volume ratio. Over time, the average particle radius increases, while the number density of particles decreases. This process is facilitated by the Gibbs-Thomson effect, the dependence of equilibrium concentration at an interface on the mean curvature, H, of that interface. The equilibrium composition of the liquid at any point along the interface is given by the Gibbs-Thompson equation as

$$C_L = C_\infty + \Gamma H \tag{2.1}$$

where C_L is the composition in the liquid, C_∞ is the equilibrium composition of the liquid at a flat interface, Γ is the capillary length (determined by the material parameters including solid-liquid interface energy), and the mean curvature of the interface is equal to

$$H = \frac{1}{2}\left(\frac{1}{R_1} + \frac{1}{R_2}\right) \tag{2.2}$$

where R_1 and R_2 are the maximum and minimum radii of curvature, respectively. Because of this composition dependence, the concentration of solute atoms near a small particle (with high curvature) will be relatively high, while the concentration near a larger particle (with lower curvature) will be relatively lower. This concentration gradient causes mass to diffuse from the small particle to the larger particle, with the large particle growing and the small particle shrinking until it disappears.

Coarsening of spherical structures can therefore be described by only one variable, the radius of the spheres. Lifshitz and Slyozov [**30**] and Wagner [**31**] developed a theory in 1961 for the coarsening of a polydisperse array of particles embedded in a matrix which effectively predicts the growth rate of the average particle size. They predicted that

$$\bar{R}^3(t) - \bar{R}^3(0) = K_{LSW}t \tag{2.3}$$

where $\bar{R}$ is the average particle radius at some time, t, and K_{LSW} is the rate constant

$$K_{LSW} = \frac{8T_0\Gamma D}{9M_L(C_S - C_L)} \tag{2.4}$$

with T_0 the coarsening temperature, Γ again the capillary length, D the diffusion coefficient, M_L the slope of the liquidus curve, and C_S and C_L the compositions of the solid and liquid at a flat interface. LSW theory assumes infinitely separated particles, i.e., that the volume of the particles is negligible so that there is no overlapping of diffusion fields, and that the interfacial free energy is isotropic (producing spherical particles). Equation 2.3 also predicts the condition of self-similarity, meaning that the microstructure appears the same as it coarsens except for a scaling factor (i.e., time-independent when scaled by a time-dependent characteristic length).

2.2. Coarsening of Dendrites

Unfortunately, most real systems do not present simple spherical particles. Metal alloys, for example, usually solidify by forming dendrites, complicated tree-like structures with secondary, tertiary and sometimes higher order branches. After solidification initiates, minute variations develop in the progressing solid-liquid interface. Thermodynamics drives these perturbations to quickly grow into cellular and then dendritic morphologies. Between the tips and the bases of the dendrites is a region of solid plus liquid, known as the mushy zone, where coarsening occurs. This occurs under nearly isothermal conditions.

Dendrite surfaces present a complex curvature which can be either positively or negatively curved, and which are no longer related to the size of the particle. The varying curvatures set up concentration gradients in the liquid, which cause a flux of solute and drive the evolution of the morphology. Although the concentration at the interface is determined by the curvature of the local interface, the velocity of the interface at any given point is determined by long-range diffusive interactions with surrounding regions. The effects of this nonlocal dependence on coarsening dynamics are not yet well understood.

The first description of dendrite coarsening was put forth by Papapetrou in 1935 [**32**], and initially it was studied by looking at the secondary dendrite arm spacing. While providing useful information about the evolution of the structure, this method has several significant shortcomings, namely the inherent difficulties in extracting information about three-dimensional objects from a two-dimensional measurement, and the problem of evolution to the point where the dendrites become spherical and there are no arms to measure. Most models of the mushy zone have generally simplified dendrites to a collection of cylinders [**33**–**37**] or tear-drop shaped arms [**38**, **39**]. This allows the curvature of

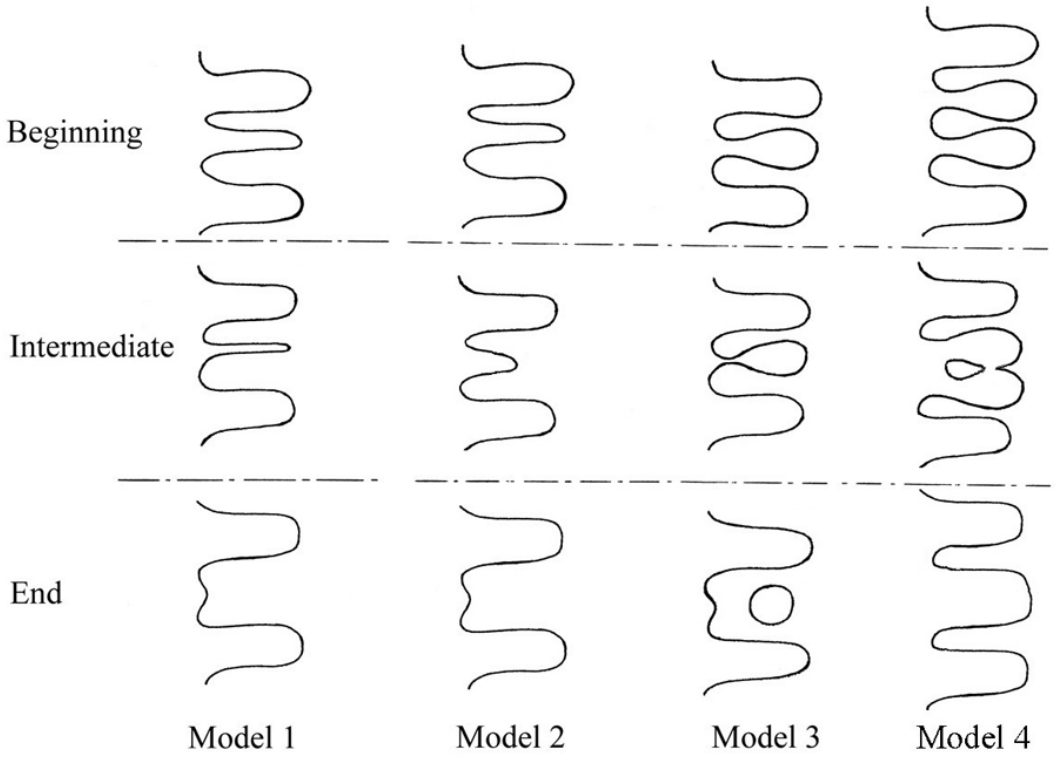

Figure 2.1. Four different models for isothermal corasening: (1) radial remelting, (2) axial remelting, (3) arm detachment, and (4) arm coalescence.

the interface to be once again linked with size. Kattamis *et al.* [**40**] proposed methods for both shapes. The first describes a situation in which a cylindrical arm, thinner than the surrounding arms and therefore with a lower melting point, will decrease in radius until it has melted away, leading to an increase in average spacing. For the second case, Kattamis proposed a model in which a tear-drop shaped arm between two cylindrical arms will decrease in radius at its base until it pinches off entirely as mass is transported from the base of the arm to the tip. Alternatively, Kahlweit approximates dendrite arms as cylinders with spherical tips [**33**] which melt back from the tips instead of radially. Young and Kirkwood [**39**] propose that the the method of coarsening is coalescence rather than

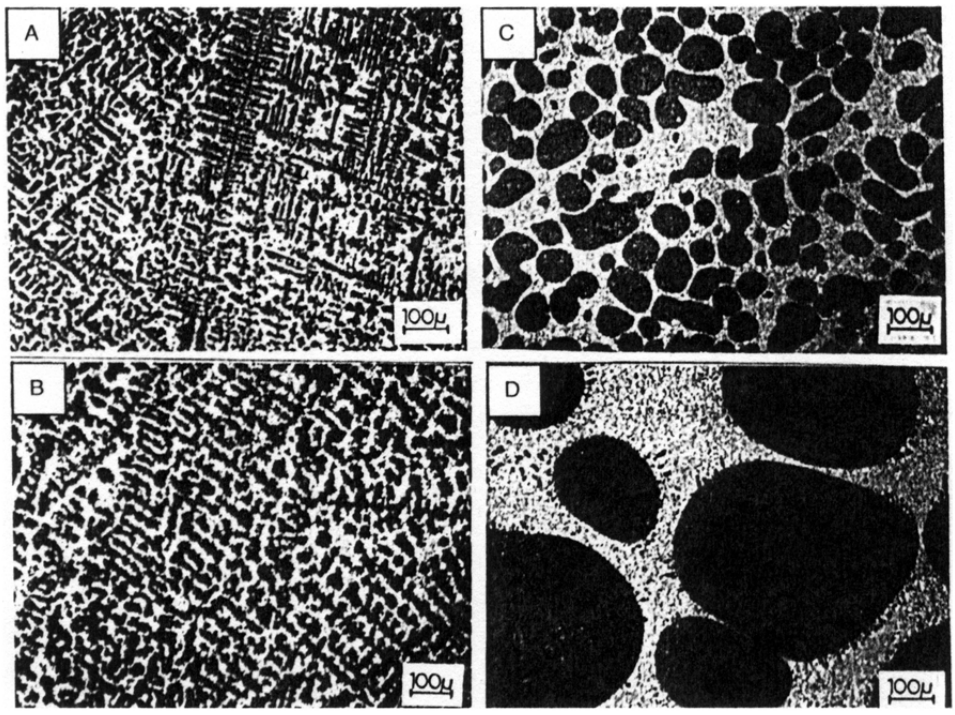

Figure 2.2. Micrographs showing the coarsening of Sn-$wt\%$40Bi for (a) $t = 0$, (b) $t = 10min$, (c) $t = 2.5hr$, (d) $t = 240hr$.

melting. According to their calculations, the curvature between dendrite arms will cause initially cylindrical arms to become tear-drop shaped and impinge on one another near the tips, causing coalescence. These four methods are shown schematically in Figure 2.1. Experimental evidence suggests that each of these methods is possible to some extent, depending on circumstances.

By measuring secondary dendrite arm spacing, researchers were able to determine that dendrite coarsening follows the same power law observed in spherical particle systems and spinodal decomposition of alloys, namely $\lambda_2 \sim t_f^{1/3}$, where λ_2 is the secondary dendrite arm spacing and t_f is the local solidification time. While measuring λ_2 is clearly

a useful measure, it has significant shortcomings, such as those faced by Marsh and Glicksman in their 1996 study of Sn-40wt%Bi. After coarsening for very long periods of time, the microstructure underwent drastic morphological changes, with the initially branched structure breaking up into spherical particles (see Figure 2.2 [**41**]). Without secondary, or even primary arms, a different measure was clearly needed. They proposed using the specific interfacial area, S_v, which is the interfacial area per unit volume of the system under consideration and has units of inverse length. It has the advantage of being morphologically independent and so can be used to describe the coarsening process regardless of changes to the microstructure. The term S_v^{-1} is also useful, and commonly defined as the characteristic length of the system. Furthermore, S_v can be related to coarsening time by the formula

$$S_v^{-3}(t) - S_v^{-3}(0) = K_{LSW}t \tag{2.5}$$

and Marsh and Glicksman found that, over the entire observed coarsening range, despite the enormous changes in morphology, the evolution of the system was always described as $S_v^{-1} \sim t^{1/3}$ (see Figure 2.3 citeglicksman). All analysis of coarsening presented in this document will use S_v as a basis of measurement. While the coarsening exponent is the same, unlike the case of spherical particles, the condition of self-similarity seems not to be correlated with a $t^{1/3}$ evolution of S_v^{-1} in dendrites [**15**].

To study the curvature and evolution of dendrites without resorting to fixed geometries, three-dimensional data is needed. In 1966, Bower, Brody, and Flemings [**42**] used serial sectioning to study the shape of dendrite arms. Some work was done by Feijóo and Exner [**43**, **44**] using deep-etching combined with stereo-pictures to evaluate curvature

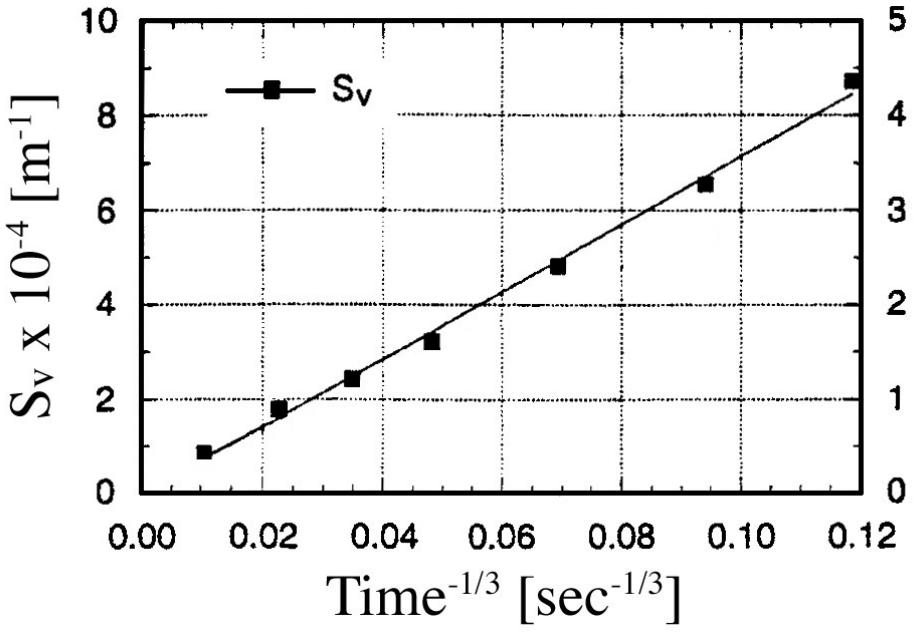

Figure 2.3. Change in specific surface area with time in Sn-40%Bi.

distributions of dendritic structures, but both methods had severe limitations. Only recently have advances in computing power allowed for more rigorous methods and models to be attempted.

The study of coarsening is further complicated by the effect of sedimentation. As dendrites coarsen, side branches or even entire dendrites will often pinch off from the rest of the solid region. Unsupported, gravity will cause these loose pieces to either sink or rise, depending on their relative density, through the liquid of the mushy zone and deposit on one side of the sample. This process is known as sedimentation, and results in non-uniform volume fraction of solid throughout the sample, thereby affecting all other measurements. The problem of sedimentation is more pronounced for alloys with a small volume fraction of solute, since the dendrite network is smaller and less interconnected. Long coarsening time also exacerbates the problem.

2.3. Coarsening in Bicontinuous Structures

Coarsening also affects so-called bicontinuous structures, where phases are interpenetrating and intricately connected. Bicontinuous structures form in both phase separating and phase ordering systems, including spin ordering in magnetic materials, spinodal decomposition in binary homopolymer mixtures, and microemulsions. Phase separation occurs when a homogeneous single-phase mixture is cooled below some critical temperature and it becomes thermodynamically favorable for two phases to form. This process may occur with conserved or nonconserved dynamics; that is, the amount of each phase after separation may be fixed or it may not be. Spinodal decomposition is a good example of conserved dynamics. The amount and composition of phase A and B are dictated by the phase diagram. Evolution can only occur by diffusion of mass from one region to another. Spin ordering is an example of nonconserved dynamics, as a region may switch from one domain (+) to the other (-) simply by the flipping of dipoles. Because of the interconnected nature of these structures, a decrease in the amount of interface requires continual pinching apart of both phases.

The growth law developed by LSW and given in Eqn. 2.3 can be modified for non-particulate systems by replacing $\bar{R}$, the average particle radius, with the characteristic length, l, defined above as S_v^{-1}, to be

$$l^m(t) - l^m(0) = K_{LSW}t \tag{2.6}$$

where m is the growth exponent, equal to 3 for conserved dynamics and 2 for nonconserved dynamics. Other effects such as fluid flow or elastic stress can also change the exponent.

Although it has been shown that dendritic coarsening does not proceed in a self-similar manner, recent work shows that bicontinuous structures do reach a regime of self-similar coarsening, as measured by the Interface Shape Distribution and topology [**45**].

CHAPTER 3

Spatial Correlations in Symmetric Bicontinuous Mixtures

3.1. Development of Calculation Method

Because curvature distributions and directionality are not enough to completely characterize a structure, a method was developed for quantifying the spatial correlation of complex structures such as dendrites and the bicontinuous structures discussed in the introduction. The radial distribution function has been used extensively to characterize particulate systems, but there are a number of challenges to applying it to systems without discrete particles.

The radial distribution function is defined for particle systems as

$$RDF = \frac{\text{No. Particles per area in a spherical shell}}{\text{Overall particle density}} \tag{3.1}$$

that is, if one starts at any given particle and goes out some radial distance, the RDF gives the probability of finding another particle at that distance, normalized by the overall density of particles in the system. An example of a typical RDF for a system of spherical particles is shown in Figure 3.1 [**46**]. In order to compare results from one sample to another, the radial distance is typically normalized by the average particle radius as in Figure 3.1. The RDF appears as a line with some combination of peaks and valleys, and at longer distances, generally shows a decaying oscillation about 1. One indicates that there is no correlation; in other words, the probability of finding anything is the same as

it would be in a system with a random distribution of particles. RDFs are often further specified to determine the correlations between particular sizes of particles, say, between large and small particles or between all particles with a given diameter range.

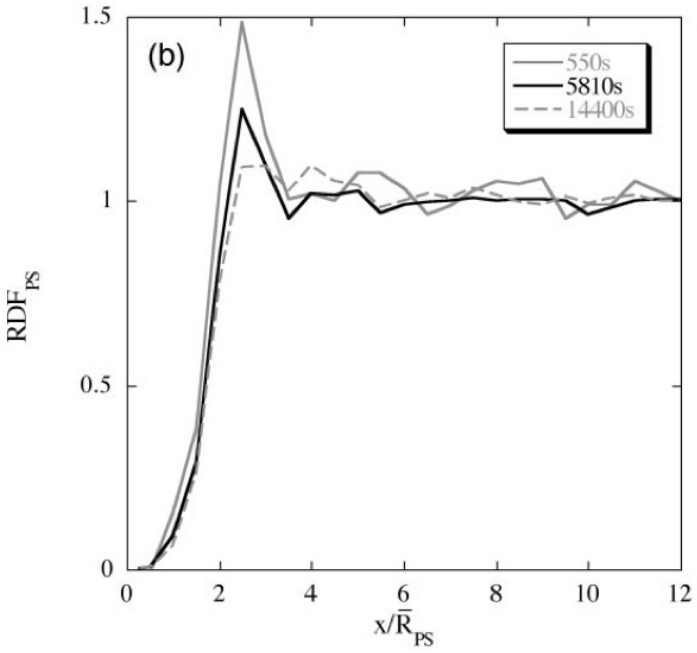

Figure 3.1. Typical RDF for system of spherical particles showing probability as a function of normalized distance. For this system, RDF changes somewhat with coarsening time.

When attempting to define a RDF for a non-particulate system, one must consider some particular aspect of the structure; in this case, the variation in curvature of the interface. As stated earlier, at least two values are needed to completely define the shape of a patch of curvature, such as the mean (H) and Gaussian curvature (K). This gives a spatial correlation function that is a function of five independent variables: H and K of two patches and r, where r is the distance between two interfacial patches. To reduce the dimensionality of the RDF I focused only on the mean curvature due to its significance in the coarsening process (see Equation 2.1).

Initially, I attempted to plot RDF the same way it was done for particle systems by choosing two regions of the ISD and calculating the correlation between them at all distances. An example of this is shown in Figure 3.2. It soon became apparent that this was not a good way to look at the data, as it required very large numbers of plots. For example, to see the correlations of each of the thirteen boxes and with themselves and all other boxes shown in Figure 3.2a would require 91 line plots and still does not capture all possible correlations. Also, there was no good way to determine size and location of these boxes, as there were no natural lines along which to distinguish the curvatures.

A more reasonable distinction is to plot correlations between all values of curvature at some discrete distance on a single plot. This requires a 2D contour plot similar to those used for IDSs and INDs. Using this method, the RDF is calculated for a series of concentric shells about all initial points, H_1 (see Figure 3.3). Now the RDF can be defined as the probability, referenced to the average over the sample volume, of finding an interfacial patch having a given mean curvature H_2 at distance r from a patch having a mean curvature H_1. This is given by the ratio of the interfacial area having a curvature of H_2 found inside a spherical shell to the volume-averaged interfacial area having the same curvature (see Figure 3.3), or

$$G(H_1, H_2, r) = \frac{A(H_2, r)}{A_v(H_2) 4\pi r^2 dr} \tag{3.2}$$

where $A(H_2, r)$ is the interfacial area having curvature H_2 within a spherical shell of thickness dr at a radial distance, r, measured from a point having curvature H_1, and $A_v(H_2)$ is the volume-averaged total interfacial area per unit volume having curvature

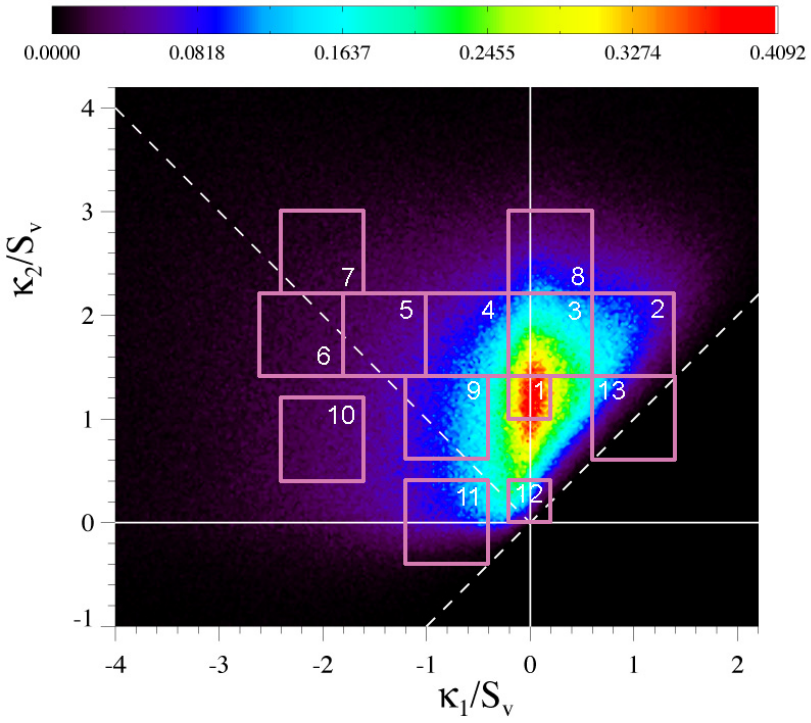

(a)

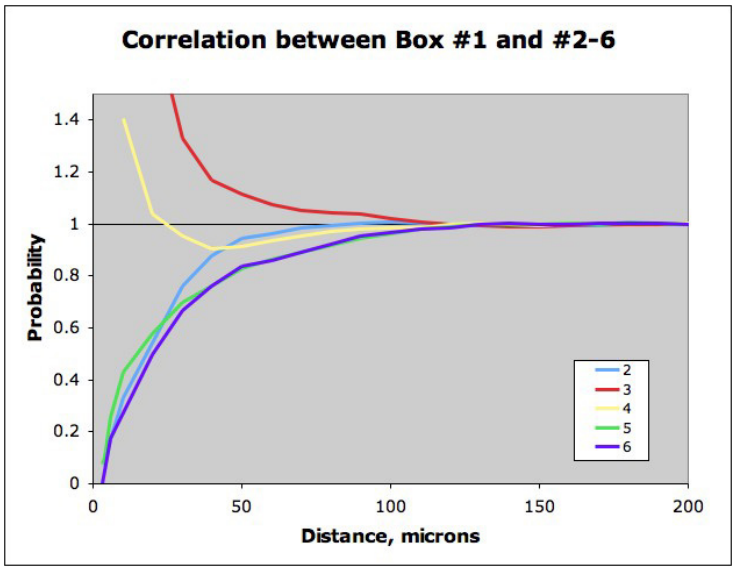

(b)

Figure 3.2. Initial method of calculating RDF for complex systems. Example shown is Pb-Sn dendrites, 43% solid, 3 minute coarsening time. See Chapter 7 for more data from this system. (a) The ISD was broken into regions and the correlation between any two boxes could be calculated. (b) Some of the correlations measured between boxes for the system in (a).

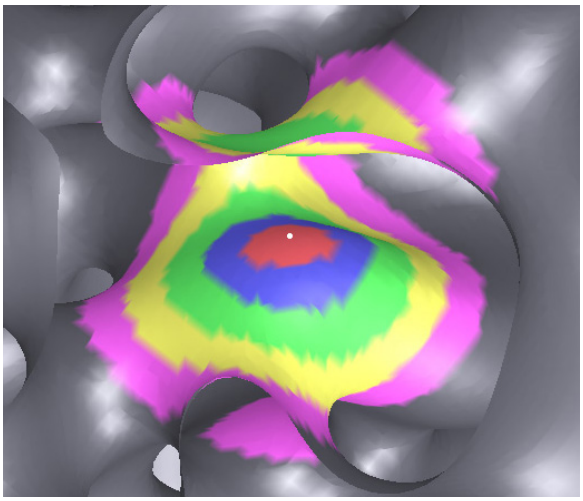

Figure 3.3. Red, blue, green, yellow and purple display the interfaces that are within the first five shells, each having a width of 1/3 S_v^{-1}, centered around an initial patch of interface, shown in white. It is clear from this figure that a patch is typically surrounded by similar values of H at small distances and interfaces with many different values of H at larger distances.

H_2, calculated for the entire volume. As before, G will approach 1 in the limit where $r \rightarrow \infty$.

An example of the RDF for $r = 1/3 S_v^{-1}$ one of some generic structure, where r is much less then a typical radius of interfacial curvature, is shown in Figure 3.4. By looking at Figure 3.3, it is clear that the curvature in the red region is very similar to the curvature of the initial point. Therefore, since the interfacial patch size is very small compared to the scale of the structure, all positive correlations at this distance should be between curvatures of the same or similar values. Figure 3.4 shows this to be the case, with all correlations running along the $H_1 = H_2$ line. This will be true for any real (non-fractal) structure since surface energy acts to smooth the curvature. In general, the plots must be symmetric across the $H_1 = H_2$ line (shown as a dotted line) since $G(H_1, H_2, r) = G(H_2, H_1, r)$ by definition.

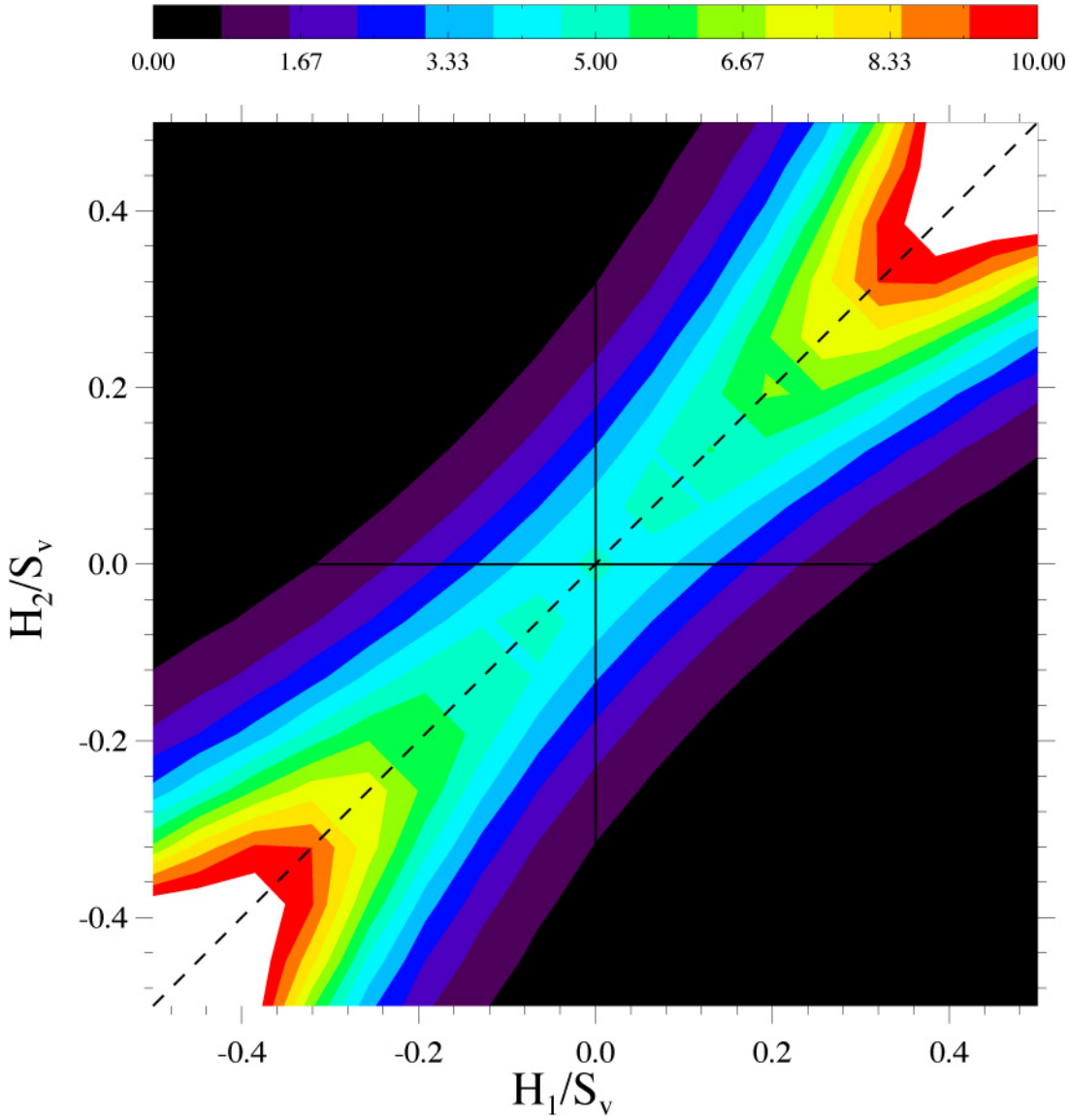

Figure 3.4. RDF for $r = 1/3S_v^{-1}$ for some generic structure. At this distance, correlations between like curvatures are extremely high. Notice that the axes are scaled by the characteristic length of the system. White indicates values greater than ten.

As the bell shape of the curvature distribution indicates (shown below in Figure 3.6), there is very little area with high absolute curvature values. The relative scarcity of

this curvature, which is not randomly distributed through the structure but concentrated into a few features, causes the probability to scale inversely with the relative amount of curvature. That is, the higher the magnitude of curvature is, the more scarce it is and the more relatively concentrated it is, producing a higher correlation value. Larger absolute values of mean curvature also correspond to regions with very small radii of curvature (i.e., very small features) where the curvature changes quickly over a smaller spatial distance, causing the region of increased probability to widen near the edges of the plot.

3.2. Structures for Analysis

The method of analyzing spatial correlations using the Radial Distribution Function was first applied to two structures composed of bicontinuous phases of equal volume, shown in Figure 3.5. They were obtained by numerically evolving the Cahn-Hilliard equation, which governs conserved dynamics, and the Allen-Cahn (time-dependent Ginzburg-Landau) equation, which governs nonconserved dynamics, from an initial condition having random noise around a mean value chosen such that the volume fraction of each phase is 50%. Complete details about these structures can be found elsewhere [**45**, **47**], including the structure function, which is the parameter generally used to characterize this type of complex structure. These structures provided a good testing ground for the new method because the 3D models were not affected by experimental error.

While the driving force for the evolution of interfaces is related to the interfacial mean curvature in both cases, the interfacial motion occurs by different mechanisms. In the conserved dynamics, mass is conserved and coarsening takes place by the diffusion of species from one region to another; thus the interfacial motion depends not only on the

local curvature, but also on the mean curvatures of surrounding interfaces. On the other hand, for the nonconserved dynamics, the velocity at a point on the interface depends only on the mean curvature at that point.

The probability of finding a patch of interface with a given value of the mean curvature for each structure has a peak at $H = 0$ and is symmetrically distributed about zero, see Figure 3.6. When the distributions are plotted in terms of a scaled mean curvature H/S_v, where S_v is the surface area per unit volume, unique time-independent distributions result. The distribution is narrower for the conserved dynamics case as compared with the nonconserved dynamics case. Despite this difference, the two structures were found to be topologically similar, with nearly identical values of scaled genus [**45**].

The RDFs were calculated for conserved and nonconserved structures of size $(22S_v^{-1})^3$ and $(16S_v^{-1})^3$, respectively. For each structure, 120,000 initial H_1 values were sampled, each providing many thousands of patches for H_2. Since all structures were initially created using periodic boundary conditions, I was able to calculate the RDF across the boundaries, effectively creating a much larger volume from which to sample data. Utilizing the periodic boundary conditions in this way dramatically decreased the noise near the edges of the plots and allowed correlations to be calculated out to much longer distances. To obtain sufficient statistics while ensuring a good resolution in r, the shell thickness resolution Δr was set to $1/3(S_v^{-1})$. The correlation functions were also plotted for values of scaled curvature $-H_{max} < H < H_{max}$ such that some percentage of the total interfacial area is included in the data displayed. Unless otherwise noted, all plots in this section are scaled to display curvatures of 90% of the total surface area. This does not result in loss of essential data since high curvature areas (with large $|H|$) are evolving quickly, thus their

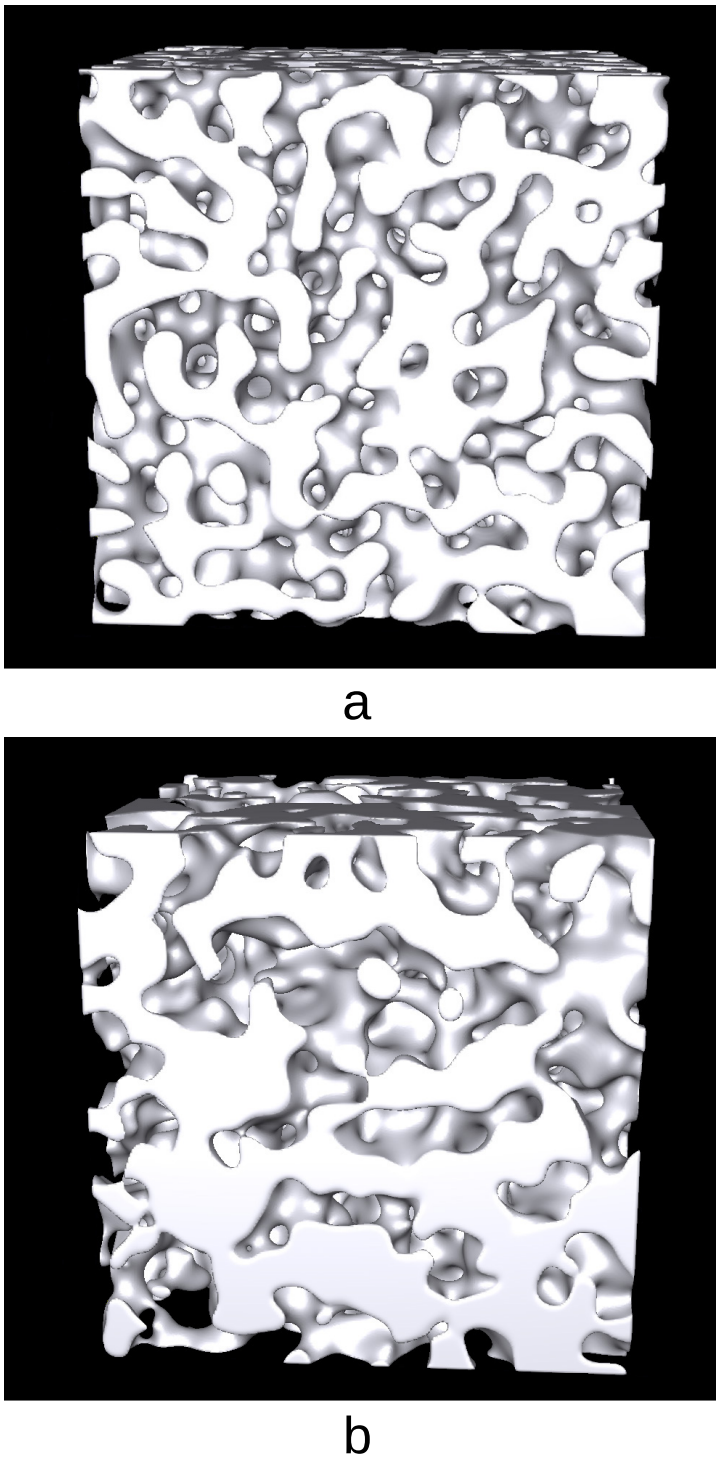

Figure 3.5. Two structures used for analysis, (a) conserved order parameter and (b) nonconserved order parameter.

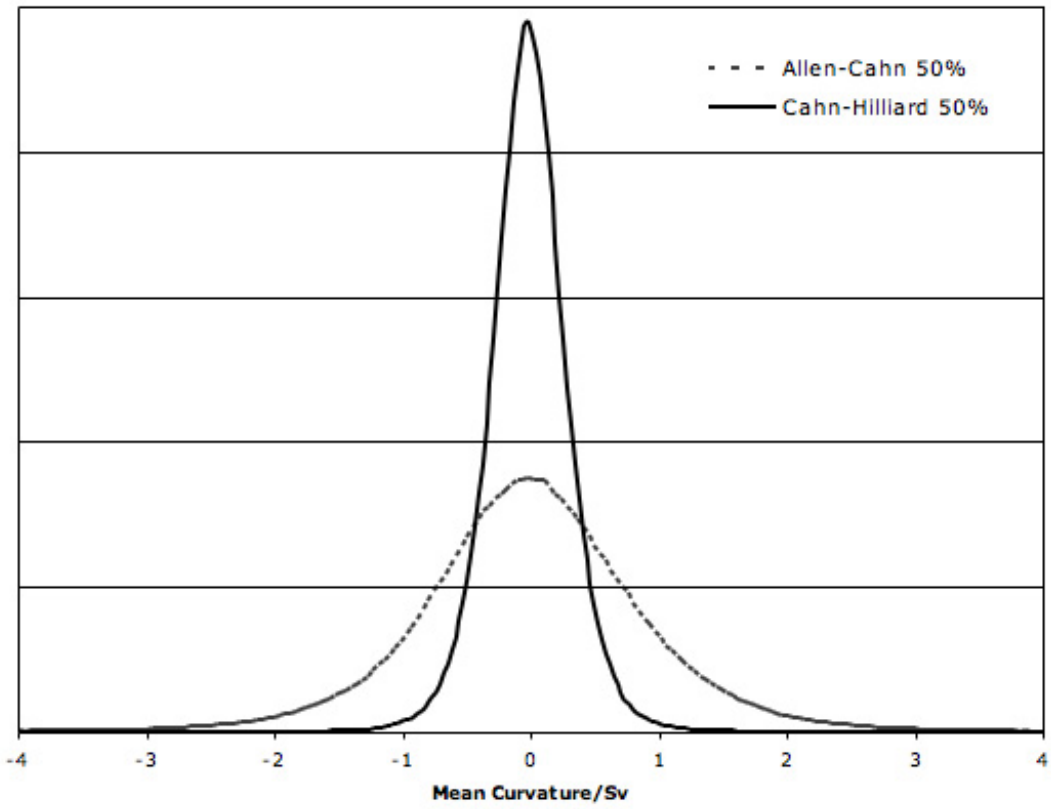

Figure 3.6. Mean curvature distributions for symmetric, 50% solid structures produced by evolving the Cahn-Hilliard equation (conserved dynamics) and the Allen-Cahn equation (nonconserved dynamics).

existence is strongly transient in nature. These measures, along with scaling the axes of the plot by the characteristic length of the system (S_v^{-1}) allows one to compare results for the two different structures, despite the differences in width of the scaled curvature distributions.

Since the interfacial morphologies resulting from both the conserved and the nonconserved dynamics attain statistically unique time-independent states when scaled by their characteristic length [**45**], the scaled spatial correlation was expected to have specific time-independent forms as well. The RDF for the conserved system was thus compared

with another structure that had been evolved approximately twice as long. When scaled by S_v^{-1}, the spatial correlation functions were found to be statistically the same, confirming this time-independence. We thus plot the correlation functions as a function of the dimensionless curvatures $\tilde{H}_1 = H_1 S_v^{-1}$, $\tilde{H}_2 = H_2 S_v^{-1}$ and distance $\tilde{r} = r S_v^{-1}$. In both the conserved and nonconserved structures a radius of curvature of the interfaces has a magnitude that is on the order of S_v^{-1} [**45**].

3.3. Analysis of Structure with Conserved Dynamics

The RDF of the structure produced using conserved dynamics, with its nonlocal evolution, is shown in Figure 3.7. As mentioned above, the plots must be symmetric across the $\tilde{H}_1 = \tilde{H}_2$ line. Because both structures discussed in this section have equal volume fractions of the two phases, the plots will also be symmetric across the line $\tilde{H}_1 = -\tilde{H}_2$. The RDF shows a fairly complex pattern of spatial correlations with several distinct regions of positive correlation. At very short distances (see Figure 3.7a) all enhanced probability is concentrated along the $\tilde{H}_1 = \tilde{H}_2$ line and is higher for larger values of $|\tilde{H}_1|$ and $|\tilde{H}_2|$. From $\tilde{r} = 1$ to 4/3, Figure 3.8b and 3.8c, these strongly localized correlations begin to decay, and patches of $\tilde{H} = 0$ reach a random distribution at $\tilde{r} = 1$.

As the positive correlation between similar curvatures decreases with increasing distance, a separate nonzero probability begins to appear for patches of interface that have different signs of the curvature. This probability grows in intensity until it dominates at $\tilde{r} = 5/3$ (Figure 3.7d) and regions where both patches have either very large or very small curvature become slightly anticorrelated at $\tilde{r} = 2$, Figure 3.7e. These correlations and

anticorrelations slowly disappear near $\tilde{r} = 10/3$ (see Figure 3.8). The like-curvature correlation reappears weakly at about four times the magnitude of the characteristic radius of curvature of the interfaces ($\tilde{r} = 4$), and the opposite-curvature correlation returns yet more weakly around $\tilde{r} = 5$ (Figure 3.8). The distance over which the correlation function oscillates as it decays is a characteristic length scale of these structures that can only be identified through analysis such as this.

As mentioned, strong correlations were found between patches of interface with like curvatures for $\tilde{r} \leq 5/3$ (Figure 3.7a-d). Since surface energy acts to smooth a spatial variation in the curvature and the interfacial patch size is very small compared to the scale of the structure, most patches are surrounded by other patches of similar curvature, producing this type of correlation. For this reason, the correlation functions of the conserved and nonconserved structures are similar at very short distances, as will be seen. However, examination of the conserved structure revealed that these regions are larger than the length scale over which surface energy would be expected to act, and that they are instead the result of the interconnected structure and pinching events. The high curvature tubes formed during pinching act to constrain the structure so that the interfaces on both ends of the tube have curvatures of the same sign. In the conserved case these pinching events occur quite quickly, but the remnants of the pinched tubes persist and contribute to the enhanced correlations between regions of interface with large absolute values of curvature. The enhanced rate of pinching in the conserved case as compared to the nonconserved case can be seen in shrinking spherical particles. When such particles shrink by conserved dynamics or diffusion, the shrinkage rate goes as $1/R^2$ whereas for nonconserved dynamics the shrinkage rate goes as $1/R$. Thus as $R \rightarrow zero$, conserved

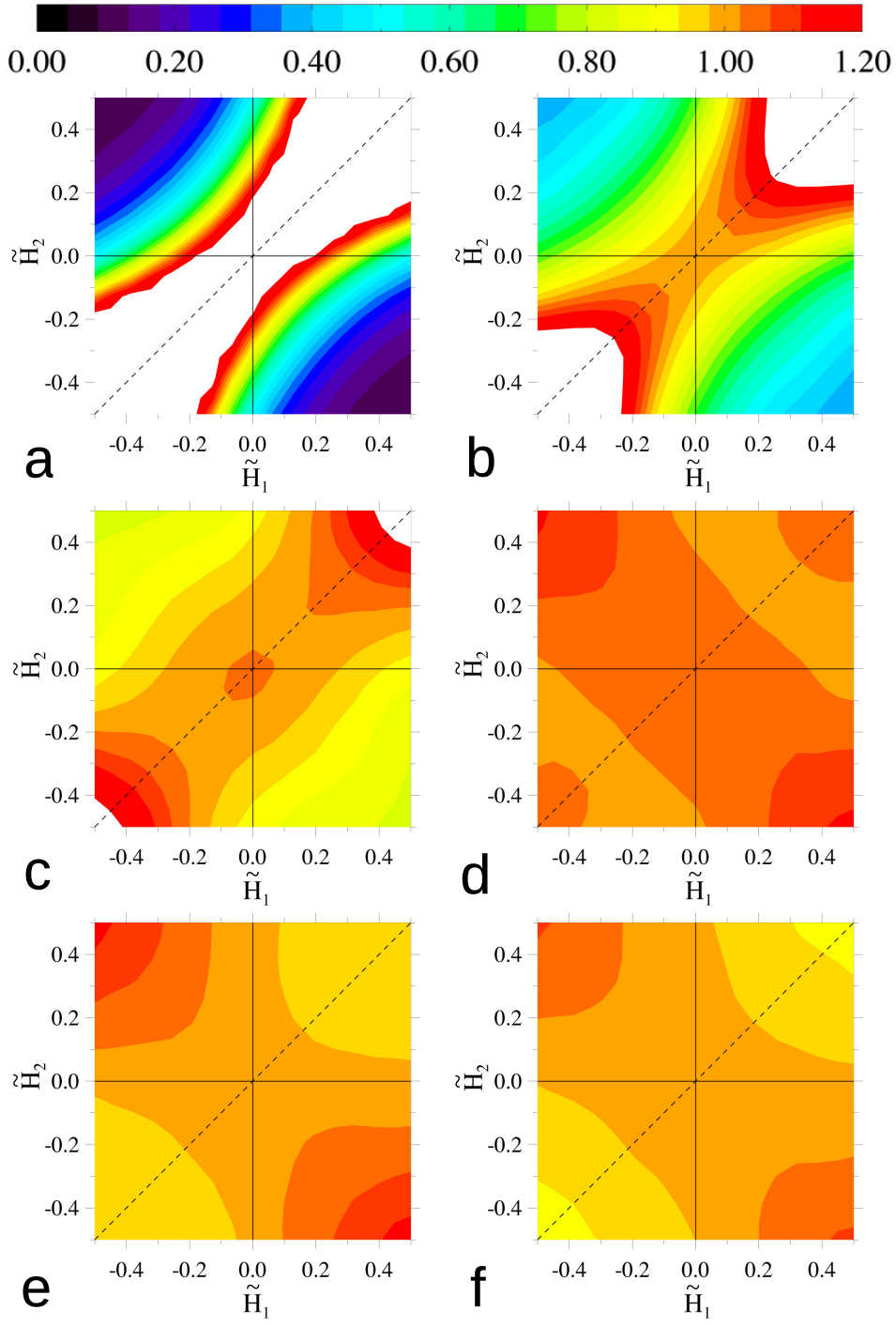

Figure 3.7. Spatial correlations in the conserved structure for a variety of distances. Plots were constructed using a shell of thickness 1/3 at $\tilde{r}$ = (a) 2/3, (b) 1, (c) 4/3, (d) 5/3, (e) 2, and (f) 7/3. The data shown represents greater than 90% of total interfacial area. White indicates a probability of greater than 1.2.

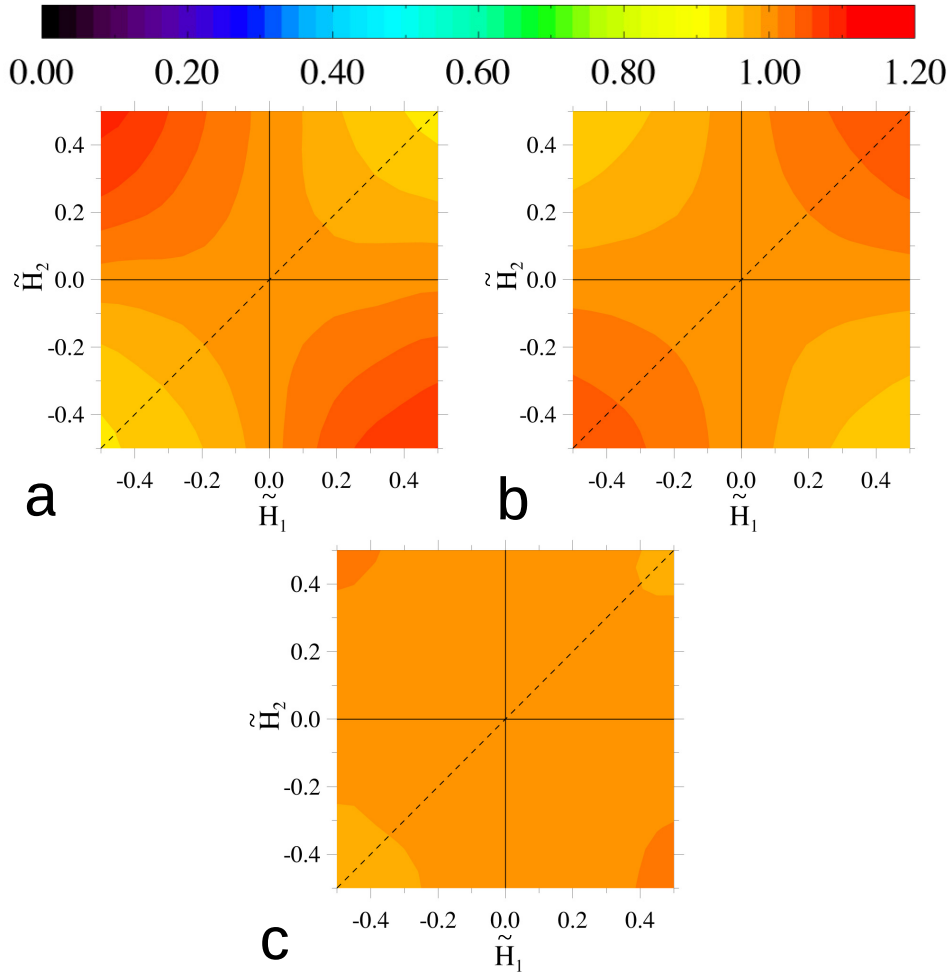

Figure 3.8. Spatial correlations in the conserved structure at very long distances of $\tilde{r}$ = (a) 3, (b) 4, and (c) 5, showing the fluctuation between correlation of similar curvature and opposite curvature. Note that a higher resolution is required in the color bar for these smaller correlations to be visible.

dynamics yield much faster transformation rates than nonconserved dynamics. This is also why the probability of finding two interface patches with opposite signs of H at this distance is very low since such an arrangement would introduce a rapid mass flow from one region of curvature to the other or a high interfacial velocity and thus disappear from the system.

Because the evolution of this structure is driven by diffusion, it is best to have regions of positive and negative curvature near each other as they act as sources and sinks for diffusing mass. The distance between these positive and negative mean curvature regions must be long enough that the difference in chemical potential does not create an unduly high diffusion gradient and the subsequent elimination of one region, as it does at shorter length scales. Thus the only pinching remnants which persist in this structure are those that occur at a distance favorable for diffusion, $5/3 \leq \tilde{r} \leq 10/3$, appearing in the plots as an increased correlation between curvatures of opposite signs. The necessity for sources and sinks of mass in the conserved order parameter model creates a somewhat regular structure, with correlations that extend to at least $\tilde{r} = 5$.

These regions of positively and negatively curved interface are separated by bands of near-zero mean curvature. Note that in this case, zero mean curvature does not indicate a flat interface but rather an interface with equal and opposite values of the principal curvatures. The uniform separation of the positive and negative curvature regions means that the spacing between regions of near-zero mean curvature is also quite regular, and so causes the slight increase in probability near zero curvature at $\tilde{r} = 4/3$ (Figure 3.7c). This small probability peak can also be found at $\tilde{r} = 5/3$, but its small value at this distance means that is is not visible in Figure 3.7d as plotted.

3.4. Analysis of Structure with Nonconserved Dynamics

The RDF of the structure produced with nonconserved dynamics is given in Figure 3.9 and displays a comparatively simple correlation pattern. At very short distances, $\tilde{r} = 2/3$ (Figure 3.9a), it follows the probability enhancement along $\tilde{H}_1 = \tilde{H}_2$ described above,

clearly showing that the structure does not have a random spatial distribution at short distances as has been sometimes assumed [**48**]. The strongly convoluted nature of the interfaces shown in Figure 3.5b is illustrated by the correlations at $\tilde{r} = 4/3$, Figure 3.9c. At this distance, interfaces with approximately zero mean curvature, $\tilde{H}_1 = 0$, are surrounded by a nearly random distribution of interfaces with a wider range of curvatures, $|\tilde{H}_2| < 1.4$, than for conserved dynamics, see Figure 3.9c. In the conserved case the interfacial energy induces a smoothing that occurs by long-range diffusion, whereas in the nonconserved case the motion of the interface is much more local and thus for the same value of interfacial energy it is possible to have more irregular interfaces. As a result, there is a wider distribution about $\tilde{H}_1 = \tilde{H}_2$ for the nonconserved case as compared to the conserved case at short distances.

As $\tilde{r}$ increases, the nonconserved structure maintains its preference for positive correlations between like curvatures, although the magnitude of these increased probability regions decreases and their width increases. Curvatures near zero reach a random distribution by $\tilde{r} = 5/3$, with all values reaching a random distribution by $\tilde{r} = 8/3$, just less than three times the characteristic length. Correlation plots for this distance and greater show all that curvatures are randomly distributed in space. Unlike the conserved dynamics case, no positive correlation is ever observed between regions of opposite curvatures since there is no need for diffusion of mass from positive to negative curvatures for the structure to coarsen.

The evolution of the curvature in the nonconserved system is not strictly local since it depends on the second derivatives of the interfacial velocity (or curvature) [**49**]. However, this should lead to a very short ranged correlation on the order of the radii of principal

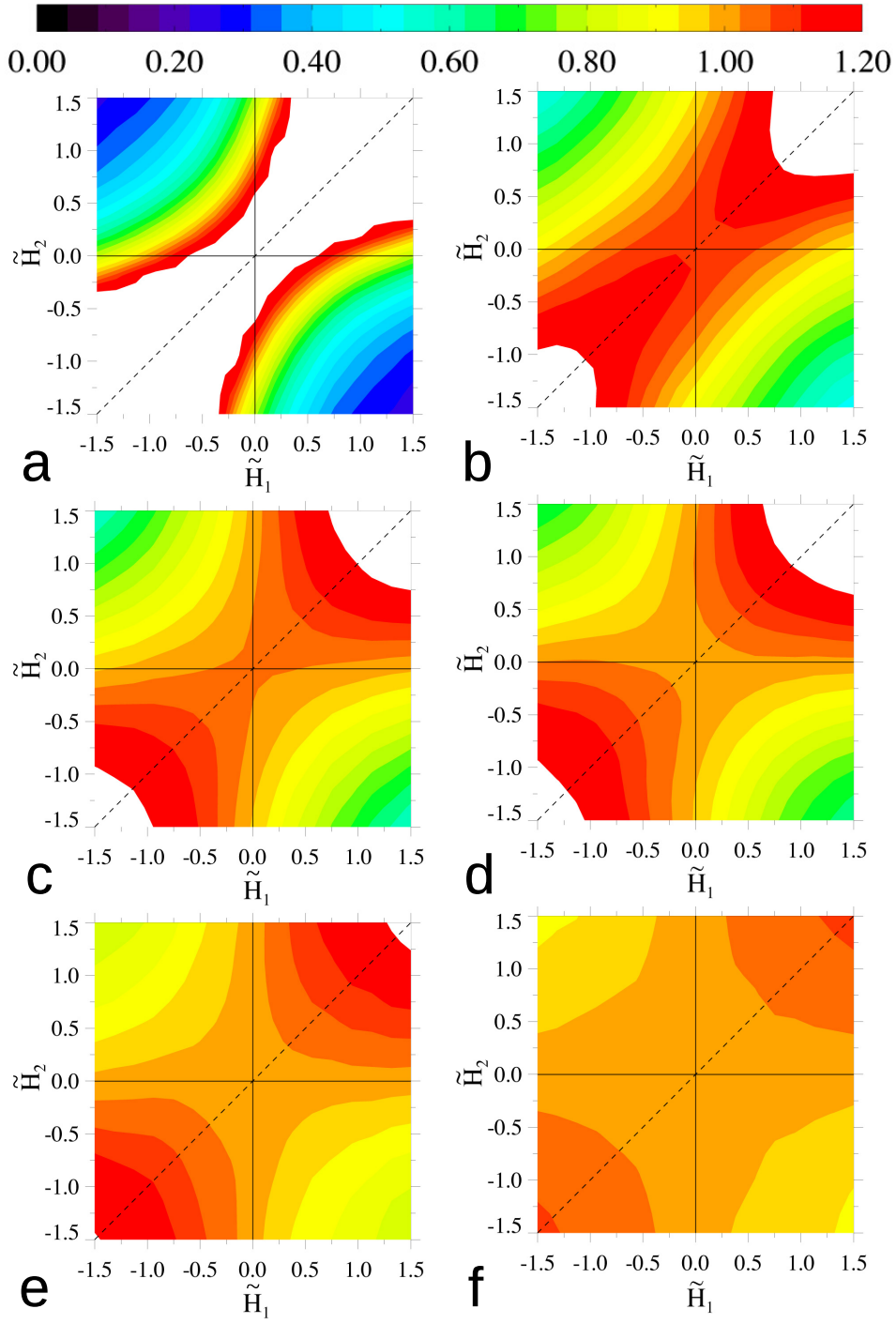

Figure 3.9. Spatial correlation in the nonconserved structure calculated for shells of thickness of 1/3 and $\tilde{r}$ = a) 2/3, b) 1, c)4/3, d)5/3, e) 2, f) 7/3. The data shown represents greater than 90% of total interfacial area. White indicates a probability of greater than 1.2.

curvatures, $r = S_v^{-1}$ [**45**]. Instead, curvatures of the same sign are correlated out to a distance of $\tilde{r} = 7/3$, see Figure 3.9. This long-ranged correlation gives rise to regions with a diameter on the order of 4 that have curvatures of the same sign. As was the case in the structure with the conserved order parameter, these large regions are related to the tubes that are present in this interconnected structure. Because interface motion does not require long range diffusion, pinching occurs more slowly in the nonconserved case, and thus it is far easier to identify the tubes and their remnants (a cap that is locally spherical). As in the conserved case, the high-curvature tubes act to constrain the structure, so that the interfaces on both ends of the tube have curvature of the same sign. This region of positive or negative mean curvature will persist until it meets a tube, or a remnant thereof, of opposite sign. Thus, this length scale of regions of positive and negative curvature is roughly equal to the distance between active pinching events, or high-curvature tubes, and the morphology of the bicontinuous structure itself induces the correlations in the curvature that we observe.

3.5. Summary

I have developed a new method of broad applicability to quantify the morphology of topologically complex interfaces by calculating the spatial correlation of interfacial curvature. I have used this method to determine the structure of bicontinuous, two-phase mixtures produced using conserved and nonconserved dynamics. I find that the long-range diffusive interactions resulting from conserved dynamics yield specific correlations and anticorrelations over an extended length scale. The correlations indicate regularly spaced regions of positive and negative curvature which is a new characteristic length

scale for this structure. Despite the local nature of the interfacial evolution process in the nonconserved case, spatial correlations on a relatively long scale were observed. These correlations are attributed to the persistence of high curvature tunnels in the structure. The spacing between these tunnels constitutes a new characteristic length scale for these structures. The time independence of both the scaled spatial correlation functions and the interface shape distributions indicate that the interfacial morphologies in these cases assume a unique time independent form.

CHAPTER 4

Spatial Correlations in Nonsymmetric Bicontinuous Mixtures

4.1. Structures for Analysis

The method of analysis described in Section 3.1 was applied to two structures composed of bicontinuous phases, shown in Figure 4.1. One is a symmetric mixture with a volume fraction of 50% (this is the same as the conserved structure discussed in Chapter 3). The other is an asymmetric mixture produced by an off-critical quench with a volume fraction of 36%. The structures were obtained by numerically evolving the Cahn-Hilliard equation, which has conserved dynamics. More details about these structures can be found elsewhere [**45**, **50**]. The evolution of the structures is nonlocal, in that mass is conserved and coarsening takes place by the diffusion of mass from one region to another.

The Mean Curvature Distribution (MCD) for each structure is shown in Figure 4.2. When the distributions are plotted in terms of a scaled mean curvature H/S_v, where S_v is the surface area per unit volume, unique time-independent distributions result. Conserved dynamics produces a fairly regular interface with a narrow distribution of curvature around the average mean curvature of the structure. When the mixture is symmetric, the curvature distribution is symmetric about zero. For comparison, the MCD for a symmetric structure produced using nonconserved dynamics (evolution of the Allen-Cahn or time-dependent Ginzburg-Landau equation) is also shown. Analysis of the correlations in this nonconserved-dynamics structure can be found in Chapter 3 and [**51**].

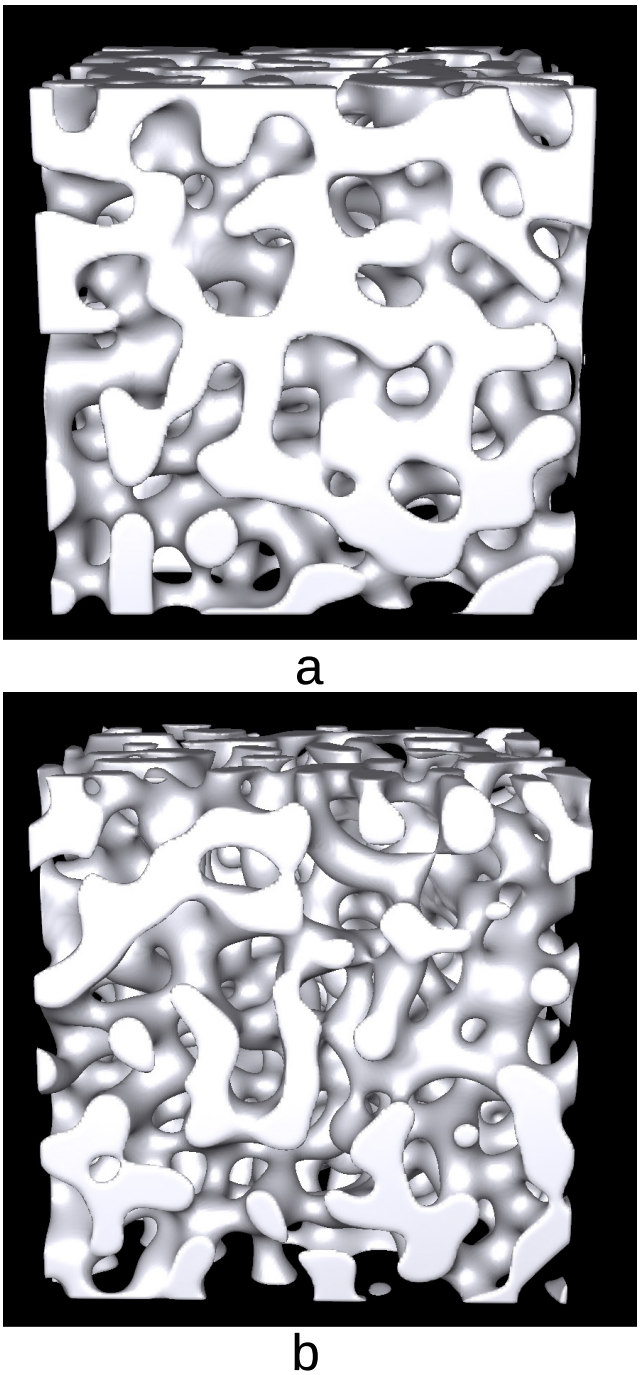

Figure 4.1. Two structures used for analysis, a) symmetric mixture 50% solid and b) asymmetric mixture 36% solid.

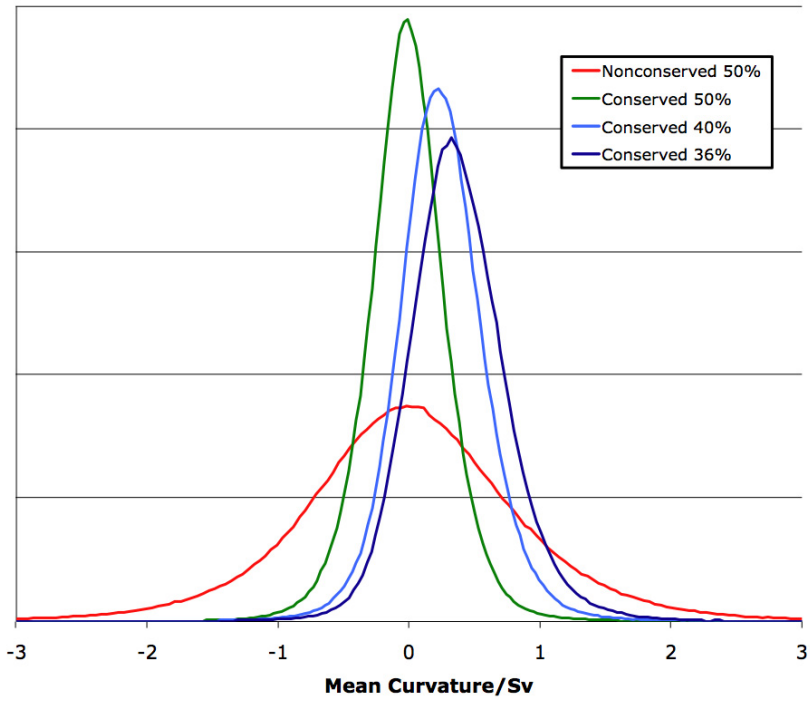

Figure 4.2. Mean curvature distribution of symmetric and asymmetric mixtures with conserved and nonconserved dynamics.

An asymmetric mixture, however, has a mean curvature distribution that is centered about some non-zero value, and is relatively wider than the distribution of the symmetric structure. As the figure shows, the shift away from zero and the increase in distribution width are proportional to the degree of asymmetry. A mixture containing 40% solid has a MCD that is midway between the symmetric mixture and the asymmetric 36% solid mixture. The correlations in the 40% solid mixture were also found to be intermediate, with no unique features, and so will not be discussed further. The MCD for asymmetric mixtures is also not perfectly symmetric about the maximum value. For the 36% solid mixture, the right side of the MCD has a slightly greater slope than the left side as well as a longer tail.

The RDFs were calculated for symmetric and asymmetric mixtures of size $(22S_v^{-1})^3$ and $(20S_v^{-1})^3$ respectively. The same symmetric mixture was discussed in Chapter 3. For each structure, 80,000 to 120,000 initial H_1 values were sampled, each providing many thousands of patches for H_2. Since all structures were initially created using periodic boundary conditions, it was possible to calculate the RDF across the boundaries, effectively creating a much larger volume from which to sample data. To obtain sufficient statistics to ensure a good resolution in r, the shell thickness resolution Δr was set to $1/3(S_v^{-1})$. To further reduce statistical noise, the plots shown are obtained by averaging together the RDFs obtained from two separate structures evolved under the same physical assumptions but with initial conditions created by different seeds for the random noise generation. This serves to reduce the noise, particularly near the edges of the plot, although there are no major differences between the two mixtures being averaged.

Since the interfacial morphologies resulting from the conserved dynamics attain statistically unique time-independent states when scaled by their characteristic length [**45**], the scaled spatial correlation was expected to have specific time-independent forms as well. To confirm this, the RDF for the symmetric system was compared with another simulated structure which had been evolved for approximately twice as long. When scaled by S_v, the spatial correlation functions were found to be statistically the same, confirming this time-independence. Thus we plot the correlation functions as function of the scaled curvatures $\tilde{H}_1 = H_1 S_v^{-1}$, $\tilde{H}_2 = H_2 S_v^{-1}$ and distance $\tilde{r} = r S_v^{-1}$. In both the symmetric and asymmetric mixtures the average radius of curvature of the interfaces has a magnitude that is on the order of S_v^{-1}, which can be defined as the characteristic length of the system.

In order to directly compare results for the two structures, despite the differences in scaled MCDs, the correlation functions were plotted using some width $\pm\tilde{H}_{max}$ around the maximum value of the MCD. $\tilde{H}_{max}$ was chosen such that 98% of the total interfacial area is included in the data displayed, as opposed to the 90% used to produce the results shown in the previous chapter. This does not result in loss of essential data since high curvature areas (with large $|\tilde{H}|$) are evolving quickly and thus their existence is extremely transient in nature. For the symmetric mixture, $\tilde{H}_{max} = 0.83$ and the maximum of the MCD at $\tilde{H} = 0.00$. For the asymmetric mixture, $\tilde{H}_{max} = 1.00$ with the maximum of the MCD at $\tilde{H} = 0.33$.

4.2. Analysis of Symmetric Mixture

Figure 4.3 shows the correlations in the symmetric structure with conserved dynamics. As distance increases, the probability falls from that shown previously in Figure 3.4. At $\tilde{r} = 4/3$ (Figure 4.3b) a separate nonzero probability begins to appear for patches of interface with curvature of opposite sign. At the same distance, a small increase in correlation between patches of $\tilde{H} = 0$ is also seen. At $\tilde{r} = 5/3$ (Figure 4.3c) the initial correlations between like curvatures have decayed to small peak centered at $\tilde{H} = |0.5|$. These two instances are the only observed peaks with discrete boundaries which do not increase or decrease continuously with increasing magnitude of curvature. At $\tilde{r} = 2$ (Figure 4.3d) like curvatures have become anticorrelated, while the correlations between curvatures of opposite signs continue to grow. From $\tilde{r} = 7/3$ to $10/3$ the magnitude of both the correlations and the anticorrelations decreases, and then positive correlations between curvatures of like sign return at $\tilde{r} = 4$. This oscillation of the correlations and

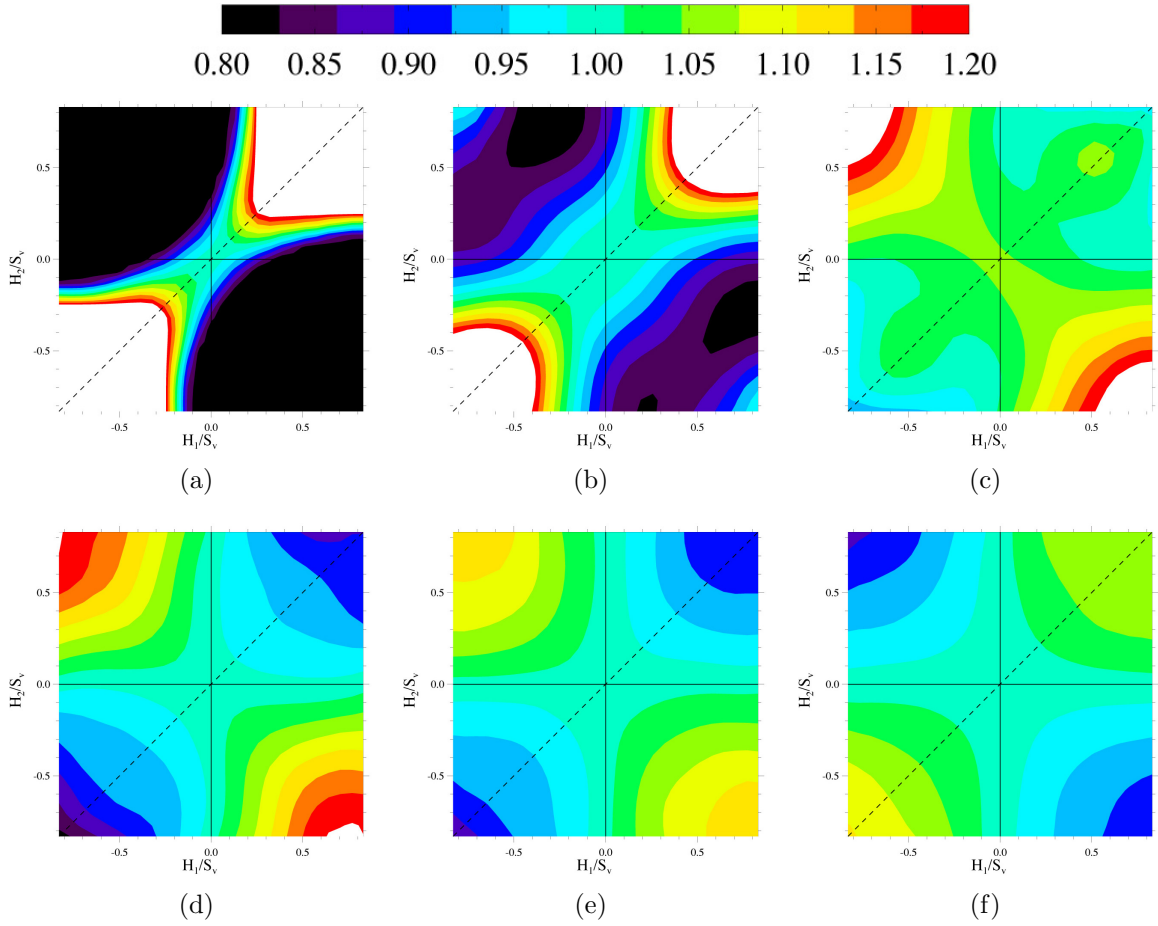

Figure 4.3. Spatial correlations in the symmetric mixture for a variety of distances. Plots were constructed using a shell of thickness 1/3 at $\tilde{r}$ = a) 1, b) 4/3, c) 5/3, d) 2, e) 3, and f) 4. White indicates a probability of greater than 1.2.

anticorrelations between high-magnitude curvatures of the same sign and opposite sign continues with decreasing intensity out to $\tilde{r} = 7$ before all correlations disappear and all curvatures are randomly distributed. Additionally, note that the curvature of the structure is such that at $\tilde{r} = 5/3$ (Figure 4.3d) more interfacial area falls within the shell than at other distances, causing the probability of all values of curvature to be above that expected for a random distribution.

With the exception of the two discrete peaks in the symmetric mixture mentioned above, the RDF plots can be thought of as showing correlations between different primary regions of curvature, with the overlapping effects of each region making up the contours of the plots. The symmetric mixture has only two primary regions: correlations between regions interface with similar curvature or between regions with opposite curvature. These primary regions can be identified by the increase in magnitude of correlation or anticorrelation with increasing magnitude of curvature and with increasing similarity between patches of curvature being compared. For example, at any given distance, the magnitude of the correlation between two patches of $\tilde{H} = 1$ will be higher than between two patches of $\tilde{H} = 0.7$.

To more easily follow the changes in correlations for each of these primary regions, the correlations for each region as a function of distance are plotted in Figure 4.4. In the symmetric mixture, both primary correlations show a decaying oscillation about 1, reaching a random distribution by seven times the characteristic length of the system. The two primary correlations are clearly related, as they are perfectly out of phase with each other. As we previously reported [**51**], this oscillatory behavior results from large regions of interface within the structure which are composed primarily of either positive or negative curvature. Regions of curvature with a high magnitude are created when one phase undergoes a pinching event. Because of the interconnected nature of the mixture, any increase in length scale requires the pinching apart of one of the phases. This creates a high-curvature tunnel which, after pinching, leaves behind two hemispherical caps of high curvature.

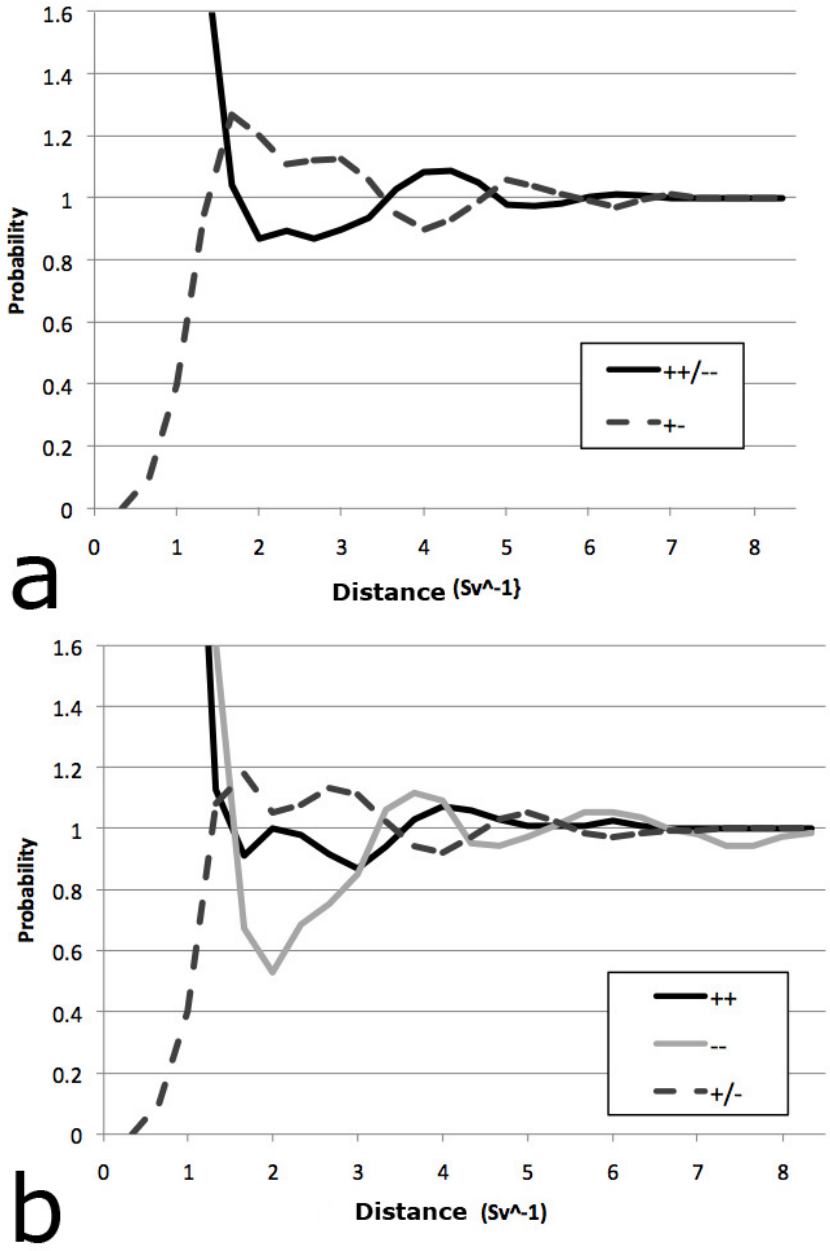

Figure 4.4. RDFs for the primary correlation regions of the (a) symmetric mixture and (b) asymmetric mixture. Lines indicate correlations between similar positive curvature (++), regions of similar negative curvature (–) and regions of opposite curvature (+/-) In the symmetric mixture, (++) and (–) are the same.

Because the evolution of this structure is driven by diffusion, it is necessary to have regions of positive and negative curvature near each other as they act as sources and sinks for diffusing mass. While the difference in chemical potential between two patches of interface with different positive (or negative) curvatures could also drive diffusion, the necessary difference in magnitude between curvatures of like sign would require curvatures of a very high magnitude which disappear quickly and thus are not commonly present in the structure. The distance between these positive and negative mean curvature regions must be long enough that the difference in chemical potential does not create an unduly high diffusion gradient and the subsequent elimination of one region, as it does at shorter length scales. Thus the morphology of this structure, and the corresponding correlations, are a result of diffusion acting on pinching remnants, so that the only remnants which persist are those that occur at a distance favorable for diffusion, $5/3 \leq \tilde{r} \leq 10/3$, appearing in the plots as an increased correlation between curvatures of opposite signs. The size and spacing of these positive or negative curvature regions is so regular that correlations extending out to $\tilde{r} = 7$ are observed.

These large regions of positively and negatively curved interface are separated by bands of near-zero mean curvature. Note that in this case, zero mean curvature is not a flat interface but rather an interface with equal and opposite values of the principal curvatures. The uniform separation of the positive and negative curvature regions means that the spacing between regions of near-zero mean curvature is also quite regular, and so causes the slight increase in probability near zero curvature at $\tilde{r} = 4/3$ (Figure 4.3b).

The discrete peaks that remain at $\tilde{r} = 5/3$ also provide insight into the morphology of the system. They represent the curvature regions which exhibit self-correlation over the

Figure 4.5. Small segment of the interface in the symmetric structure, with curvature of $\tilde{H} = -0.5 \pm 0.1$ highlighted in red. Visible are two rings which mark the top and bottom of a recent pinching event.

longest distance, indicating the size of the largest continuous region of any one curvature. These regions consist of curvature with $|\tilde{H}| = 0.5$. Note these are regions of curvature that have an average radius of curvature equal to half the characteristic length. From observing the curvature distribution directly on the structure, it was observed that $|\tilde{H}| = 0.5$ corresponds to the smallest magnitude of curvature which is predominately rings around pinching remnants, as shown in Figure 4.5. Curvatures closer to zero are generally distributed as long bands through the structure, as described above, and so have a shorter self-correlation. Curvatures of greater magnitude also correspond to pinching remnants, but are relatively smaller features and so have a shorter self-correlation. Visual analysis of the 3D structure confirms that $|\tilde{H}| = 0.5$ forms rings which are have a maximum diameter of about $\tilde{d} = 4/3$. Note that these are rings of iso-curvature on the interface and do not indicate tubes of this size in the structure.

4.3. Analysis of Asymmetric Mixtures

The asymmetry of the second mixture introduces another layer of complexity to the spatial correlations, as seen in Figure 4.6. While initially similar to the correlations seen in the symmetric mixture, by $\tilde{r} = 1$ the asymmetry becomes apparent, as the correlations between regions of negative curvature remain higher than the correlations between regions of positive curvature. At $\tilde{r} = 5/3$ the correlations between regions of negative curvature decrease dramatically and remain strongly anticorrelated out to $\tilde{r} = 8/3$. Correlations between two positively curved regions of interface and between regions of opposite curvature exhibit a decaying oscillation similar to that seen in the symmetric mixture. These correlations persist out to a radial distance of about $\tilde{r} = 7$. The correlations between regions of negative curvature extending farther, to greater than $\tilde{r} = 8$.

The plots for the asymmetric mixture show correlations between three primary and independently varying regions: regions of positive curvature, regions of negative curvature, and regions of opposite curvature. Because the MCD is not centered around zero, the asymmetric mixture has some positive curvature which is less than the average mean curvature. This curvature displays the same oscillation with distance as the negative curvature region. The interactions between these three primary regions produce very different contours, see particularly Figure 4.6e and h.

The correlations for each of the three primary curvature regions of the asymmetric mixture are shown in Figure 4.4b. When the positive curvature regions and opposite curvature regions are plotted against the corresponding regions for the symmetric mixture (Figure 4.7), there is remarkable similarity. The change in volume fraction and resulting changes to the MCD appear not to have much effect on correlations between similar

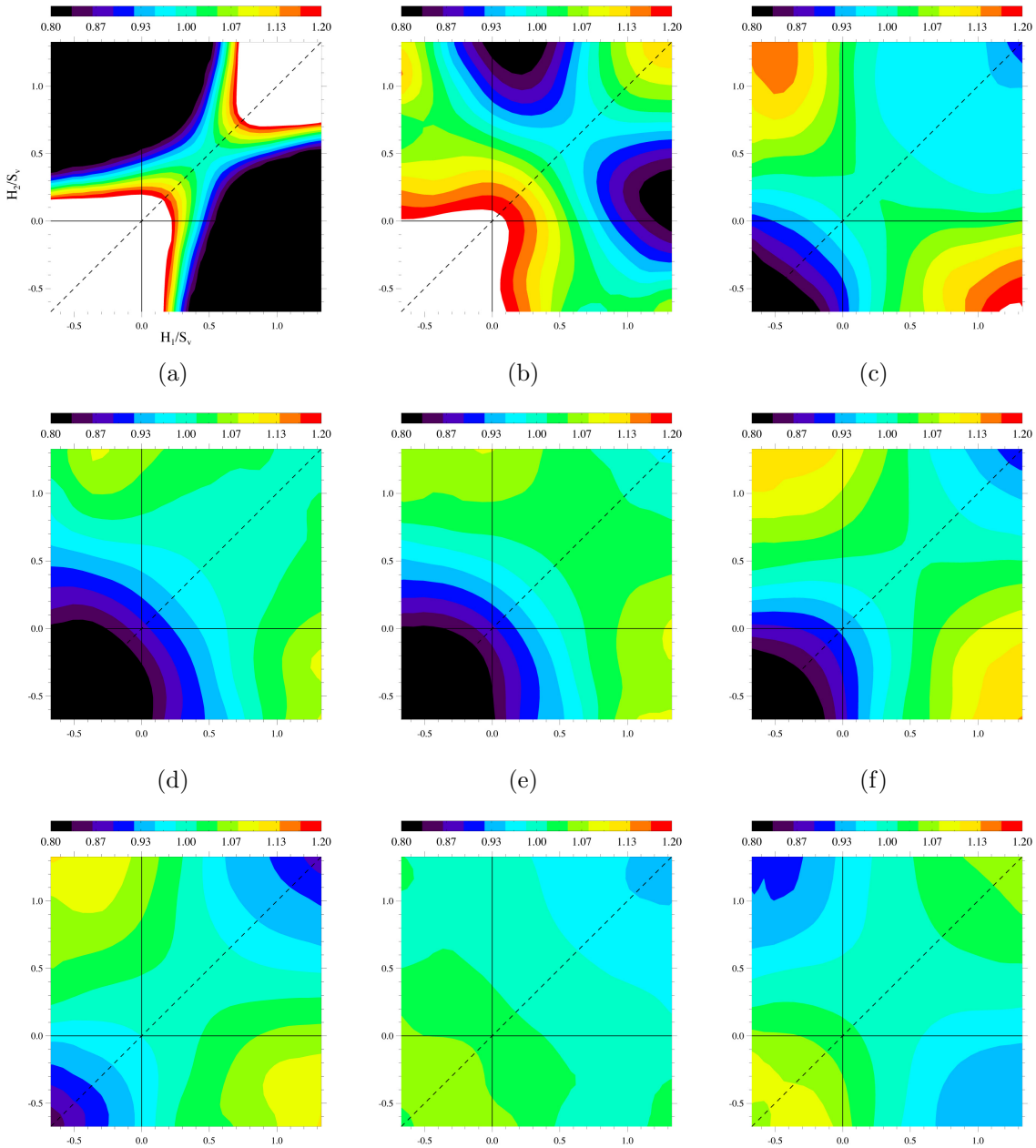

Figure 4.6. Spatial correlations in the asymmetric mixture for a variety of distances. Plots were constructed using a shell of thickness 1/3 at $\tilde{r}$ = a) 1, b) 4/3, c) 5/3, d) 2, e) 7/3, f) 8/3, g) 3, h) 10/3 and i) 4. White indicates a probability of greater than 1.2.

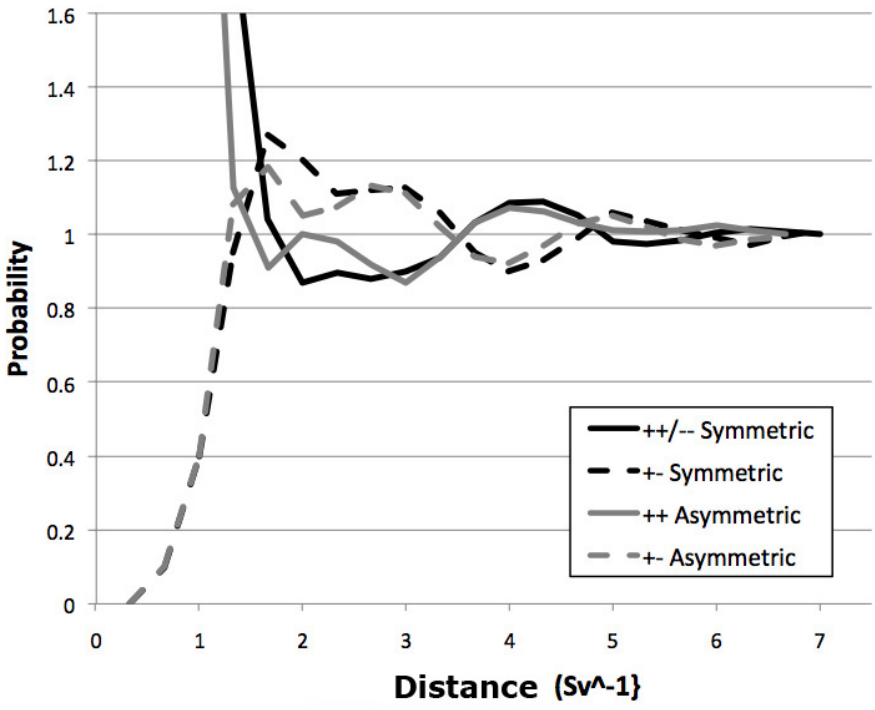

Figure 4.7. Comparison of the changes in primary correlations between the symmetric and asymmetric mixture.

positive regions of interfacial curvature and between regions of opposite curvature, when scaled by S_v^{-1} and to include the same fraction of total interface (here, 98%).

The correlation between regions of negative curvature in the asymmetric mixture, as plotted in Figure 4.4b, does not have a corollary in the symmetric structure. It has the strongest correlations and anticorrelations in space and seems to be unrelated to any correlations between other regions, oscillating with a different wavelength. This would indicate that what little negative curvature exists in this structure is clustered in large patches, some which visual analysis of the structure clearly shows to be the result of a rare pinching event in the majority phase. The largest of these patches have a radius on the order of S_v^{-1}, which is consistent with the correlation analysis. The correlations also

indicate a distance of approximately $2S_v^{-1}$ between patches which is responsible for the trough in Figure 4.4b.

Whereas in the symmetric mixture, the curvature difference necessary for diffusion must take place between regions of positive and negative curvature, that is not the case for the asymmetric structure. The MCD shows a large enough range of positive curvature present in the structure that the diffusion necessary for coarsening can occur between regions of high positive curvature and regions of moderate positive curvature. Thus the negative curvature plays a smaller role in the evolution of the asymmetric mixture. Diffusionally, negative curvature must cluster to avoid disappearing due to the large quantities of surrounding positive curvature. However, some negative curvature is geometrically necessary for a three-dimensional, bicontinuous structure to exist and thus the strong clustering effect. Some of these regions of negative curvature seem to be created by rare pinching events in the majority phase. Previous work [**47**] has shown that 36% minority phase, where this structure is, is just at the edge of where a stable, bicontinuous structure can exist. At lower volume fractions, there is not enough negative curvature present to maintain a stable structure, and the structure will break up into spherical domains.

4.4. Summary

The new methods of calculating radial distribution functions in three-dimensional real space use used to analyze spatial correlations in morphologically complex, bicontinuous mixtures. The mixtures were both symmetric and asymmetric, produced using conserved dynamics. This analysis was performed by calculating the RDF both for correlations between all existing values of curvature at a single radial distance, and between specific

curvature values identified primary correlation regions. It was found that in the symmetric mixture the long-range diffusive interactions yielded a correlations up to seven times the characteristic length. The observed correlations are attributed to interfacial smoothing effects at short distances, diffusional constraints at intermediate distances, and the repeating nature of the structure at longer distances. The form of the correlations has led to important observations on the nature of the morphology of this type of structure. The correlation analysis of the asymmetric mixture has provided important details about the nature of changes to a spinodal structure as it moves away from a critical quench, and possibly the nature of the breakup of such structures. The asymmetric mixture also showed correlations out to a distance of about $\tilde{r} = 7$, with particularly strong correlations between patches of negative curvature. Both structures have been found to reach unique scaled microstructures which can now be uniquely characterized using this spatial correlation information along with interface shape distribution.

CHAPTER 5

Experimental Procedure for Directionally Solidified Dendrites

5.1. Lead-Tin System

The lead-tin (Pb-Sn) binary system was used for all experimental work. It is a particularly useful model system for studying coarsening because the the interfacial energy is nearly isotropic, the coarsening rate is rapid, and the thermophysical parameters are well documented [**52**]. The low melting temperature (183°C) is also convenient for laboratory work. The Pb-Sn phase diagram is shown in Figure 5.1. Tin grows as a body-centered tetragonal crystal with dendrites historically thought to grow 12° away from the [110] direction toward the [001] direction [**53**]. However, more recent work has shown that tin dendrites tend to grow in several different directions depending on growth conditions so growth direction cannot be definitively stated. Lead is a face-centered cubic crystal [**54**]. Using the phase diagram, it was determined that an alloy composed of 69.1wt% Sn and 30.9wt% Pb was necessary to produce samples containing the desired 20% Sn dendrites and 80% Pb-Sn eutectic.

5.2. Processing

The alloy studied was created using high purity tin shot (99.99+%) and lead rod (99.9998%). About 600 grams of metal, composed of the desired fraction of lead and tin as discussed above, were melted in a graphite cup and cast in a chilled aluminum mold. In the machine shop, the ends of the resulting ingot were removed and the diameter was

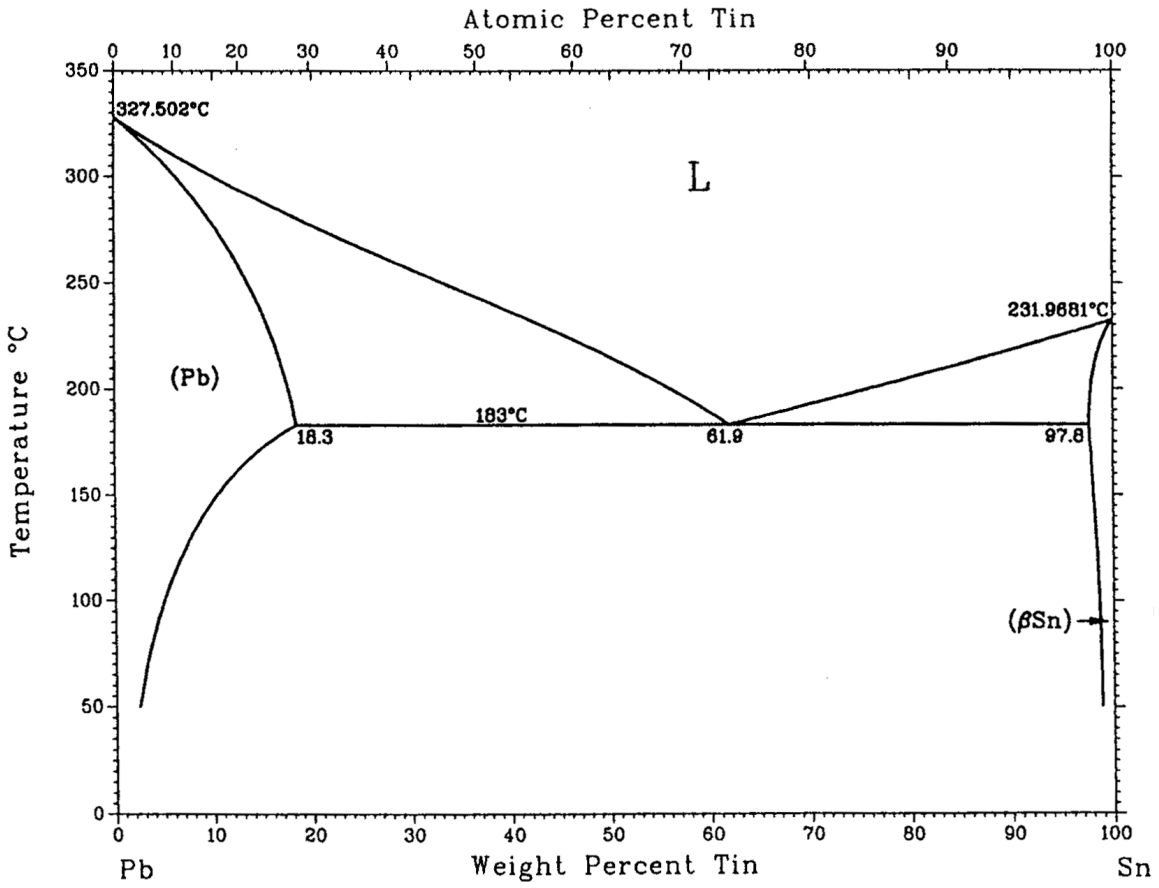

Figure 5.1. The Lead-Tin phase diagram.

reduced to 0.900 inches. The piece was then swaged, gradually decreasing the diameter to 0.500 inches.

Next, the alloy rod was directionally solidified in a Bridgeman-type furnace to produce a uniform dendritic microstructure. As opposed to a typical Bridgeman furnace which moves the sample through a stationary furnace, the alloy rod, contained inside a graphite tube, was held stationary in this custom-built furnace while the heating element moved up the length of the rod. This customized furnace was designed to minimize movement and vibration which can affect the resulting microstructure. A photo of the directional

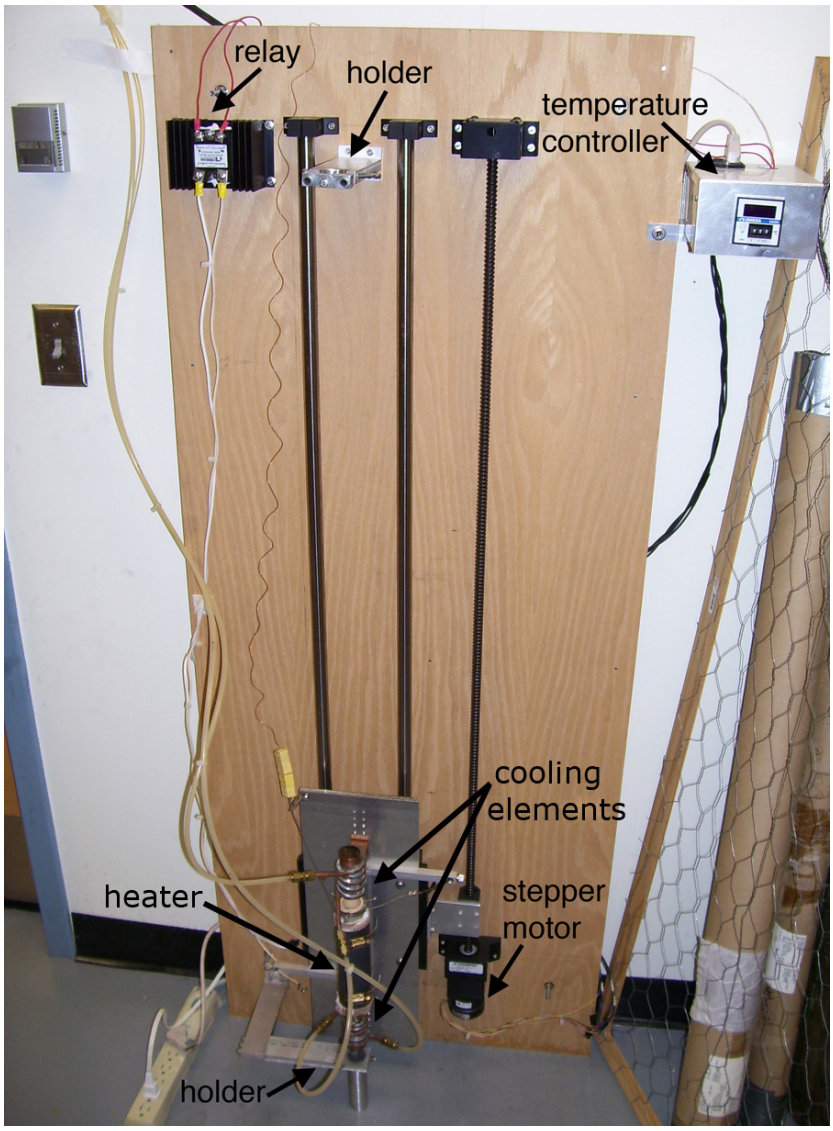

Figure 5.2. Image of the Bridgeman-type directional solidification furnace.

solidification furnace is shown in Figure 5.2. The heating unit consists of nickel-chromium wire wrapped around an alumina tube, and the cooling comes from chilled water through copper tubes. The velocity of the heater-cooler assembly, which equals the solidification velocity, is determined by a computer controlled stepper motor. For these experiments, the furnace maintained a temperature gradient of $1.22°C/mm$ and a velocity of $0.02mm/sec$.

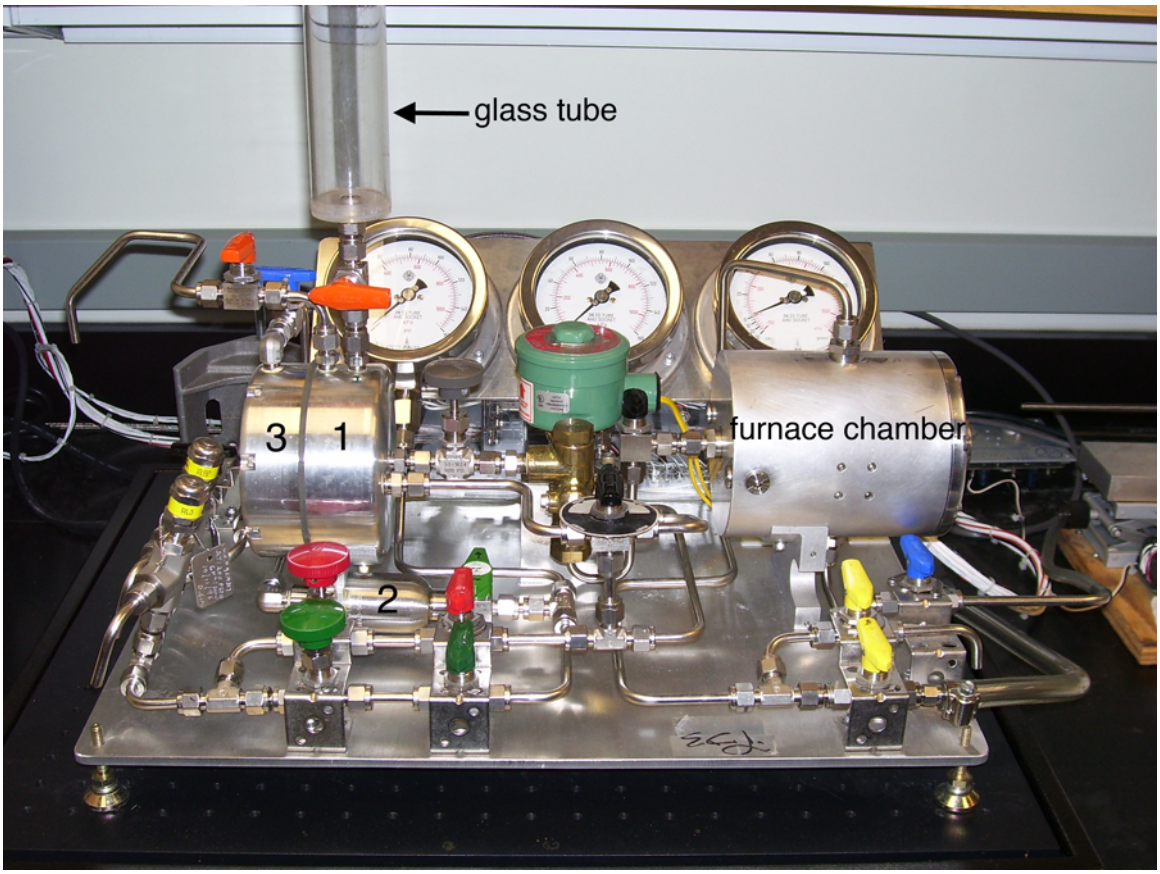

Figure 5.3. Photo of the coarsening furnace. To quench the samples, ice water was loaded into chamber 1 via the glass tube. At the end of the prescribed coarsening time, compressed air held in chamber 2 was automatically released into chamber 3, which pushed a rubber bladder forward into chamber 1 and forced the cold water into the furnace chamber.

The heater was calibrated to maintain a temperature of $250°C$ inside the metal rod, a temperature well above the eutectic temperature for this system.

After directional solidification, the rod was removed from the graphite tube and five samples, each about 6 mm thick, were cut from the middle of the rod. After further machining to reduce the samples to the exact dimensions of 0.4720 inches in diameter and 0.194 inches in height, each sample was isothermally coarsened in a special furnace

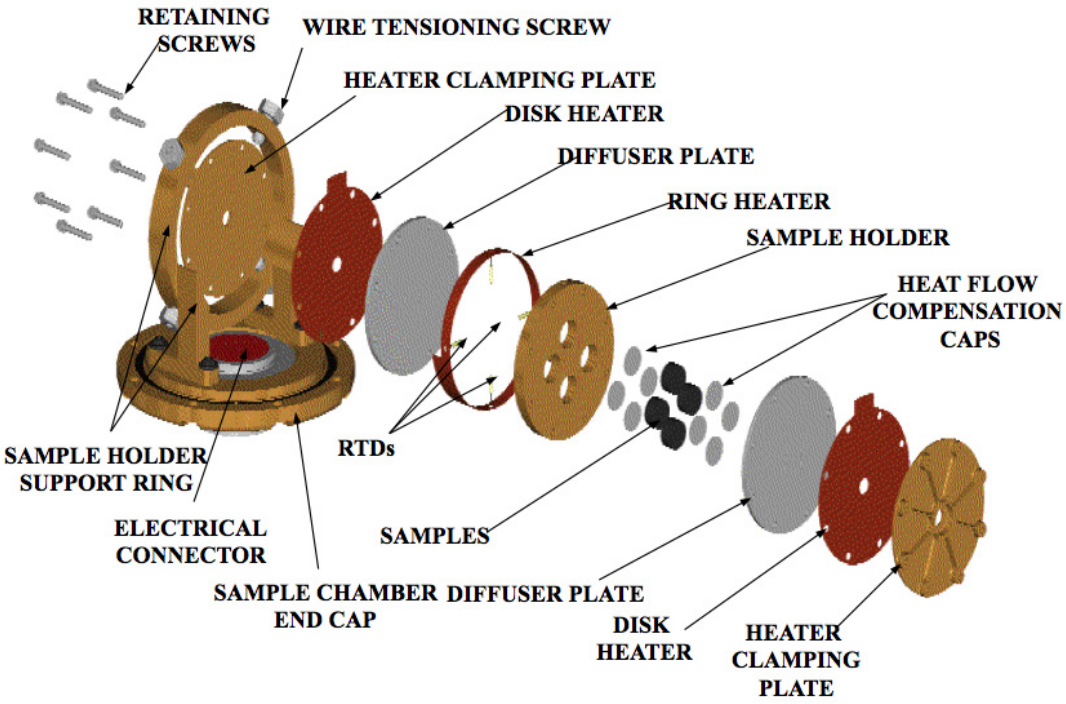

Figure 5.4. Schematic of the sample holder in the coarsening furnace. The heat flow compensation caps are necessary to equalize the thermal contact on all sides of the samples. For these experiments, only one sample was coarsened at a time, so the remaining three holes were filled with dummy samples.

for a length of time ranging from three minutes to two days. The coarsening furnace, seen in Figure 5.3, was build by NASA specifically for coarsening of Pb-Sn samples and is optimized to provide highly isothermal conditions. The complex sample holder, shown in Figure 5.4 and 5.5, is also designed to minimize temperature gradients.

For each coarsening time, a sample was loaded into the sample holder and the furnace chamber securely sealed. A vacuum pump was used to evacuate all air from the furnace chamber, pumping down for 24 hours before the coarsening run began. The vacuum is important for minimizing any temperature gradients during coarsening and so is maintained

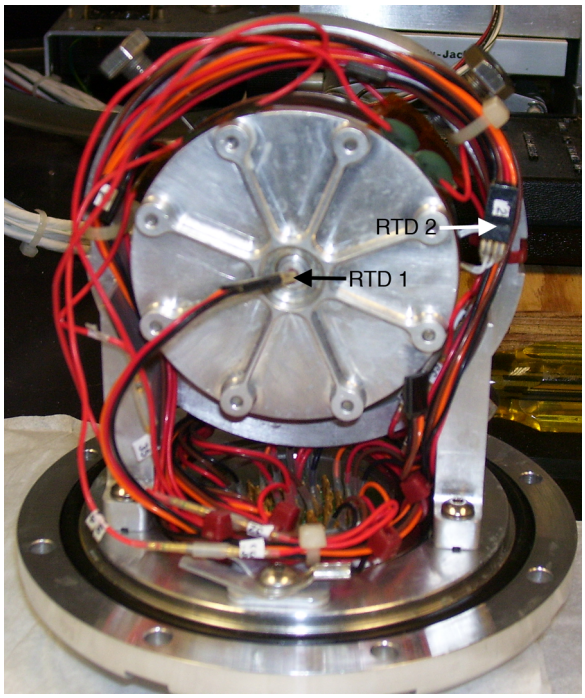

Figure 5.5. Photo showing the actual assembled sample holder with resistance temperature detectors (RTDs) indicated. The RTDs precisely measure the temperature inside the sample holder and allow the computer to direct current to the heating elements accordingly.

throughout the process. A computer controls the coarsening procedure, heating the samples to the set temperature of $185°C$, which is $2°C$ above the eutectic temperature for the Pb-Sn system. The computer uses feedback from the RTDs to hold the temperature precisely at $185°C$ for a specified number of seconds, then quenches the sample holder with ice water. This drops the temperature of the sample to well below the eutectic temperature almost instantly, preserving the form of the coarsened dendrites. This quenching method, along with coarsening the samples only slightly above the eutectic temperature, has been shown to effectively minimize the deposition of additional material at the interface during cooling [**55**]. To avoid changes to their structure after coarsening, the samples are held

in a freezer at $-80°C$ when not in use. This entire process for creating and coarsening Pb-Sn samples is also described extensively in [**56**].

5.3. Automated Serial Sectioning

To obtain the three-dimensional data needed for image reconstruction, a semi-automated serial sectioning device [**57**], shown in Figures 5.6 and 5.7, was used. To use this machine, samples are mounted on glass slides, which are held by suction on top of a movable stage. The stage is translated in the y-direction underneath the diamond-tipped blade of the milling machine which removes a uniform amount of material from the top of the sample (here, $4.75\mu m$). The speed of the stage during milling is approximately 0.8 mm/s. The sample continues in the y-direction, stopping under three nozzles which automatically etch, rinse and dry the surface of the sample. For Pb-Sn samples, the etchant is 0.5% nitric acid in methanol, the rinse is isopropanol, and the drying is done with compressed air. The etchant is left on the surface of the sample for 4-6 seconds. The stage then moves the sample under a microscope and attached camera. A digital image of the etched surface is taken, while the exact position of the stage is recorded using a linear variable differential transformer (LVDT). Because the stage moves only in the y-direction, and the sample is not removed from the stage during the sectioning process, no rotational or x-translational misalignment is introduced into the images. However, there is some variance in the image capture position in the y-direction, so the LVDT readings are used later to align the images. This method is able to produce a stack of images which are aligned to better than $0.5\mu m$.

Figure 5.6. The microtome used for serial sectioning of samples.

All images here were taken with a 5x objective lens, producing a resolution of $1.03\mu m$ in the x- and y-directions. After the image is taken, the stage returns to the starting position and the cutting blade is lowered $4.75\mu m$. Because the etching nozzles and the microscope/camera are directly mounted on the milling machine, a uniform distance from the sample surface is maintained, ensuring uniform etching and well focused pictures. Once the procedure has been set up, about twenty sections per hour can be obtained. Approximately 100 sections were obtained for all samples discussed here. The process of converting the stack of raw images to a three-dimensional reconstruction will be discussed in Section 5.5.

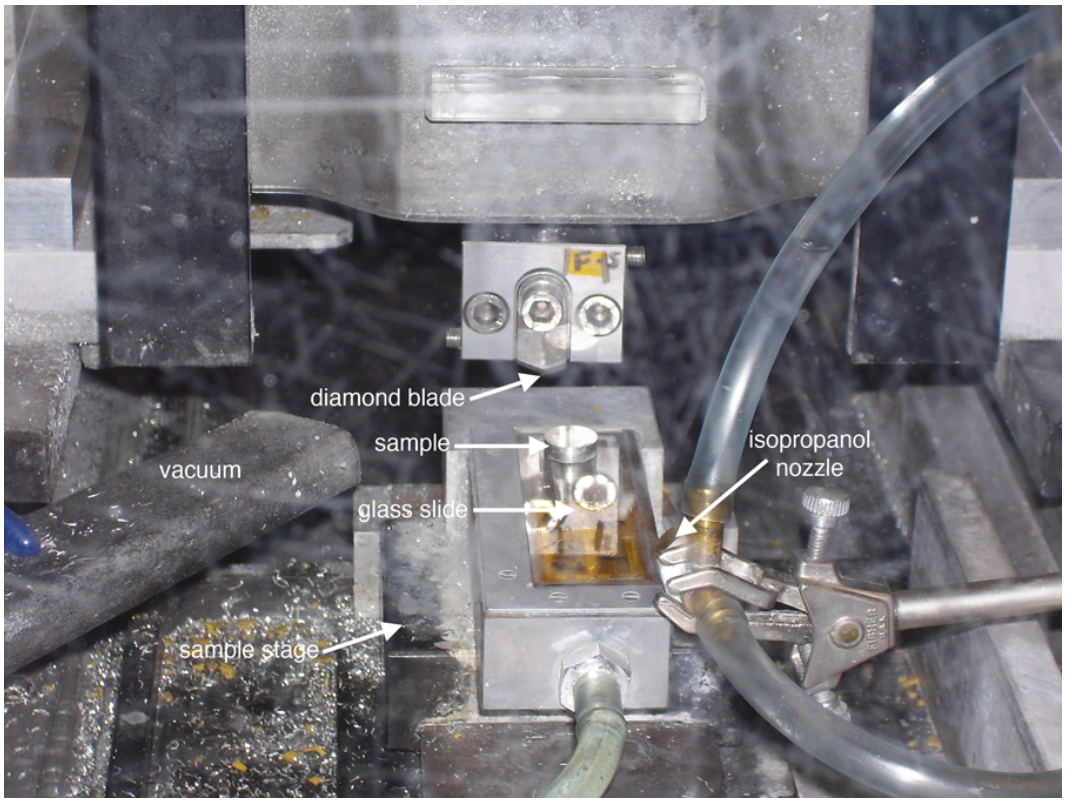

Figure 5.7. A close-up of the sample about to pass under the blade during sectioning. The sample is sprayed with isopropanol to lubricate the cutting surface, and a vacuum nozzle is present to capture chips created during milling.

5.4. Initial Observations of Dendritic Samples

Five samples of the directionally solidified Pb-69.1wt%Sn were coarsened for three minutes, twenty-eight minutes, one hundred minutes, 486 minutes (about eight hours) and 2280 minutes (48 hours). Images of the etched surfaces of the five samples are shown below in Figure 5.8, taken using a tripod and standard digital camera. The longest coarsening time shows too much sedimentation to provide usable data. The other four samples were sectioned, and 3D reconstructions and analysis are shown later (Chapter 6).

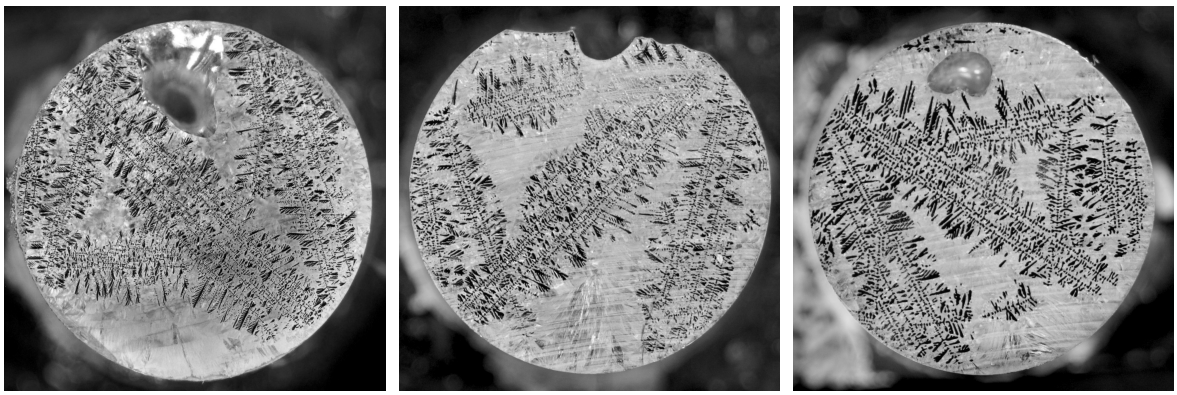

(a) (b) (c)

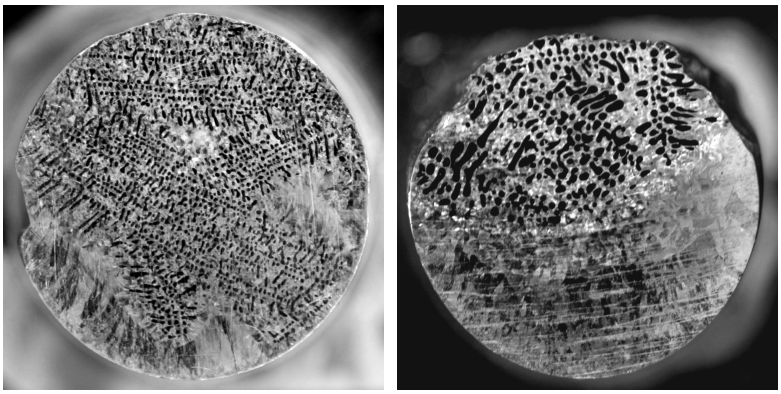

(d) (e)

Figure 5.8. Effect of coarsening on dendritic microstructure after (a) 3 minutes (b) 28 minutes (c) 100 minutes (d) 8 hours and (e) 2 days. The longest time shows complete sedimentation. Images were taken using a tripod and digital camera.

A montage of 59 images was made of the 486 minute sample (Figure 5.9), using a digital camera and 5x lens, so that enough detail would be visible to obtain an accurate volume fraction measurement. From this image, the sample was found to be 22% dendritic and 78% eutectic by volume (hence, 22% solid during coarsening). The dendritic region inside the box in Figure 5.9(b) has a volume fraction of about 38%. Previous work on higher volume fractions have found samples with an overall and local volume of 43%

solid [**58**]. This seems to indicate that that at some point between about 30% and 40% solid, the density of the dendritic regions remains relatively constant and large, empty regions of eutectic form to account for the overall lower volume fraction solid. For the three-dimensional reconstructions and analysis, effort was made to obtain data from both the dense interior dendrite region and the dendrites near the edge of the dense regions which were able to grow more freely.

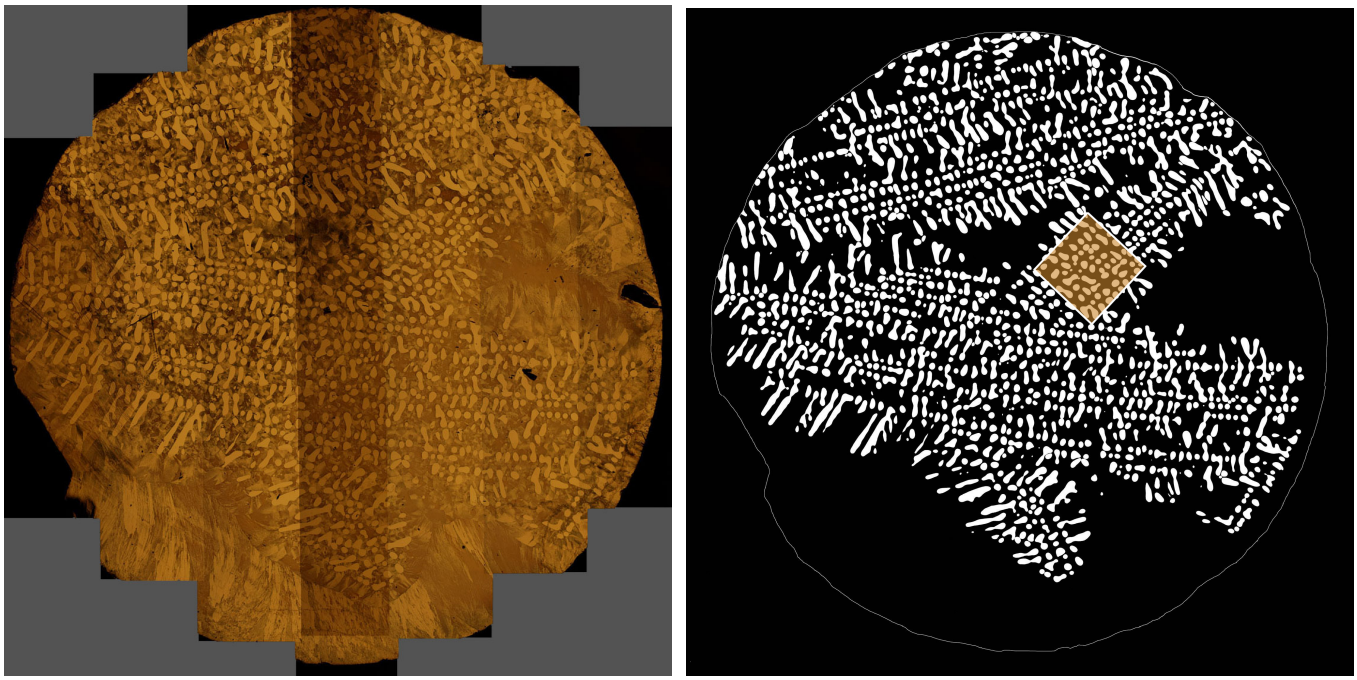

(a) (b)

Figure 5.9. Montage of eight hour coarsened sample (a) before and (b) after thresholding. The area inside the box contains 38% solid. The overall sample is 22% solid.

5.5. Three-Dimensional Reconstruction

The creation of a three-dimensional reconstruction from an experimentally obtained microstructure is a complex and multi-step process, requiring segmentation and alignment

of the images obtained from the serial sectioner and then the creation and manipulation of the actual 3D mesh.

5.5.1. Segmentation and Alignment

While the process of obtaining the sequential images using serial sectioning generally takes about a day and a half, processing the images for conversion to a 3D model takes much longer, sometimes a month or more. Figure 5.10 shows the steps taken to obtain a correctly segmented image. This work is done in Adobe Photoshop. The RAW image is first converted to grayscale, so that each pixel has a value between 0 (black) and 255 (white). The image can then be automatically thresholded, or converted to binary, so that all pixels with a value higher than the threshold value (in general, 127) become white and all those with a lower value become black. The meshing algorithm can then create an interface running along the boundary between black and white.

However, thresholding of the images is made more difficult because the images often contain flecks of debris, improper etching, water spots from the alcohol used to rinse off the etchant, variations in brightness due to misalignment of the microscope components, or other imperfections. Special filters in Photoshop can be used to minimize some of these issues, but as Figure 5.10(c) shows, there will always be some imperfections which can only be corrected by hand, and this takes time. Images of shorter coarsening time samples, with more complex morphologies, take the longest. One must also take extreme care during thresholding and subsequent cleaning that the location of the interface does not move. Thresholding at a value that is too high will create bridges between unconnected regions, altering the morphology of the meshed structure. Often it is difficult to tell whether

two regions should be connected or not, both during thresholding and later during the smoothing process (see next section) because of insufficient resolution in the images.

Semi-automated routines for thresholding have been developed using edge detection software, but these work best for systems of spherical particles and provide no time savings for the dendritic samples discussed here. Improvements to the segmentation process would clearly have a great impact on this type of work.

Once the entire stack of images has been carefully segmented, the images are stacked and aligned using the data recorded by the LVDT (as discussed in section 5.3). Figure 5.11 shows a schematic of the alignment process. From this point on, all work was done using programs written in IDL (Interactive Data Language), a language by ITT Visual Information Solutions, unless otherwise noted. IDL creates a polygonal mesh which follows the boundary between the two regions of the 3D binary array and, if the segmentation process was done well, accurately represents the morphology of the sample.

5.5.2. Smoothing

Much attention has been given to the smoothing of these structures. In the past, all smoothing has been done to the three-dimensional array which comes from the stacked binary images. Just before this work began, an improvement was developed that allowed for anisotropic smoothing, i.e. more smoothing in the z-direction than in the x-y plane for highly directional, long coarsening time samples [**56**]. Because of the extremely fine scale of this structure, this numerical smoothing caused significant microstructural changes, such as the welding of some dendrite arms and the pinching off of others. A new method

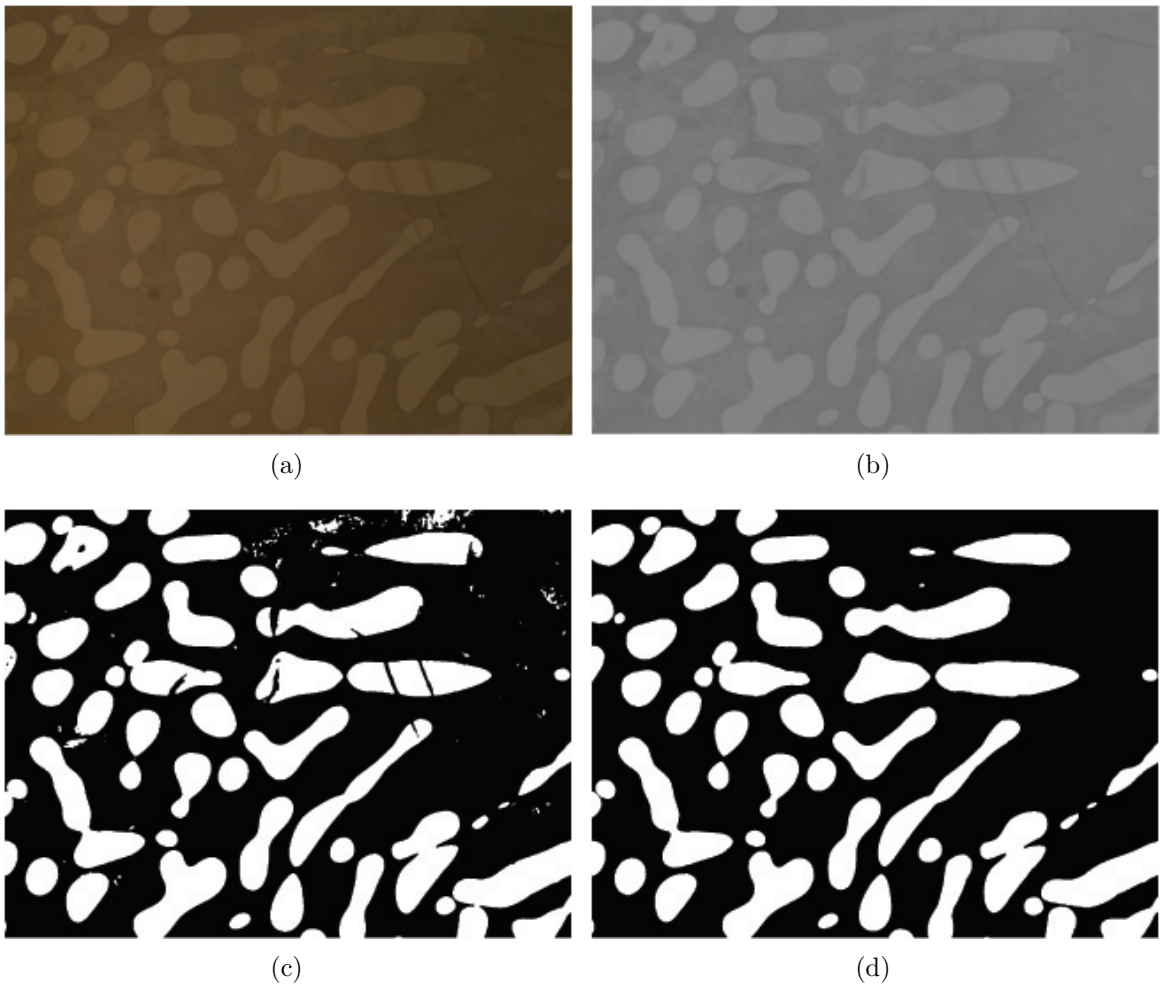

Figure 5.10. Segmentation process for part of the 100 minute coarsened sample, Pb-69.1wt%Sn. (a) The initial raw image as captured by the microscope. (b) After conversion to grayscale, equalization of brightness across image, and noise reduction. (c) After initial thresholding. (d) Final image after manual cleaning.

of first meshing the surface of the structure in IDL, then smoothing the mesh has brought dramatic improvements and increased flexibility to the smoothing process.

Although the use of mesh smoothing produced many favorable results, it also introduced some new problems. During the mesh smoothing process, IDL resizes the polygons

Figure 5.11. Schematic of alignment process

of the mesh, and in some cases constricts them so far that they have an area of zero. This causes the Simview program, which calculates areas and curvatures of all interfacial patches, to produce NANs (values that are Not A Number) and renders it unable to correctly calculate curvatures.

This issue was minimized by using a compromise of minimal volume smoothing and careful mesh smoothing. Using the *mesh_validate* command on the smoothed mesh in IDL was found to reduce the occurrence of NANs, but mesh smoothing also has the problem of being less effective at removing the "wedding cake" structure, a residual terracing effect from the sectioning process. Some reduction in the wedding cake effect was obtained by making use of the *fixed_vertices* command during mesh smoothing to fix points known to be accurate (based on the original arrays) and strongly smoothing everything between them. All these contradictory issues must be balanced, and significant advances can still be made in the smoothing process to produce a more accurate microstructure. Figure 5.13 shows the improvements made to the smoothing process, but room remains for improvement.

A final variable which can affect smoothing of the structure is the reduction factor of the images. When the binary images are read into IDL, they are generally reduced by some factor between 2 and 5. This decreases the resolution of the images somewhat, but is necessary to obtain arrays which are small enough to be handled by current computers.

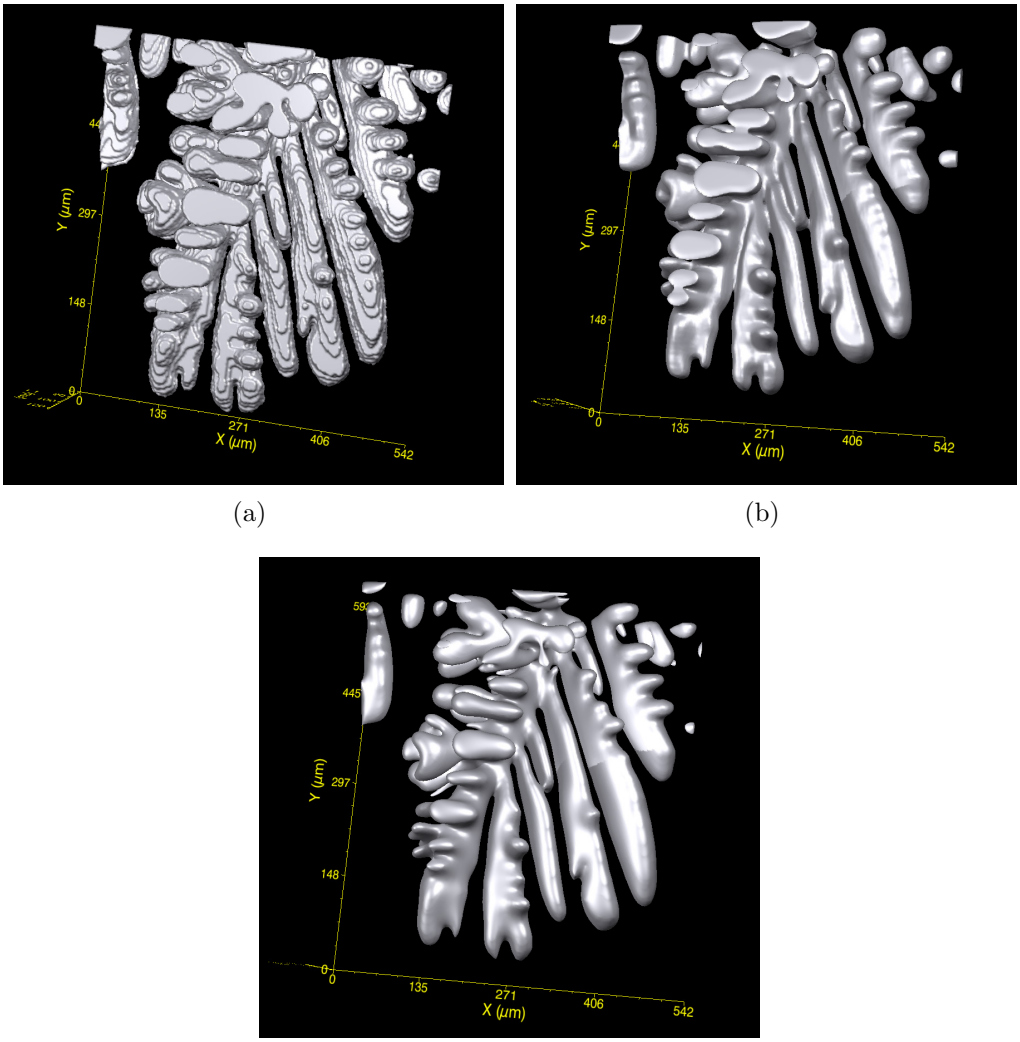

(a) (b)

(c)

Figure 5.12. Three versions of the same segment (a) without smoothing, where individual sections are clearly visible, (b) with too much volume smoothing, showing welding of some features, (c) with too much mesh smoothing, showing shrinkage and distortion of some features.

Reduction has a similar effect as volume smoothing the stack, so it is both useful for removing the wedding cake effect and detrimental when it causes welding of small features. Various reduction factors for the shorter coarsening times were explored to minimize

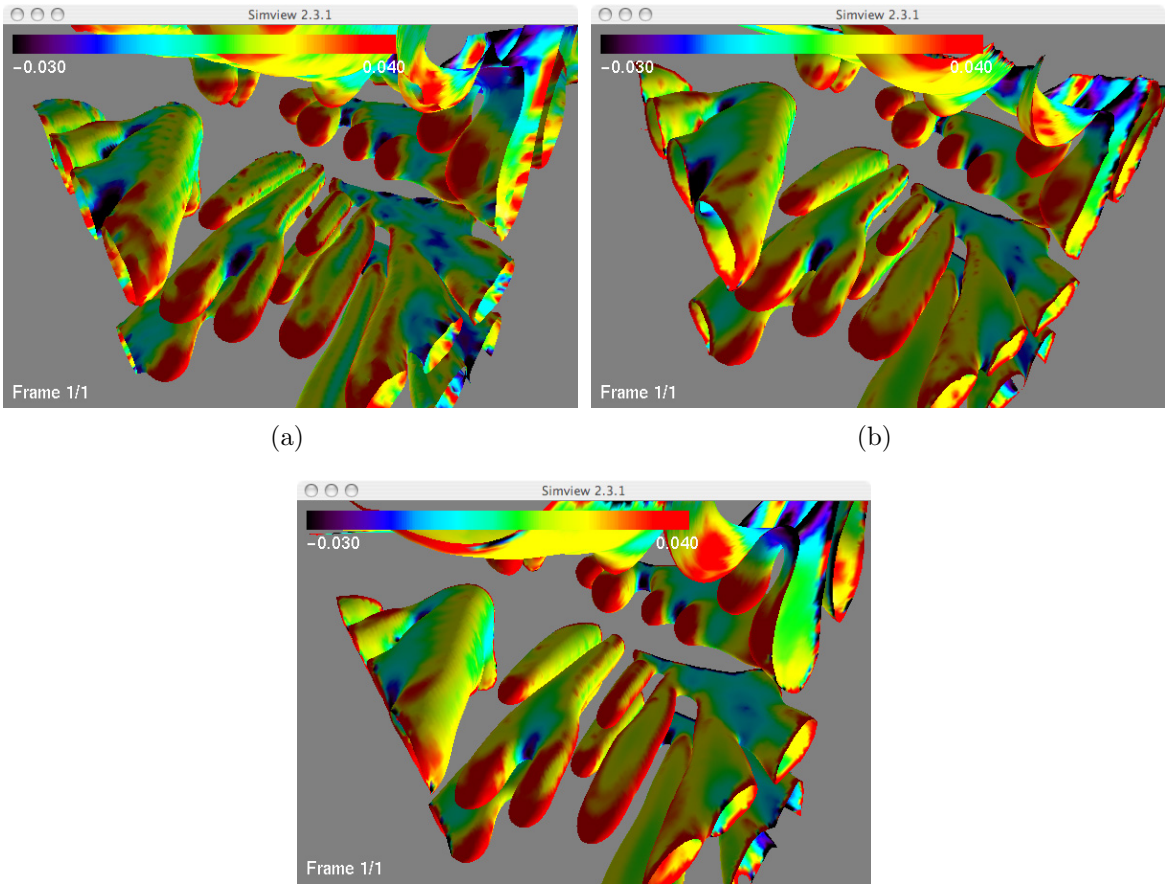

Figure 5.13. Three versions of the same structure, colored by mean curvature to show effect of various smoothing methods. (a) Volume smoothing (b) Mesh smoothing (c) Combination of slight volume smoothing and optimized mesh smoothing, showing curvature which changes smoothly across the structure with minimal patchiness.

welding effects. It should be noted that, for this setup, a reduction of 5 has generally been used because it produces the most nearly cubic voxels.

The parameters used for smoothing each structure are given in Table 5.1. All smoothing parameters were the same for the dense and non-dense regions except where noted. The values used for each parameter were a result of extensive trial and error. These are

Coarsening (min)	*Reduction*	*Volume Smoothing*	*Threshold*	*Fixed Point Mesh Smooth. (λ/iterations)*	*Mesh Smoothing (λ / iterations)*
3	3	5	142 , 127	0.06 / 60	0.05 / 75
28	5	3	127	0.05 / 60	0.05 / 50
100	5	5	127	0	0.05 / 60
486	5	5	127	0	0.05/60 , 0.06/70

Table 5.1. Smoothing parameters for each sample. Where two values or sets of values are separated by a comma, the first is that used for the dense region and the second that used for the non-dense region. Other parameters were the same for both regions.

the values which were deemed to be the ones producing the most accurate representation of each structure. However, any smoothing process inevitably introduces some error, and having used different smoothings for each structure introduces different changes to the resulting ISDs and other measurements which are confounded with any actual changes due to evolution of the structure. This is yet another reason why systematic study of and improvement to the smoothing process would prove very helpful.

CHAPTER 6

Analysis of Low Volume Fraction Dendrites

6.1. Dense Regions

For each of the four usable coarsening times (those not overly affected by sedimentation), the region for imaging was chosen such that both dense regions and non-dense regions (where free growth is approximated) were captured. All calculations were done separately for the two regions of each sample. The three-dimensional reconstructions of the dense dendritic regions are shown in Figures 6.4-6.7. The specifics of each structure are given in Table 6.1.

The change in S_v with time is plotted in Figure 6.1. As predicted, S_v^{-3} increases linearly with time. The $t^{1/3}$ dependence indicates that despite any movement due to sedimentation, etc., the coarsening kinetics are still diffusion controlled. Figure 6.2 shows the small difference in slope between the specific S_v^{-1}, S_v^{-1*}, for the dense regions versus the non-dense regions. S_v^{-1*} is defined as the surface area divided by the volume of the solid instead of the volume of the entire sample, and therefore can be measured for samples that are not uniformly filled by solid. The increased deviation from linear in the non-dense samples is likely a result of the small sample size.

Another measure of these systems is the mean curvature distribution (MCD), which is particularly for the spatial correlation work which looks only at mean curvature (see Chapter 7 for analysis of RDFs for dendritic samples). The scaled and unscaled MCD for

Coarsening (min)	*Local Volume Fraction (%)*	*Stack Size (μm)*	*S_v ($1/\mu m$)*	*Specific S_v ($1/\mu m$)*
3	37	998 x 1242 x 399	0.0291	0.0840
28	37	1777 x 932 x 394	0.0248	0.0680
100	36	1545 x 1545 x 475	0.0166	0.0472
486	32	1880 x 2575 x 523	0.0101	0.0318

Table 6.1. Characteristics of the dense regions from samples. S_v is the surface area divided by the volume of the sample box, while specific S_v refers to the amount of surface area divided by the volume of only the dendrites.

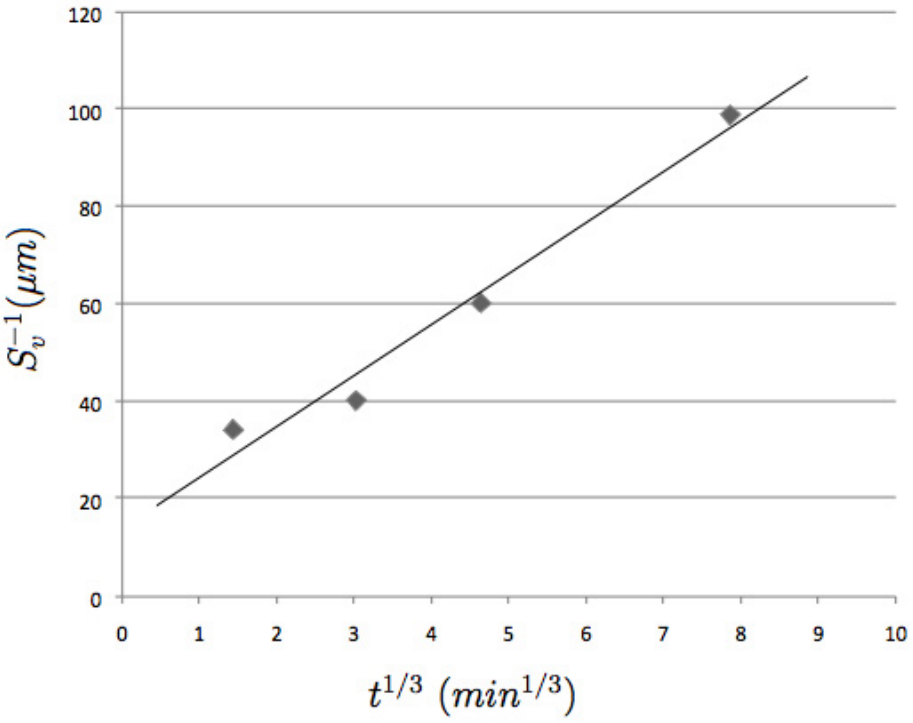

Figure 6.1. S_v^{-1} as a function of the cube root of coarsening time for all four samples, showing a strong linear dependence.

the dense region of these four samples is given in Figure 6.3. Viewed alone, the MCDs would seem to indicate coarsening in a self-similar fashion. However, mean curvature

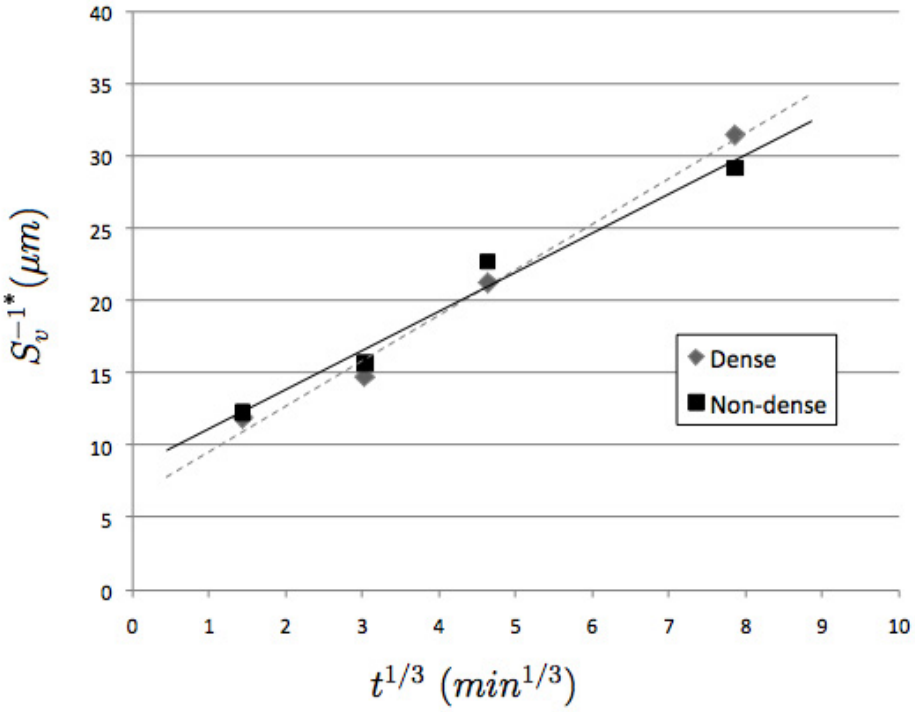

Figure 6.2. Specific S_v^{-1} as a function of the cube root of coarsening time for the dense regions versus the non-dense regions.

alone does not fully capture the type of interface present, and so a more comprehensive method of measuring curvature is developed in Section 6.3.

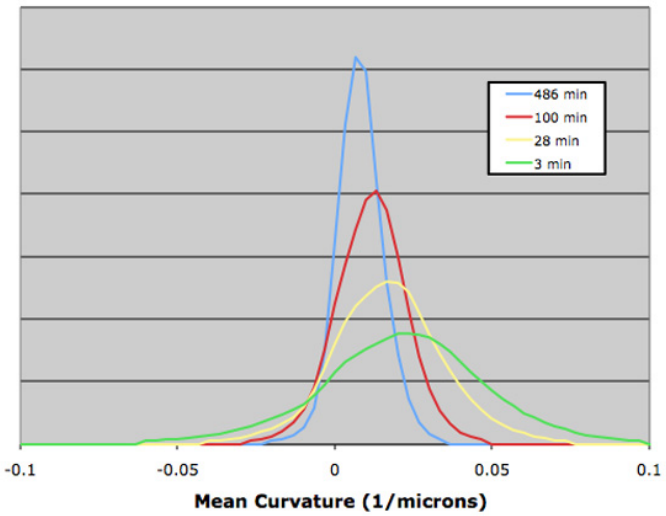

(a)

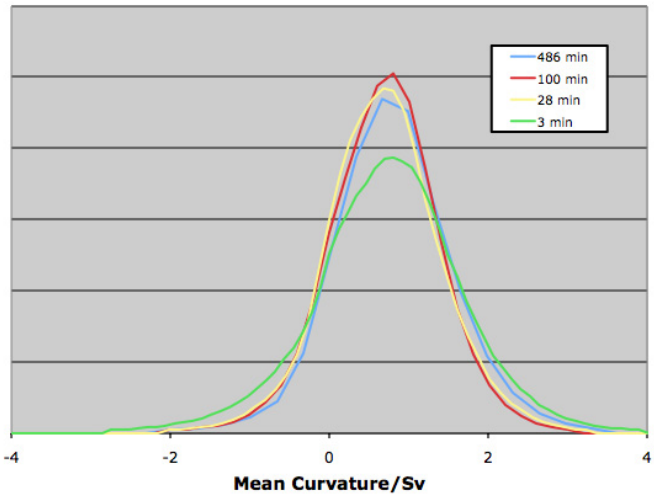

(b)

Figure 6.3. The evolution of the (a) unscaled and (b) scaled MCD of the dendritic samples with coarsening time.

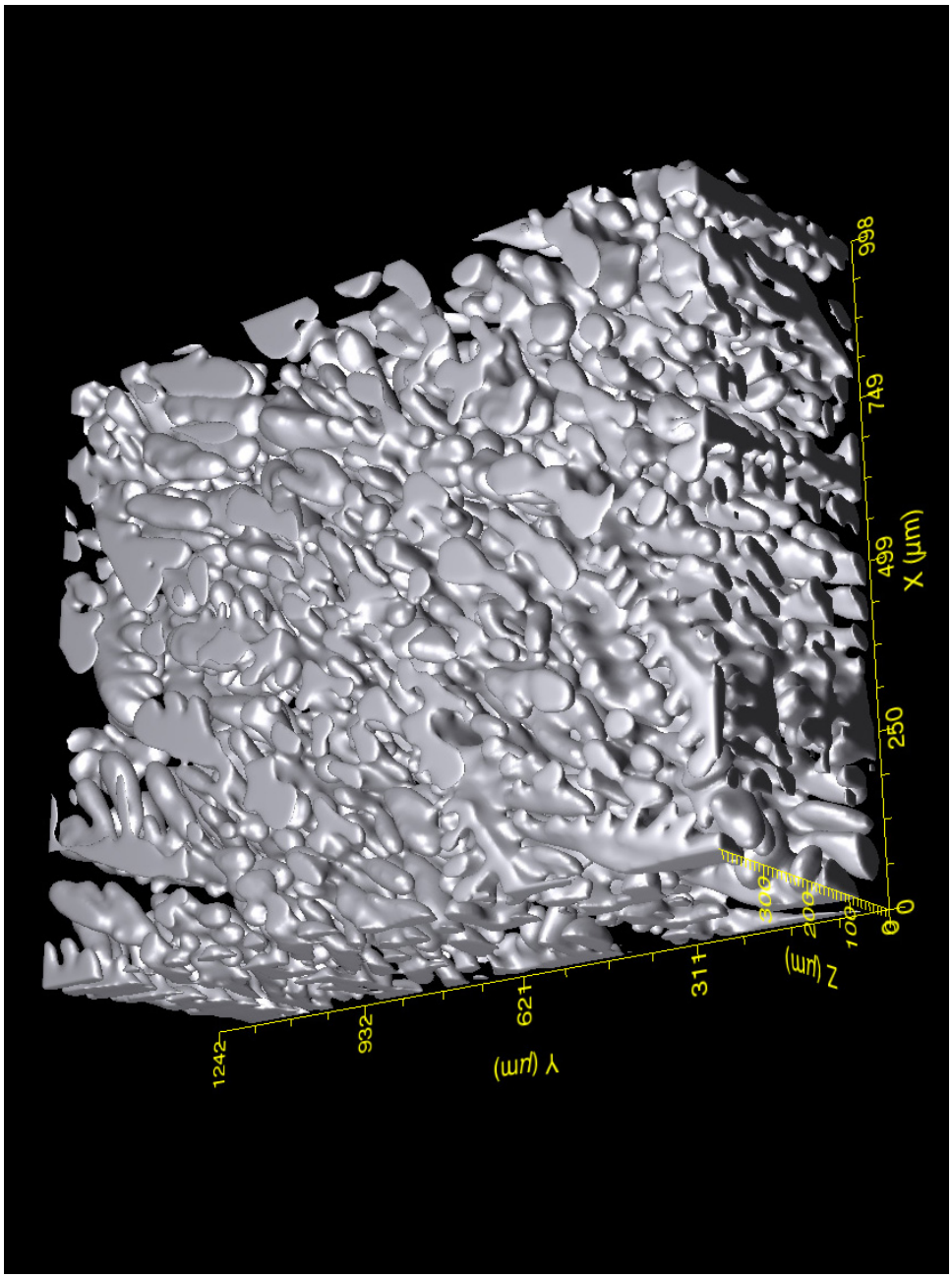

Figure 6.4. Three-dimensional reconstruction of the 3 minute coarsened sample, dense region, locally 37% solid.

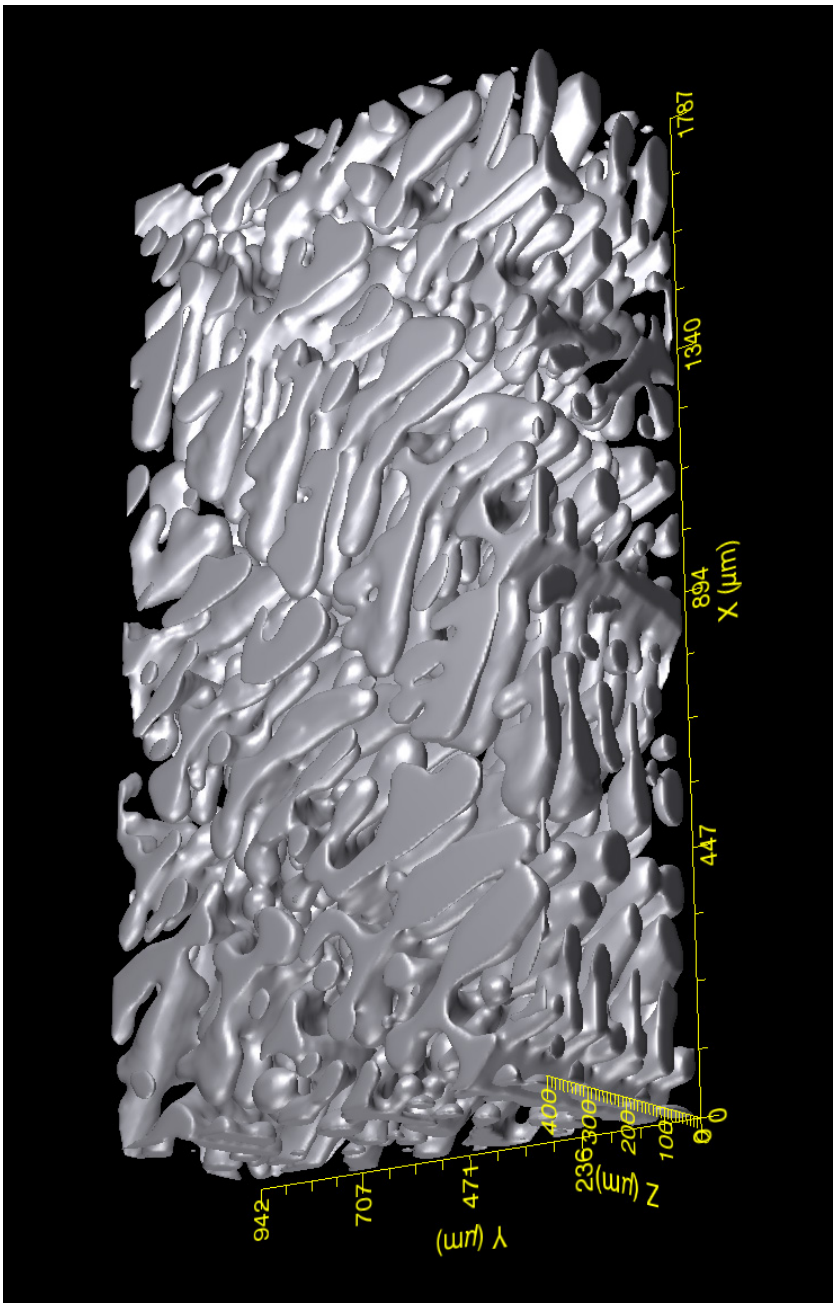

Figure 6.5. Three-dimensional reconstruction of the 28 minute coarsened sample, dense region, locally 37% solid.

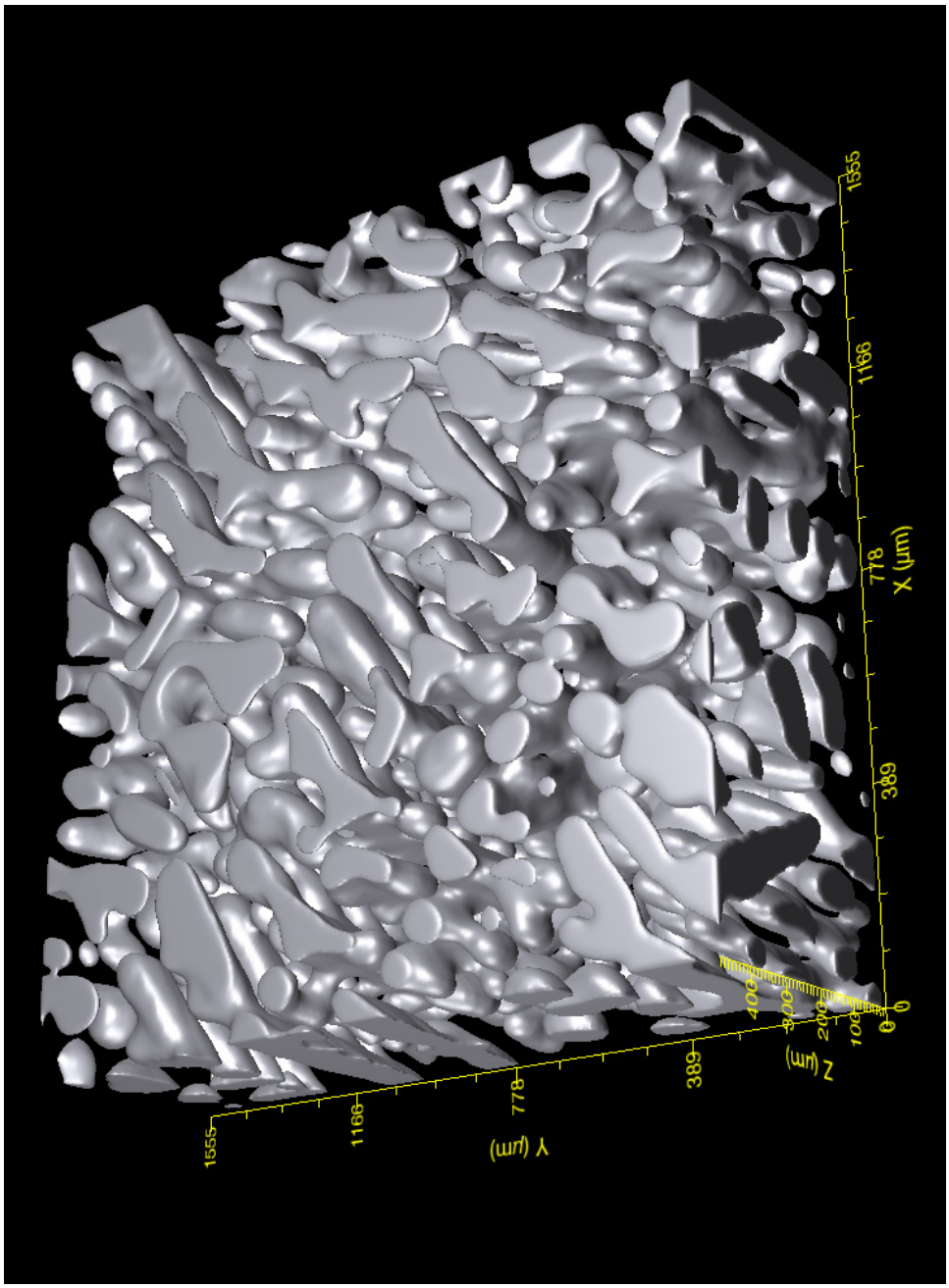

Figure 6.6. Three-dimensional reconstruction of the 100 minute coarsened sample, dense region, locally 36% solid.

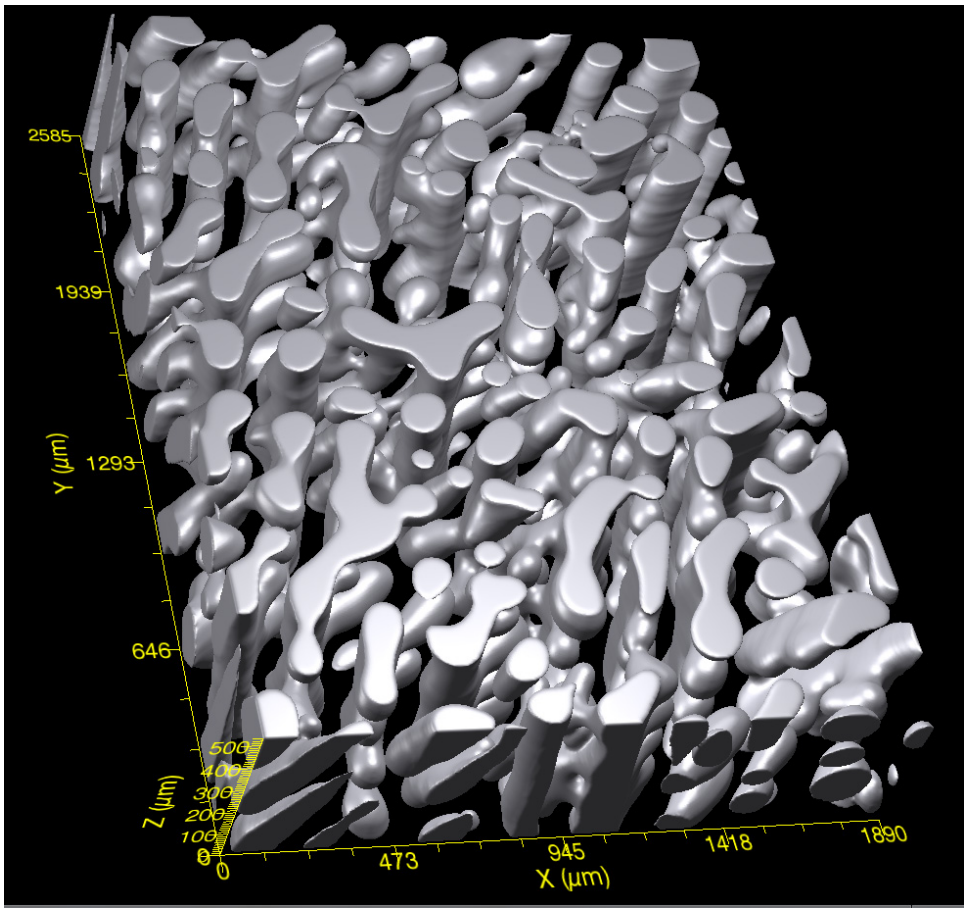

Figure 6.7. Three-dimensional reconstruction of the 8 hour coarsened sample, dense region, locally 32% solid.

6.2. Non-dense Regions

The three-dimensional reconstructions of the non-dense dendritic regions are shown in Figures 6.8-6.11. The specifics of each structure are given in Table 6.2. Where to crop the structures to include only the "non-dense" region was somewhat subjective, so the values given in the table and the analysis in the following sections reflect the exact structures being examined and may vary depending on how the region is defined. While

Coarsening (min)	*Local Volume Fraction (%)*	*Stack Size (μm)*	*Specific S_v ($1/\mu m$)*	ΔS_v *(%)*
3	25	1928 x 1091 x 390	0.0814	3.1
28	21	2719 x 1051 x 394	0.0636	6.5
100	20	2627 x 1288 x 470	0.0441	6.6
486	18	1442 x 1700 x 523	0.0343	-7.9

Table 6.2. Characteristics of the non-dense regions from samples, including the percent change in specific S_v from dense region. As the dendrites do not completely fill the sample boxes, it does not make sense to measure S_v for these samples.

these are not truly free growing dendrites, these regions do approximate dendrites growing unconstrained into a liquid, developing extensive secondary and tertiary branches.

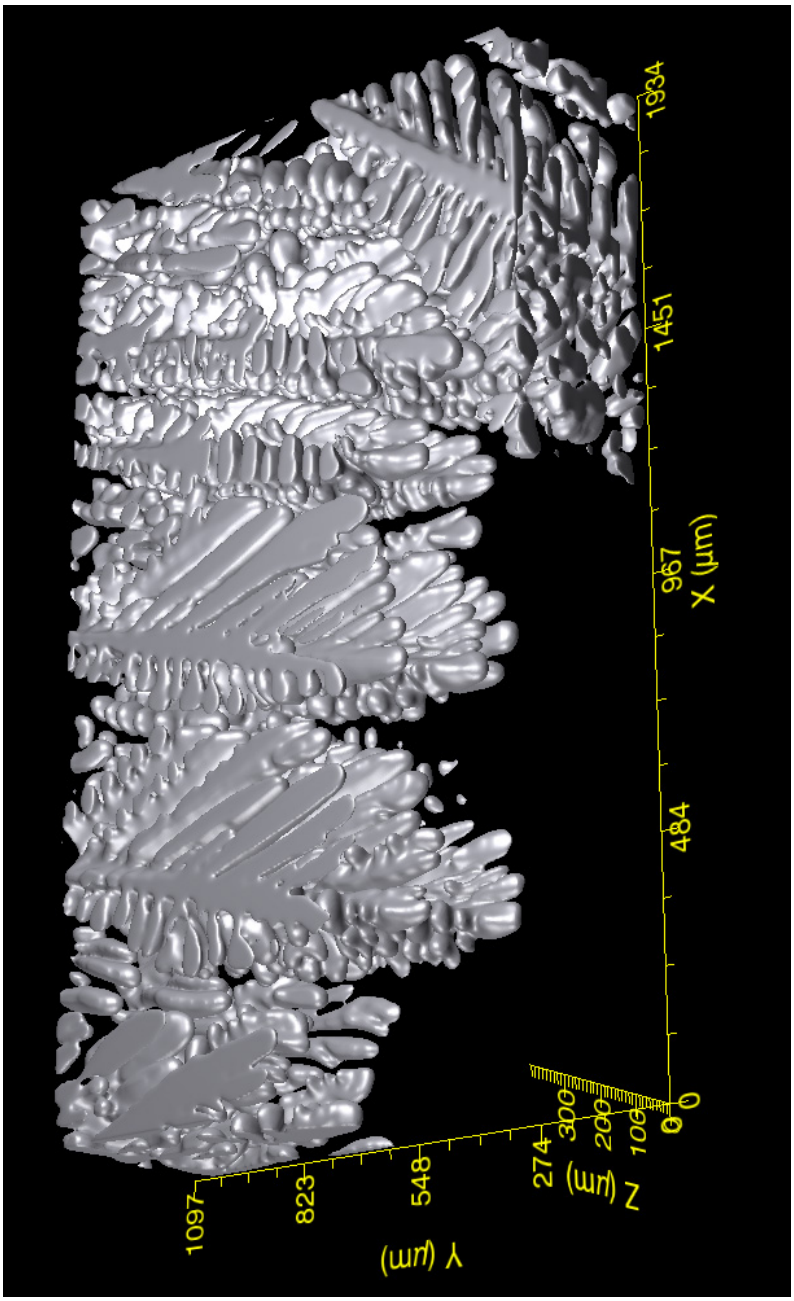

Figure 6.8. Three-dimensional reconstruction of the 3 minute coarsened sample, non-dense region.

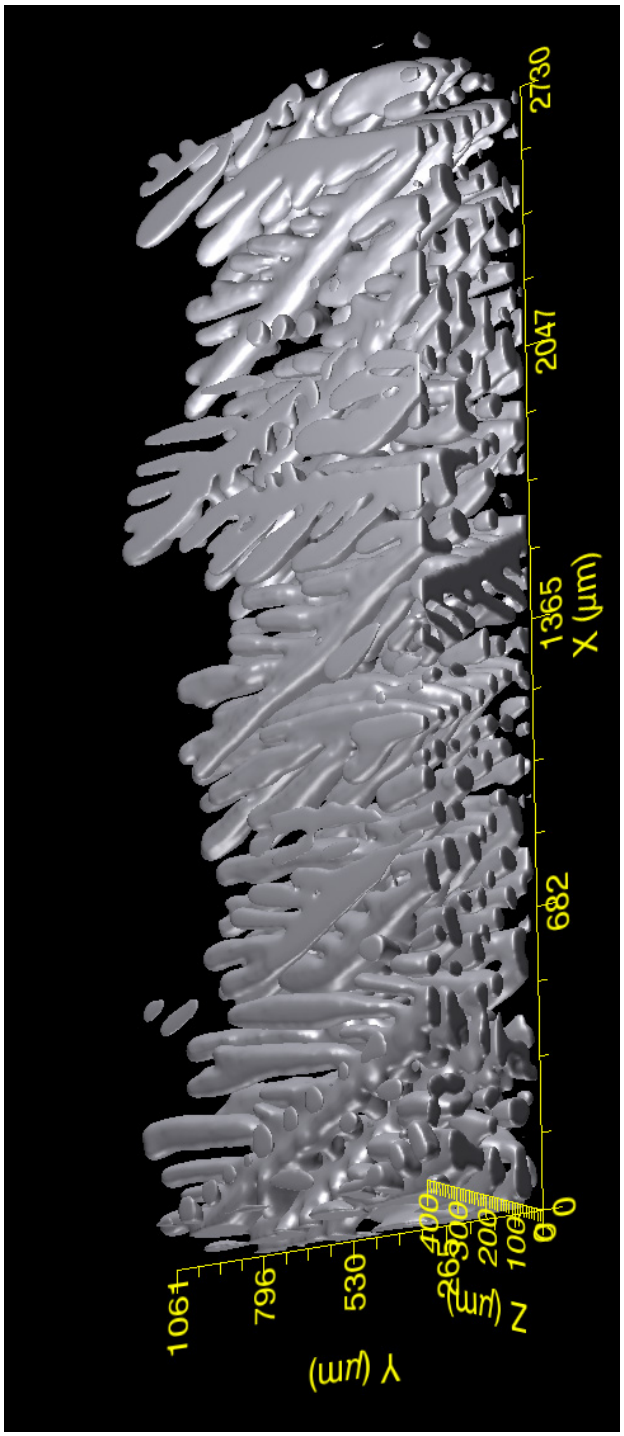

Figure 6.9. Three-dimensional reconstruction of the 28 minute coarsened sample, non-dense region.

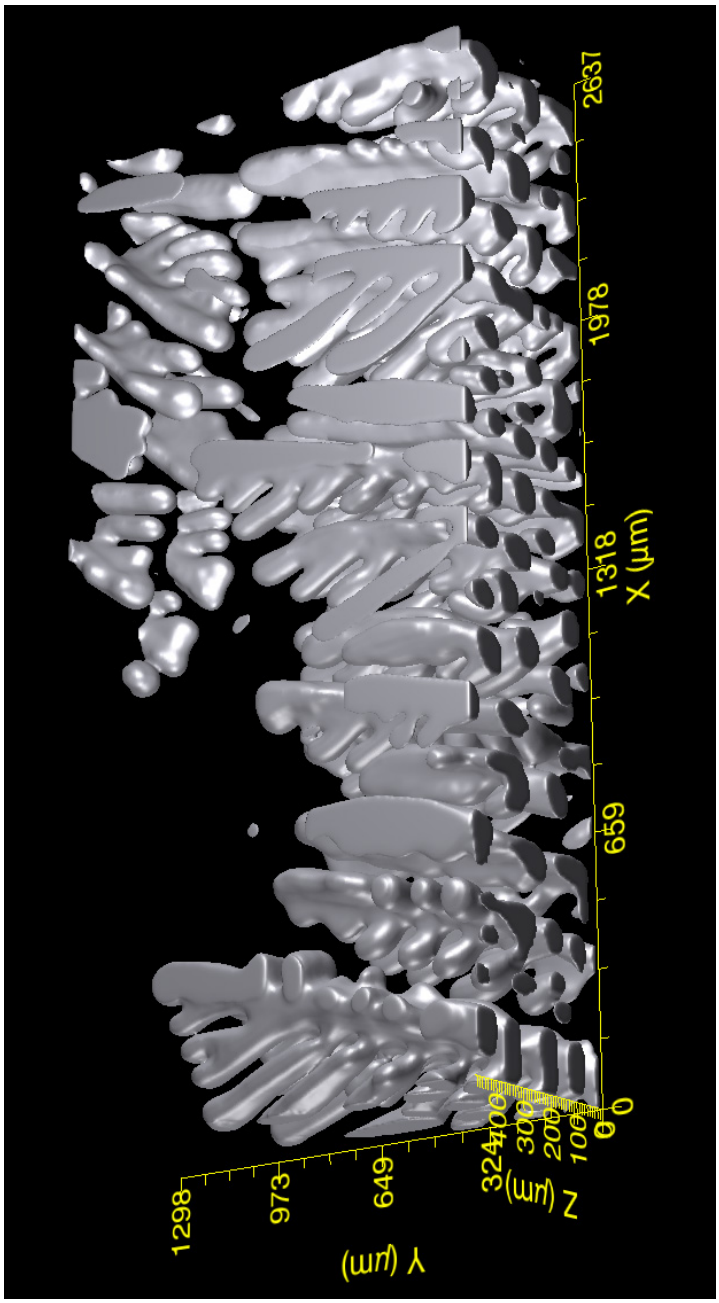

Figure 6.10. Three-dimensional reconstruction of the 100 minute coarsened sample, non-dense region.

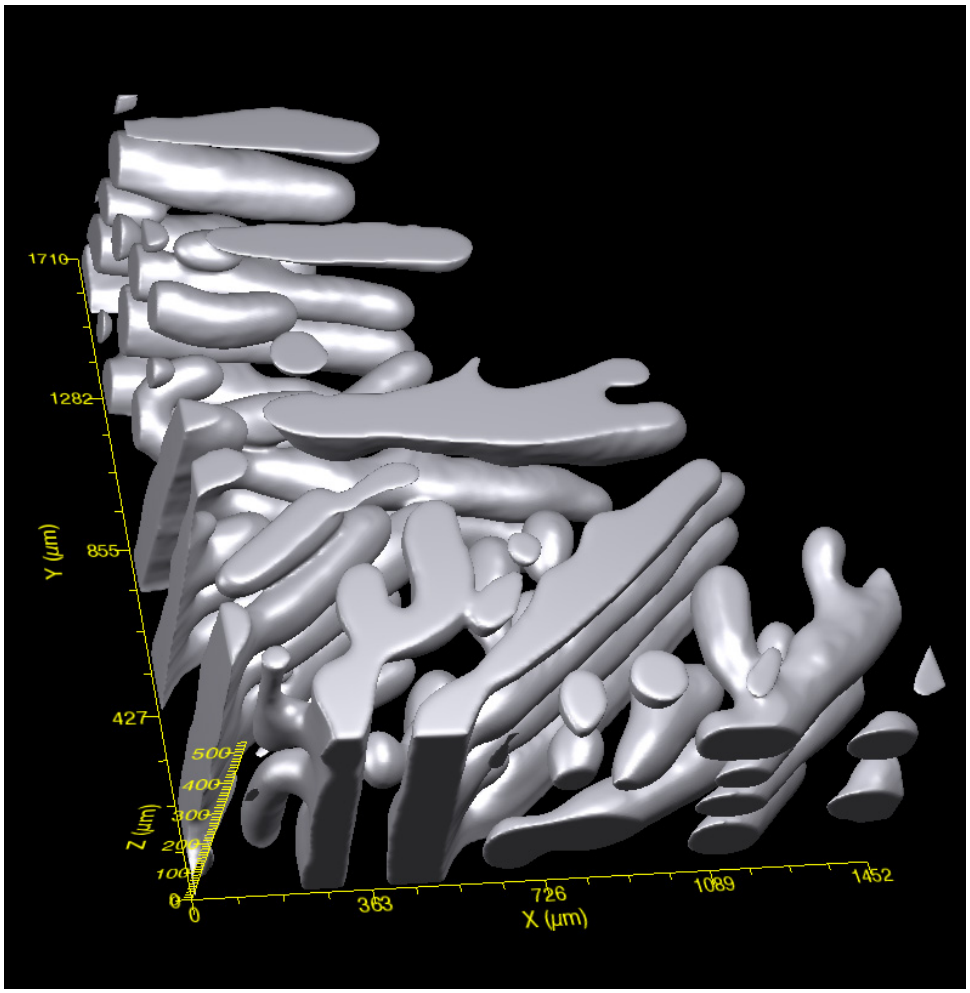

Figure 6.11. Three-dimensional reconstruction of the 846 minute coarsened sample, non-dense region.

6.3. Interface Shape Distributions

Unlike particle systems, where the interfacial curvature can be characterized by using a particle size distribution, characterization of curvature in complex structures such as dendrites requires a more elaborate method. The technique used for determining the so-called Interface Shape Distribution (ISD) of a structure, along with the ISDs for dense and non-dense regions of each sample, is described here.

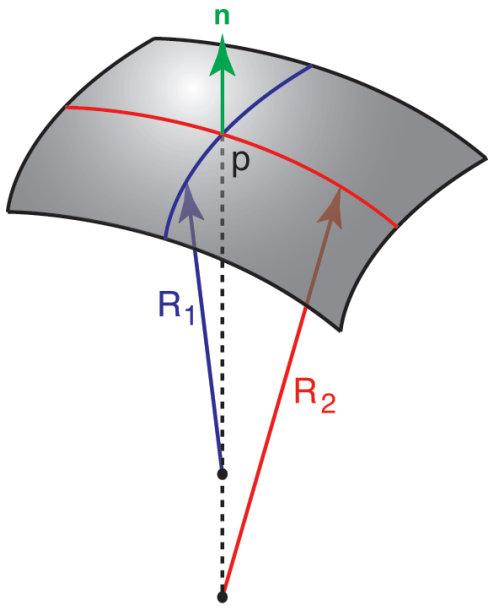

Figure 6.12. Definition of principal curvatures at a point on the surface. Note that the curvature is positive when the center of the radius is on one side of surface and negative when on the other.

6.3.1. Method

Once the three-dimensional mesh has been created and optimized, it can be used to calculate interfacial curvature at any point in the structure. For any patch of interface, the curvature at the center of the patch, point p, can be completely characterized by the two principal radii of curvature, R_1 and R_2 (see Figure 6.12). Each radius corresponds to an imaginary circle that is tangent to the surface patch at point p. The circles are perpendicular to each other and represent the maximum and minimum radii of curvature for the patch. The principal curvatures for the patch are defined simply as the inverse maximum and minimum radii of curvature,

$$\kappa_1 = \frac{1}{R_1} \tag{6.1}$$

$$\kappa_2 = \frac{1}{R_2} \tag{6.2}$$

In all cases, κ_1 is defined here to be greater than κ_2. An alternate method which can also be used to completely characterize the shape of a local interface is to measure the mean curvature, H, and the Gaussian curvature, K, defined as

$$H = \frac{1}{2}\left(\frac{1}{R_1} + \frac{1}{R_2}\right) = \frac{(\kappa_1 + \kappa_2)}{2} \tag{6.3}$$

$$K = \left(\frac{1}{R_1}\right)\left(\frac{1}{R_2}\right) = \kappa_1 * \kappa_2 \tag{6.4}$$

Unlike a spherical surface, which needs only one parameter (the radius) to be fully characterized, consideration of a saddle-shaped region illustrates why two values are necessary to completely describe the curvature of a non-spherical surface. In such a case it is possible that $R_1 = -R_2$ and so consequently $H = 0$. Using just one measure it is impossible to distinguish this surface from a planar surface, which also has a mean curvature value of $H = 0$. And while coarsening has long been described by the Gibbs-Thompson equation (Equation 2.1) which considers only mean curvature, Drew has shown that Gaussian curvature is also a determining factor during interface evolution [**49**].

Interfacial curvature can be determined using a variety of methods. Previous work in this group used the parallel surface method, described by Jinnai *et. al.* [**59**], however this work was done using a newer and faster method first described by Lavoué *et al.* [**60**]. This new method works by calculating Voronoi areas and using a mixed Finite-Element/Finite-Volume method. After triangulating the interface, the interior angles of the triangles

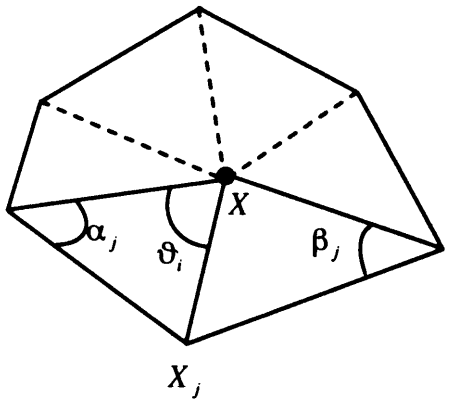

Figure 6.13. First ring of neighbors around vertex X used to calculate the curvature at point X.

surrounding each vertex are calculated as shown in Figure 6.13. The mean and Gaussian curvatures can then be calculated using the following equations where A is the Voronoi area:

$$H(X) = \frac{1}{2A}\sum(cot\alpha_j + cot\beta_j)(X_j - X) \tag{6.5}$$

$$K(X) = \frac{1}{A}(2\Pi - \sum \vartheta_i) \tag{6.6}$$

$$A = \frac{1}{8}\sum(cot\alpha_j + cot\beta_j)\|X_j - X\| \tag{6.7}$$

After the surface has been triangulated, the area of each surface patch is also calculated.

Once the curvatures have been calculated for all points on the interface, the curvature information can be displayed on a three dimensional plot like the one shown in Figure 6.14. $P(\kappa_1, \kappa_2)$ is a probability density function such that $P(\kappa_1\kappa_2)d\kappa_1 d\kappa_2$ is the probability that a randomly chosen interface point will have principal curvatures from κ_1 to $\kappa_1 + d\kappa_1$ and

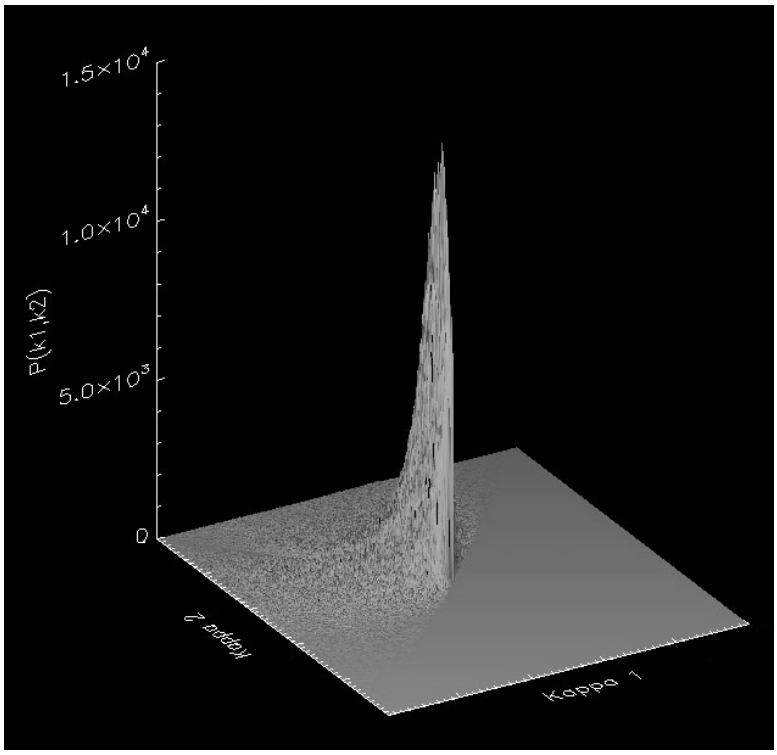

Figure 6.14. An example of the 3D curvature probability plot for κ_1 and κ_2.

from κ_2 to $\kappa_2 + d\kappa_2$. Although such a plot gives some idea of the curvature distribution, it is difficult to use for quantitative or comparison purposes. For this reason, these three-dimensional plots are converted to two-dimensional contour plots, substituting a color gradient for the z-dimension. These plots are particularly useful because each region of the plot is associated with a particular shape, as illustrated in Figure 6.15. A summary of the regions found on an ISD is given below. Note that there will never be data below the $\kappa_1 = \kappa_2$ line because κ_1 has been defined to be greater than κ_2. Self-similarity during coarsening can be explored by normalizing each plot by S_v, so that the graph shows κ_1/S_v versus κ_2/S_v. If the normalized ISD does not change with time, the structure is coarsening in a self-similar manner.

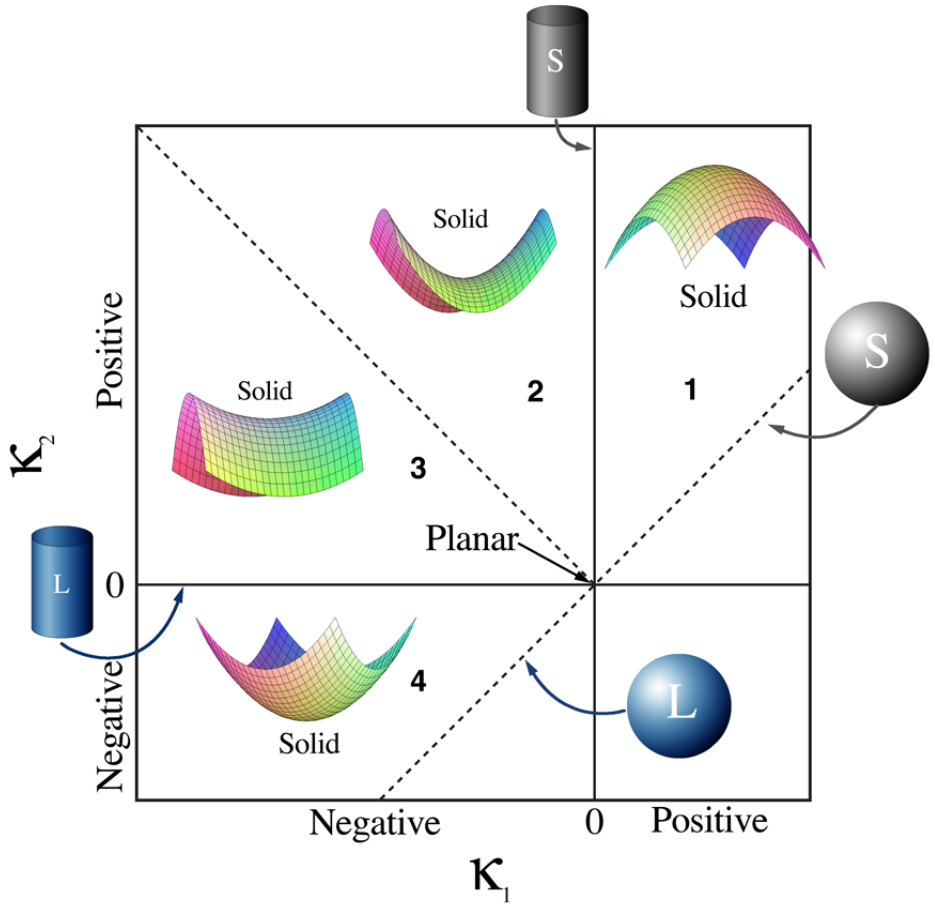

Figure 6.15. Map of local interfacial shapes for the $\kappa_1 - \kappa_2$ contour plots, known as Interface Shape Distributions (ISDs).

- Interfaces with curvatures that lie on the $\kappa_1 = \kappa_2$ line are spherical:
  - the interface has a spherical shape, composed of solid, if $\kappa_1 = \kappa_2 > 0$
  - the interface has a spherical shape, composed of liquid, if $\kappa_1 = \kappa_2 < 0$
- Interfaces with cylindrical shapes
  - are solid cylinders, if $\kappa_1 = 0$
  - are liquid cylinders, if $\kappa_2 = 0$
- Interfaces with $\kappa_1 < 0$ and $\kappa_2 > 0$ are saddle-shaped

- Interfaces with $\kappa_1 > 0$ and $\kappa_2 > 0$ are defined as convex towards the solid
- Interfaces with $\kappa_2 < 0$ are defined as concave towards the solid
- Interfaces with $\kappa_1 = \kappa_2 = 0$ are planar
- Interfaces in region 1 of the map have $H > 0$ and $K > 0$
- Interfaces in region 2 of the map have $H > 0$ and $K < 0$
- Interfaces in region 3 of the map have $H < 0$ and $K > 0$
- Interfaces in region 4 of the map have $H < 0$ and $K < 0$

6.3.2. ISDs of Dense Regions

The interface shape distributions for the dense regions of all four samples are shown unscaled in Figure 6.16 and scaled for comparison in Figure 6.17. The unscaled ISDs clearly depict the increase in length scale of the system with coarsening time, as the non-zero probability region of the plots shrinks towards the origin. This is logical, since the axis of the plots are κ_1 and κ_2 which have units of inverse microns; therefore, as the structure gets larger, the average principal curvatures will get smaller.

The scaled ISDs allow for comparison of the structures without regard to length scale; that is, to look at changes that are taking place besides the increase in scale. As discussed in Chapter 2 and illustrated in Figure 6.1, S_v^{-1} increases as $t^{1/3}$ with coarsening time and so makes an excellent measure by which to scale the ISDs. To accurately compare the ISDs, the color bar also needs to be the same. The maximum value for the color bar was set to the value of the highest peak in any plot, which in this case was 0.416 and corresponds to a peak in the 20 minute coarsened sample.

By observing the shape of the ISD and the evolution of the peak position with coarsening time, one can detect the dominant interfacial shapes and verify quantitatively the observations made by looking at the three-dimensional reconstructions. For each sample here, the majority of curvature is distributed along the $\kappa_1 = 0$ solid cylinder line, corresponding to stalks and arms of the dendrites, which are roughly cylindrical but have a range of diameters. The peak region also extends to the right of this line, into the convex towards the solid area. This region corresponds to the hemispherical caps on the ends of the dendrite arms. With increased coarsening time, the magnitude of the peak along the solid cylinder line first increases in intensity, then decreases while the peak contracts upwards toward a single value centered at about κ/S_v=1.6.

These four samples represent an increase in length scale of the structure of more than two times. When observed together, the four ISDs shown in Figure 6.17 are not dramatically different, especially when compared with the very large changes which are observed in samples coarsened for much longer times [**14**, **58**]. In directionally solidified Pb-Sn samples with a higher volume fraction, it was found that the structure evolves into long cylindrical tubes aligned along the primary growth direction at very long coarsening times. The lower volume fraction of solid of this sample precludes these long coarsening times because of the increased effects of sedimentation, and at the four coarsening times presented here, the transition to vertically aligned cylinders is just beginning.

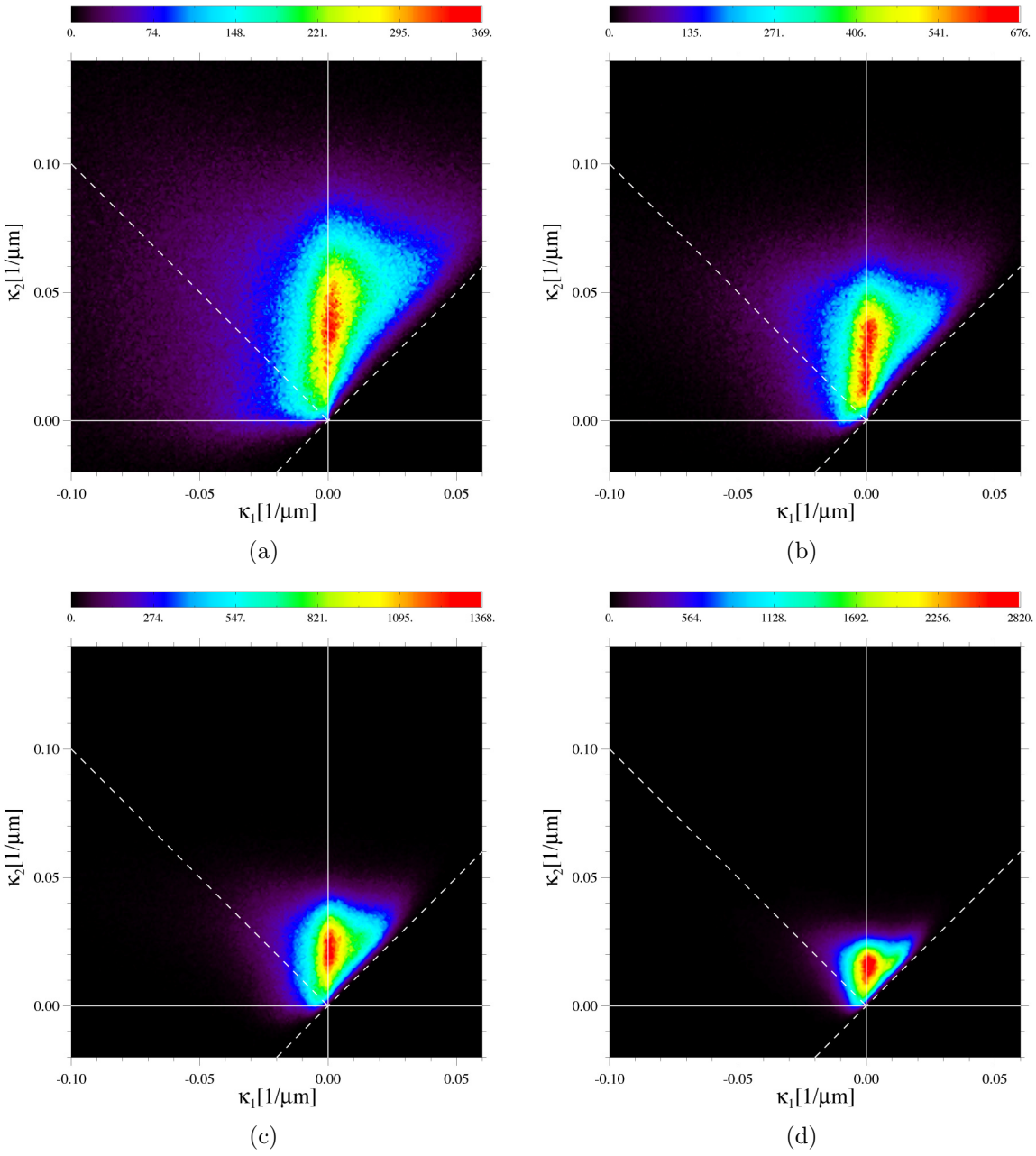

Figure 6.16. Unscaled ISDs for dense region of (a) 3 min (b) 28 min (c) 100 min (d) 846 min sample. In each plot, the maximum value of the colorbar corresponds to the maximum peak value of that plot.

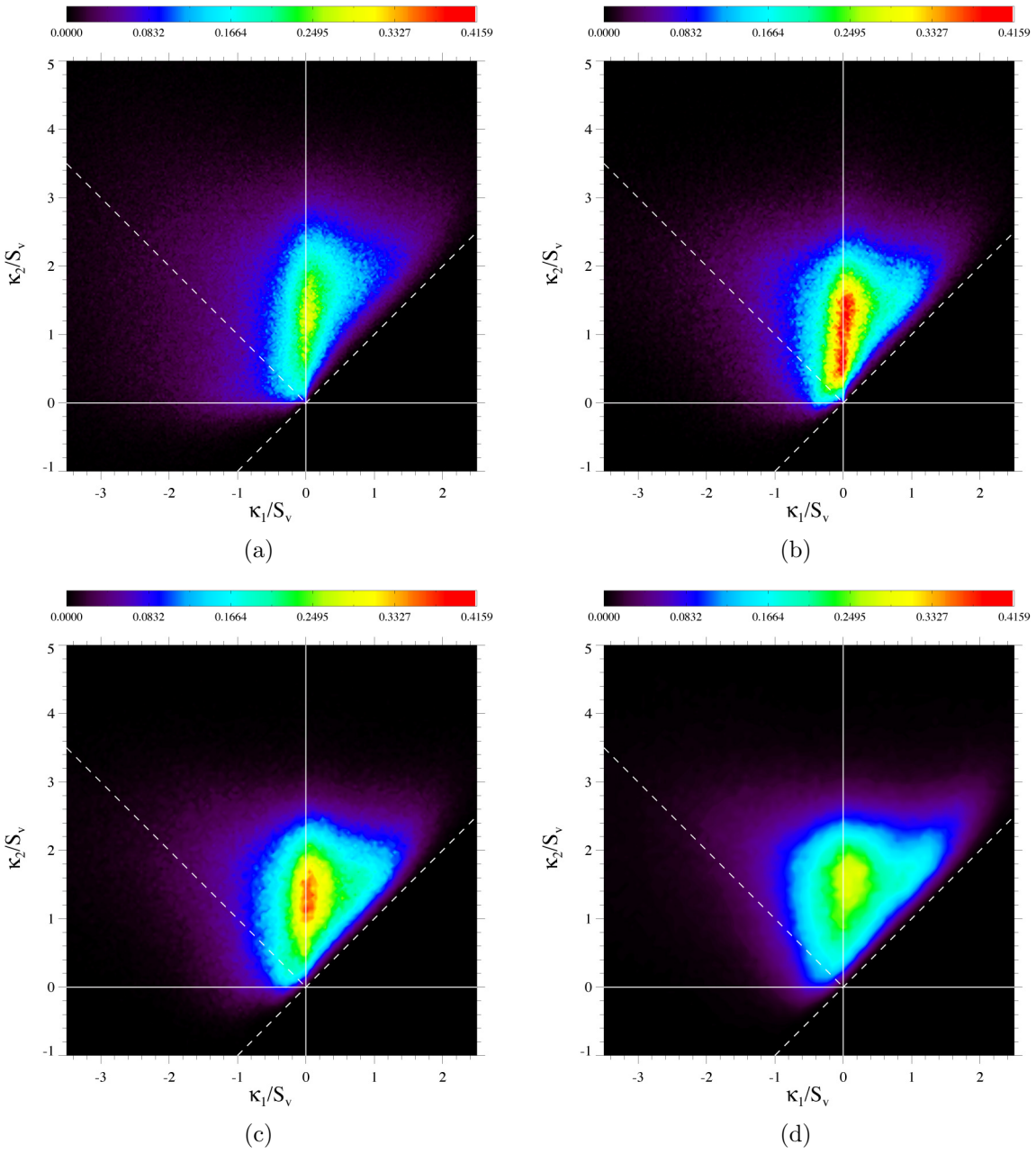

Figure 6.17. Scaled ISDs for dense region of (a) 3 min (b) 28 min (c) 100 min (d) 846 min sample. In each plot the colorbar has the same scale.

6.3.3. ISDs of Non-dense Regions

The interface shape distributions for the non-dense regions of all four samples are shown unscaled in Figure 6.18 and scaled for comparison in Figure 6.19. The most noticeable feature of all four plots is that the curvature is very strongly aligned along the solid cylinder line. This is reasonable, as the 3D images show that these regions consist of secondary arms growing uninhibited into the free space. At all times, there is less probability to the left of the solid cylinder line (high Gaussian curvature) then there was for the dense regions. This area of probability corresponds to the saddle-shaped regions which occur at the base of each dendrite arm. In the ISDs of the non-dense regions, the amount of saddle-shaped interface also decreases with coarsening time, a sign that the number of tertiary arms is decreasing. The region to the right of the peak area, corresponding to the hemispherical caps at the end of each dendrite arm, changes very little with coarsening time.

After 3 minutes of coarsening time, there are second, third and fourth-order arms present which have a variety of diameters and cause the peak of the ISD to be the most diffuse of the four. By 28 minutes, the fourth-order arms have disappeared and the peak has consolidated onto the solid cylinder line, as the structure is now primarily composed of near-cylindrical third-order arms arranged on near-cylindrical second-order arms. As in the ISD from the dense region, the red region of the peak is spread over a variety of κ_2 values, centered around $\kappa_2/S_v = 2$, indicating that there exist cylinders with a range of radii and an average radii of about S_v^{-1}. In the last two coarsening times, the peak value contracts upward as the arms continue to disappear due to coarsening and become relatively smaller compared to the scale of the structure. The ISD in Figure 6.19d

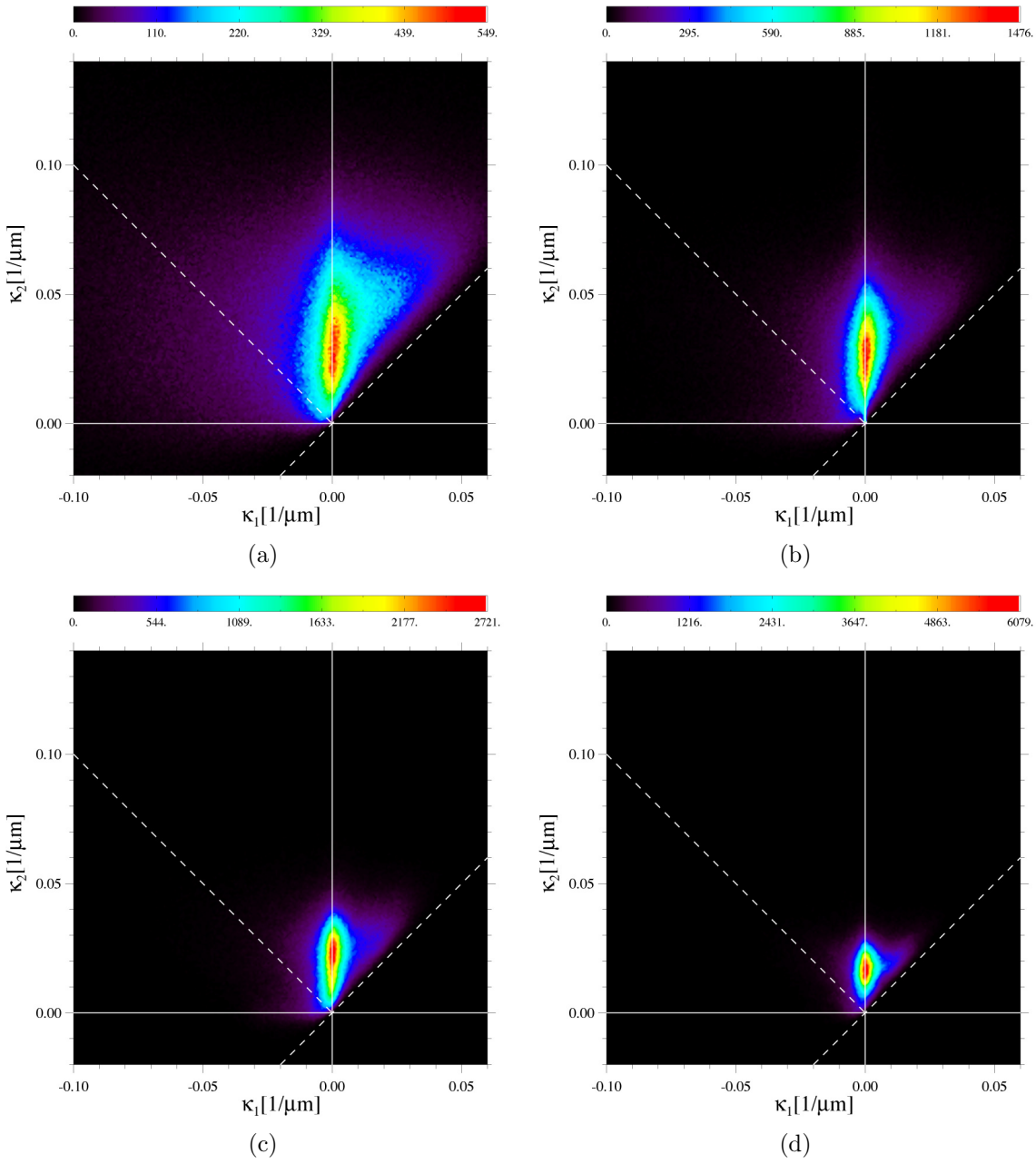

Figure 6.18. Unscaled ISDs for non-dense region of (a) 3 min (b) 28 min (c) 100 min (d) 846 min coarsened sample. In each plot, the maximum value of the colorbar corresponds to the maximum peak value of that plot.

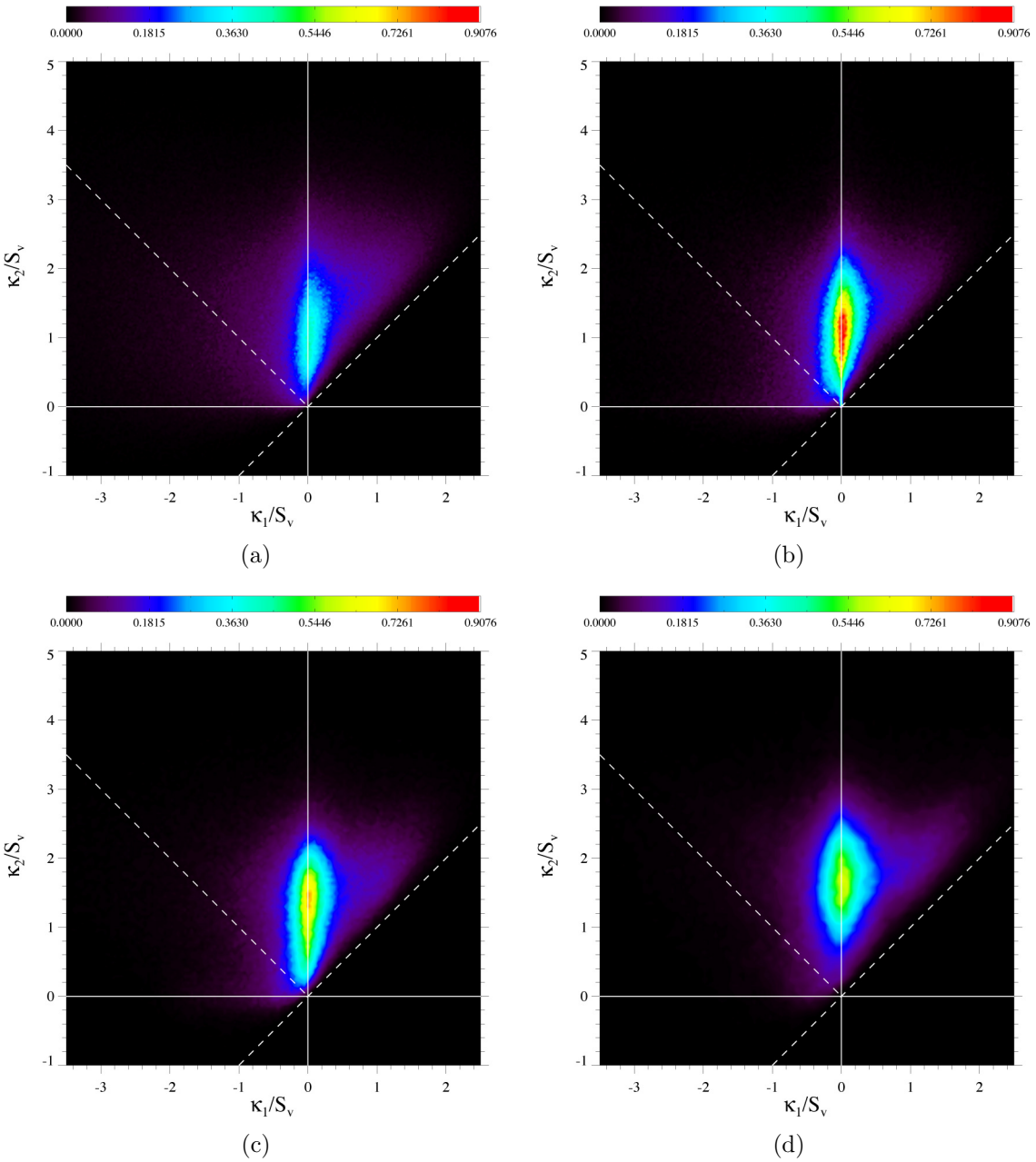

Figure 6.19. Scaled ISDs for non-dense region of (a) 3 min (b) 28 min (c) 100 min (d) 846 min coarsened sample. In each plot the colorbar has the same scale.

indicates that by 486 minutes all secondary dendrite arms have obtained a fairly uniform radius of about $1.6S_v^{-1}$. Note that while these secondary arms are still clearly present and distinct after 486 minutes of coarsening time, in the dense dendritic regions (Figure 6.7) the secondary arms are nearly gone by this time.

6.3.4. Correlating ISDs and 3D Reconstructions

When comparing the ISDs to the three-dimensional reconstructions, it is possible to correlate regions of the ISD to the exact patches of interface which appear in that region. For example, Figure 6.20 shows that the convex toward the solid region (region 1 in Figure 6.15) does in fact correspond to the tips of the dendrite arms. This approach was used to determine that the range of values along the solid cylinder line in Figure 6.19b are not due so much to dendrite arms of different radii as to varying radii within the same arm. In this sample, the arms are not true cylinders but long rods with a roughly elliptical cross section. Because of space constraints, secondary arms are flattened on the top and bottom with higher curvatures on the side (see Figure 6.21). As the primary dendrite stalks grow in the z direction, they send out secondary arms in the x-y plane. The spacing between primary stalks is greater than the spacing between consecutive arms in the z-direction, so the secondary arms generally branch only in the x-y plane, where there is more room for the tertiary arms to develop. Thus, as Figure 6.22 shows, the dendrite arms form flat, fan-like clusters, which contain individual arms that are also flattened in the x-y plane. Because the groups of tertiary arms grow quite close together, they are sometimes distorted in the opposite way, with larger curvatures on the sides and smaller curvatures found on the top and bottom. This effect can also be seen in Figure 6.21. The tertiary

arms grow at an angle which is approximately 42° from the main arm. With increased coarsening time, the ISDs show that the remaining arms do become progressively more cylindrical.

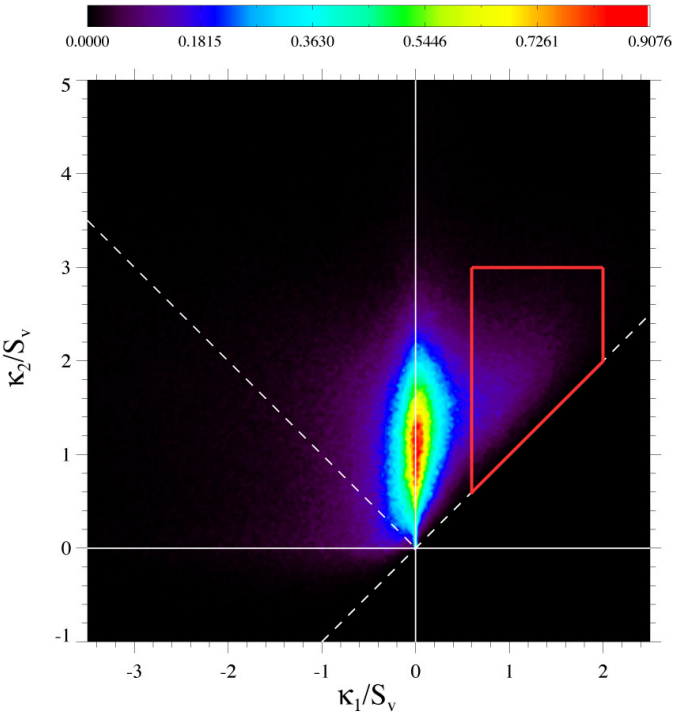

(a)

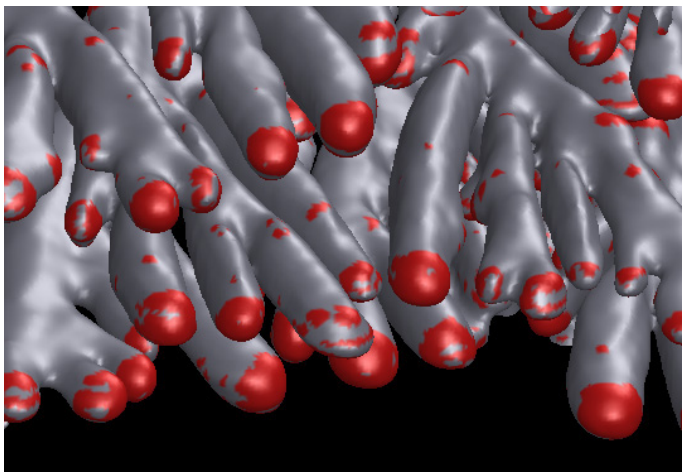

(b)

Figure 6.20. (a) The ISD for the non-dense region of the 28 minute coarsened sample, with the convex toward solid region selected. (b) A small region of the non-dense 28 minute coarsened sample, with all curvature inside the selected region highlighted in red. It is clear that the probability in this region of the ISD corresponds to the tips of the dendrite arms.

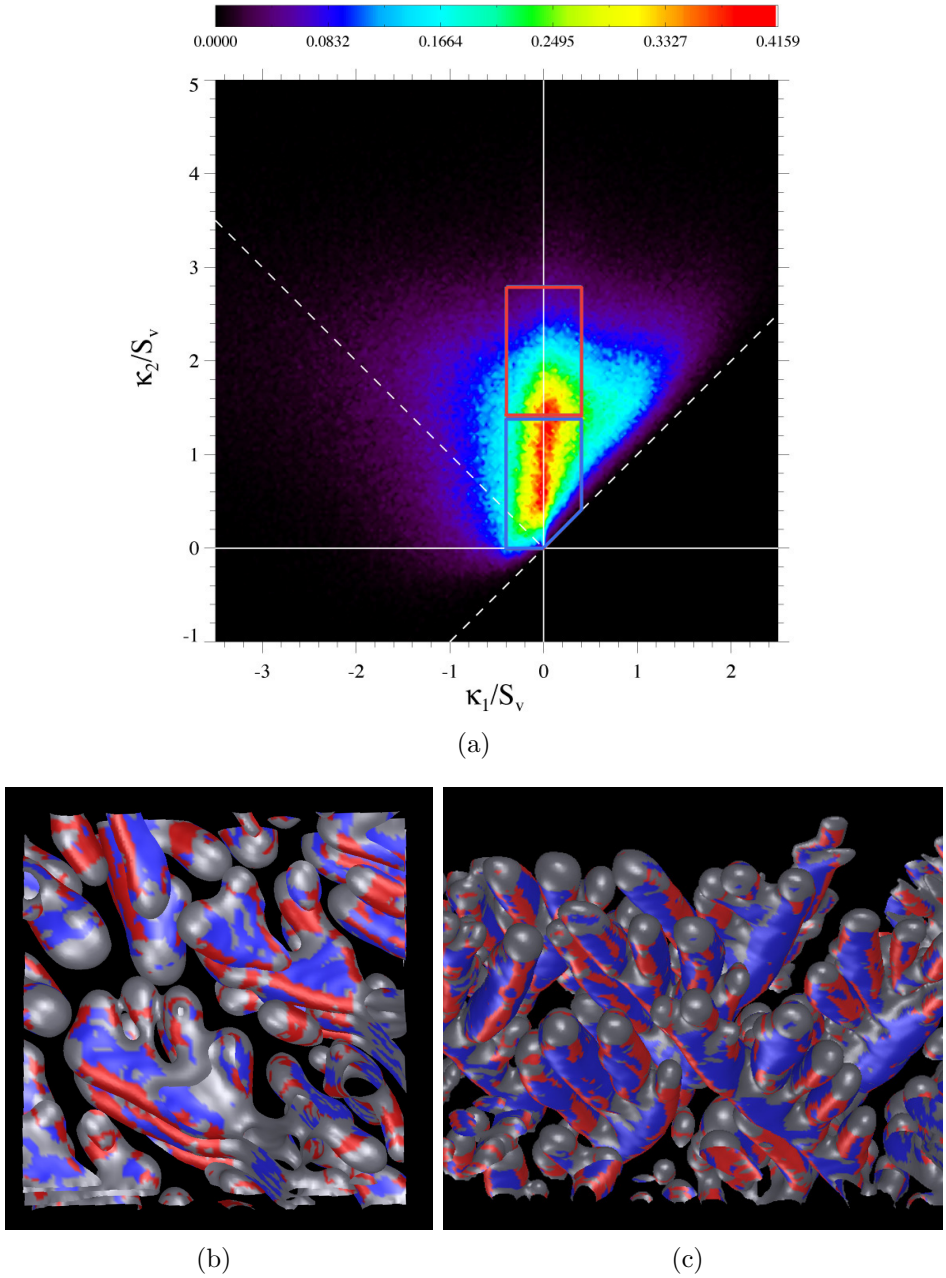

Figure 6.21. (a) The ISD for the dense regions of the 28 minute coarsened sample, with two regions selected along the solid cylinder line. (b) A small region of the 28 minute coarsened dense sample, with the upper selected region (red box) highlighted in red and the lower selected region (blue box) highlighted in blue; viewed directly down the z-axis. (c) A segment of the 28 minute coarsened non-dense structure, with the same curvature regions highlighted; viewed up the z-axis.

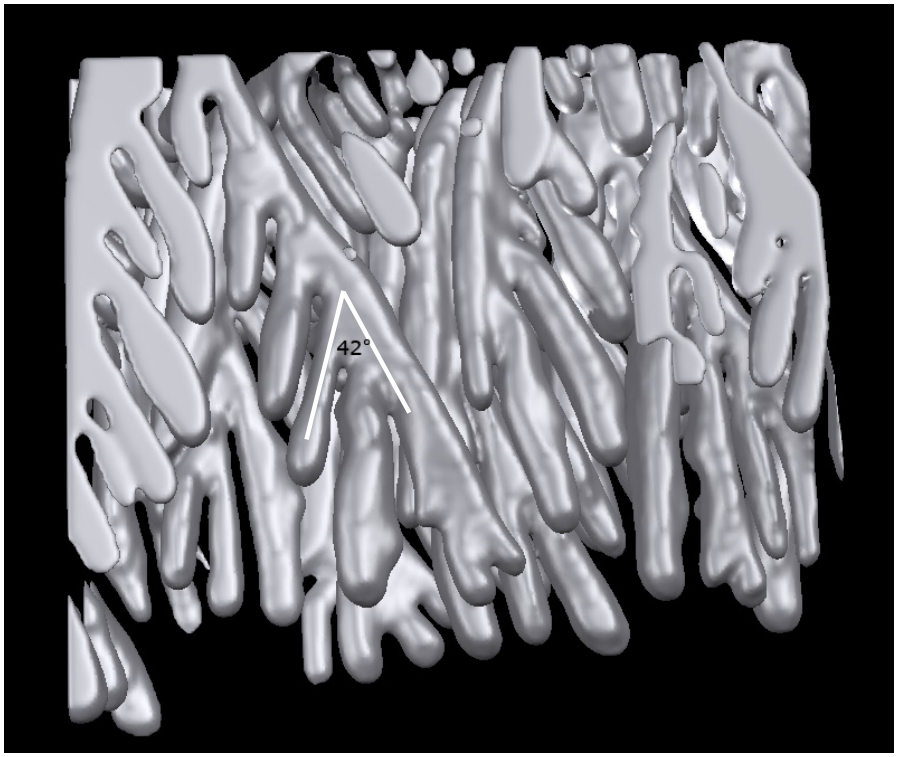

(a)

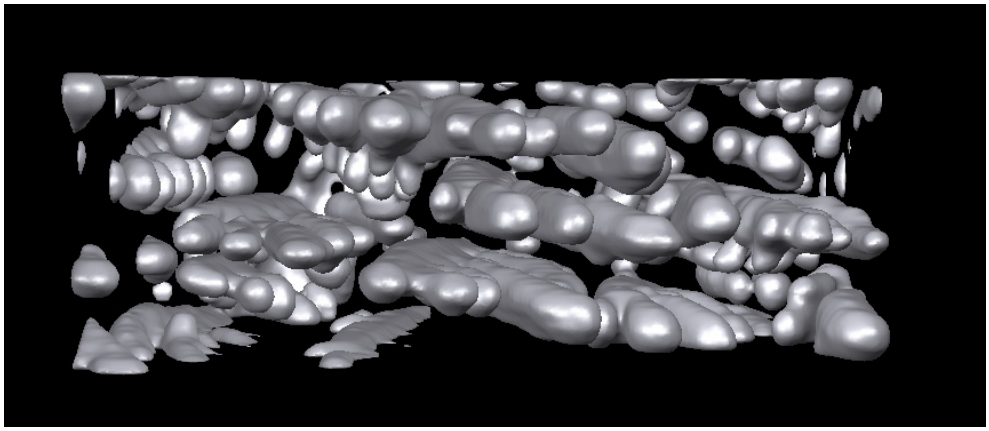

(b)

Figure 6.22. A section of the non-dense 28 minute coarsened sample showing the growth formations of the dendrite arms into the liquid. (a) Looking down the z-axis, so the 42° angle formed by the secondary and tertiary arms is apparent. (b) Looking along the y-axis, so that the spacing between the arms is visible.

6.4. Interface Normal Distributions

Because it is often useful to understand and track the directionality of a structure, a method of analyzing preferential directionality to produce Interface Normal Distributions (INDs) was previously developed [**14**]. The technique for obtaining these probability plots, along with the INDs for the dense and non-dense region of each sample, is presented here.

6.4.1. Method

For any structure where the curvature has been determined for every patch of interface, all the interface normals can be collapsed into a unit reference sphere, with their origins at the center of the sphere and their ends on its surface. A spherical projection is then used to obtain a two-dimensional representation of the directionality of the interfaces. For this work, an equal-area projection, see Figure 6.23, taken along the x-axis is used. The projection plane is tangent to the sphere and perpendicular to the axis along which the projection is made. As Figure 6.23 illustrates, the projection is obtained by drawing an arc from a point on the reference sphere to the projection plane such that the distance from the tangency point (B) to the projected point is equal to the distance from the tangency point to the point on the reference sphere. This allows for minimal distortion of features near the center of the plots, which is where the data from these samples is primarily concentrated. Also to minimize distortion, the data is binned in three dimensions on the reference sphere, with each bin covering the same amount of surface area on the sphere, instead of binning afterwards on the projection. Since the structures being analyzed are not symmetric, two projections are needed to represent all data: a near-hemisphere

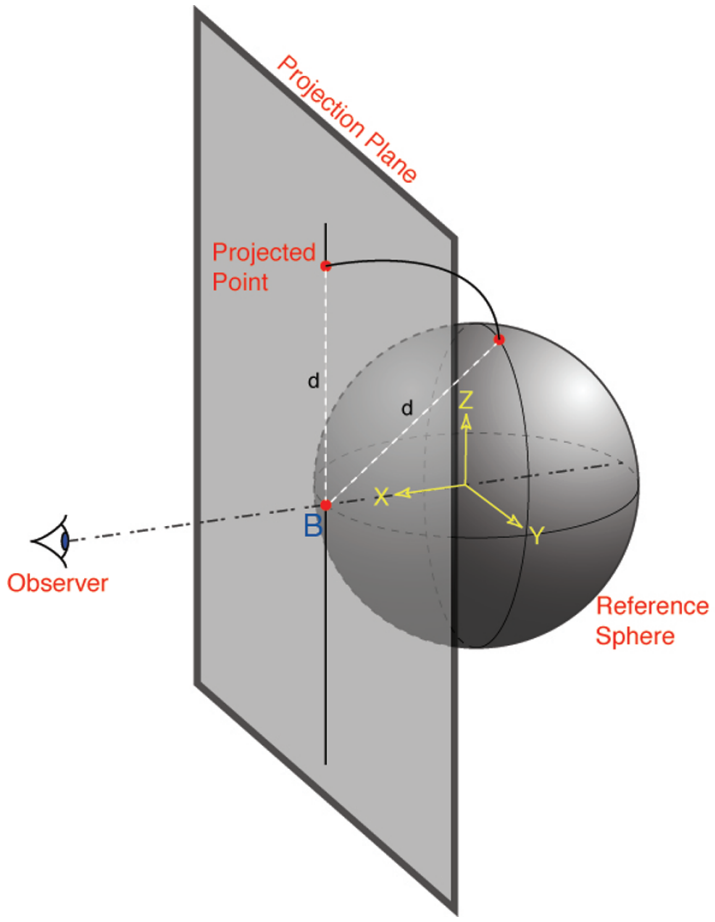

Figure 6.23. Schematic representation of the equal-area projection used to obtain the INDs.

projection (projected along the positive x-axis) and a far-hemisphere projection (projected along the negative x-axis).

During the course of this work, a method was developed to display the binned orientation data directly on the surface of the reference sphere which could be manipulated on the screen by a user. This has the potential to be a useful tool for understanding interfacial orientation distributions because it avoids the distortion caused by projections and also the general confusion often present when thinking about a two-dimensional plot

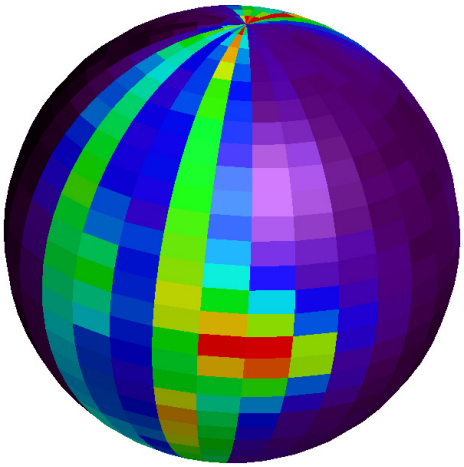

Figure 6.24. Screen capture of a sphere showing the distribution of interface normals on its surface. This sphere shows the distribution of normals for the nondense region of the 486 minute coarsened sample.

representing a three-dimensional surface. An image of the sphere is shown in Figure 6.24. The sphere shown is displaying the orientation of interface in the nondense 486 minute coarsened sample (compare to the projected version of this data in Figure 6.33. This sphere can be freely rotated by the user to view the color distribution from all angles, or captured as a movie while rotating about an axis. Such a construction is most useful for explanations and presentations where the sphere can be rotated before the audience.

6.4.2. INDs of Dense Regions

The INDs for the dense region of each sample are shown in Figures 6.25-6.28. By convention, an open circle at the origin of the coordinate system indicates that the positive axis is coming out of the page and the symbol $\otimes$ indicates that the positive axis is going into the page. To facilitate comparison between samples, the interface normals were rotated

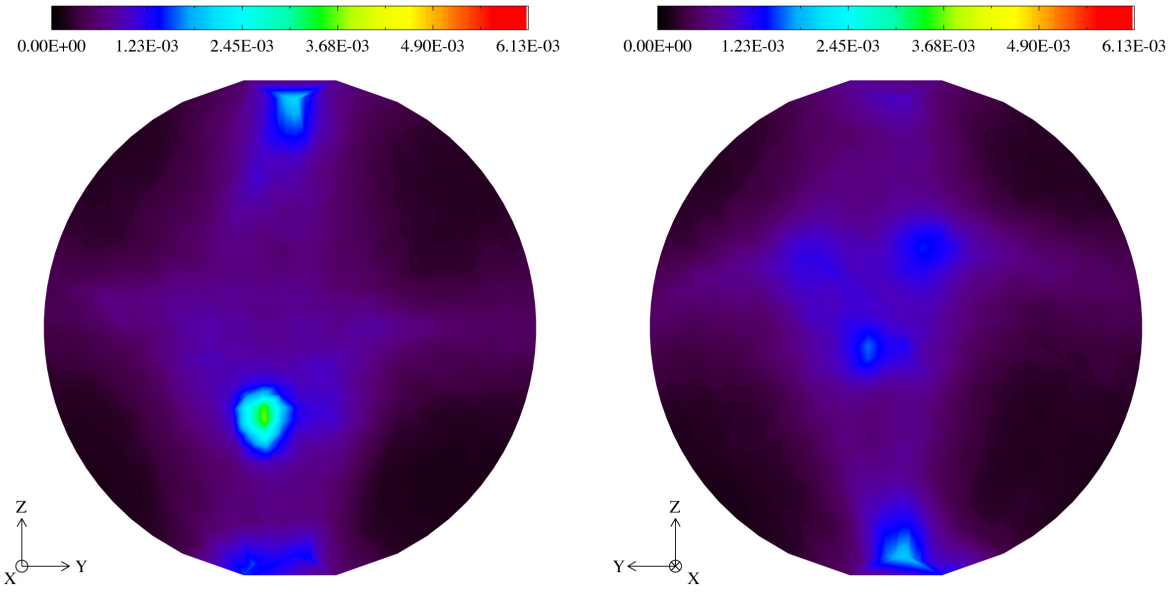

Figure 6.25. IND for the dense region of the 3 min coarsened sample.

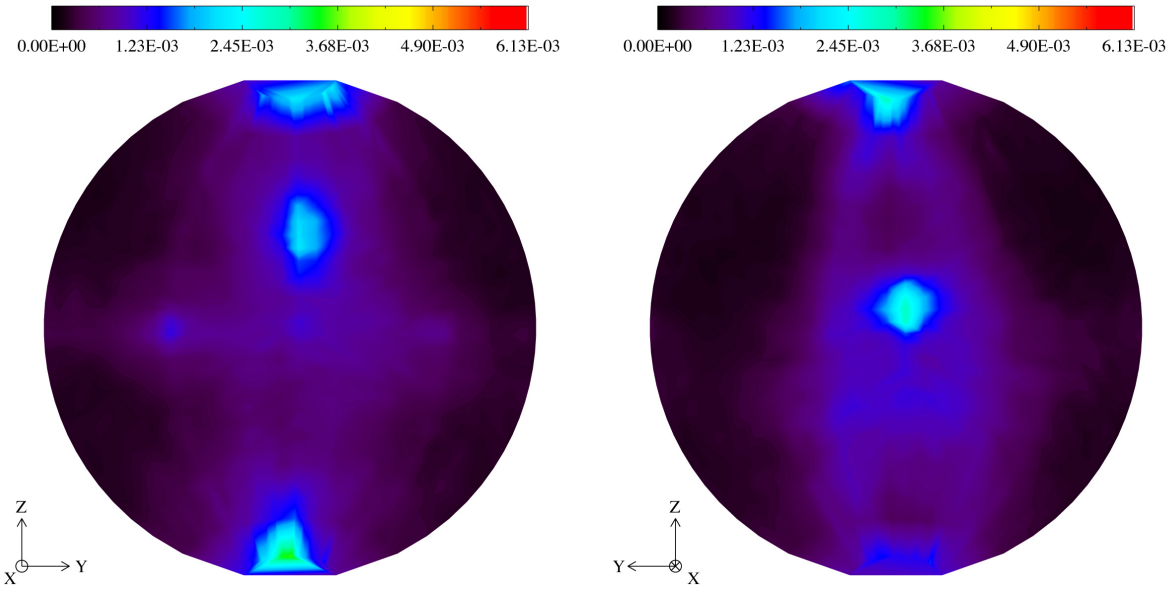

Figure 6.26. IND for the dense region of the 28 min coarsened sample.

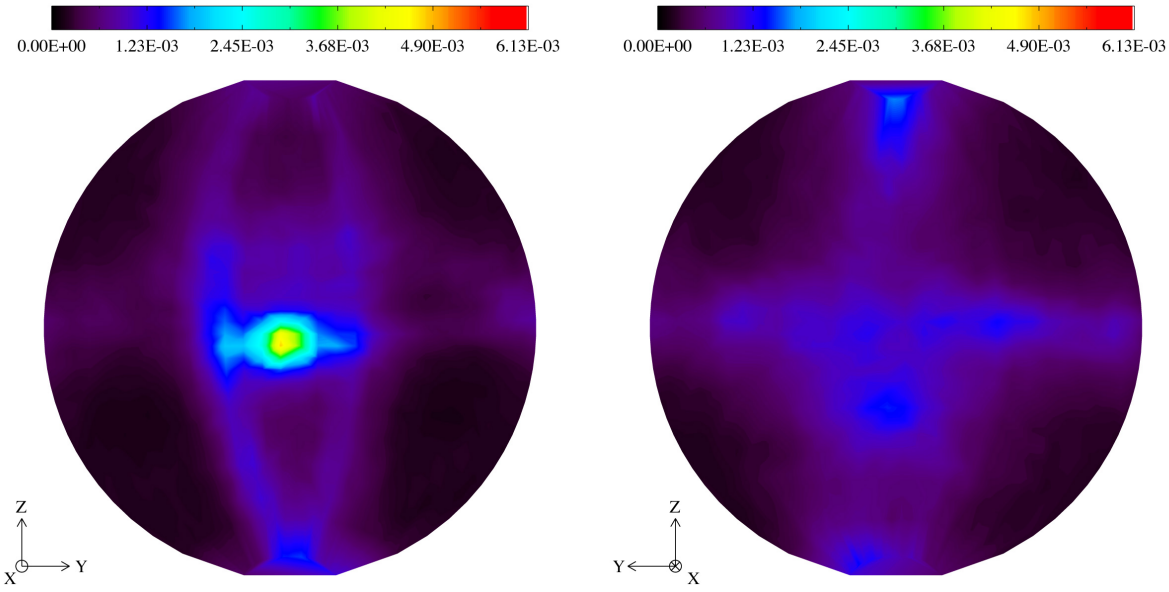

Figure 6.27. IND for the dense region of the 100 min coarsened sample.

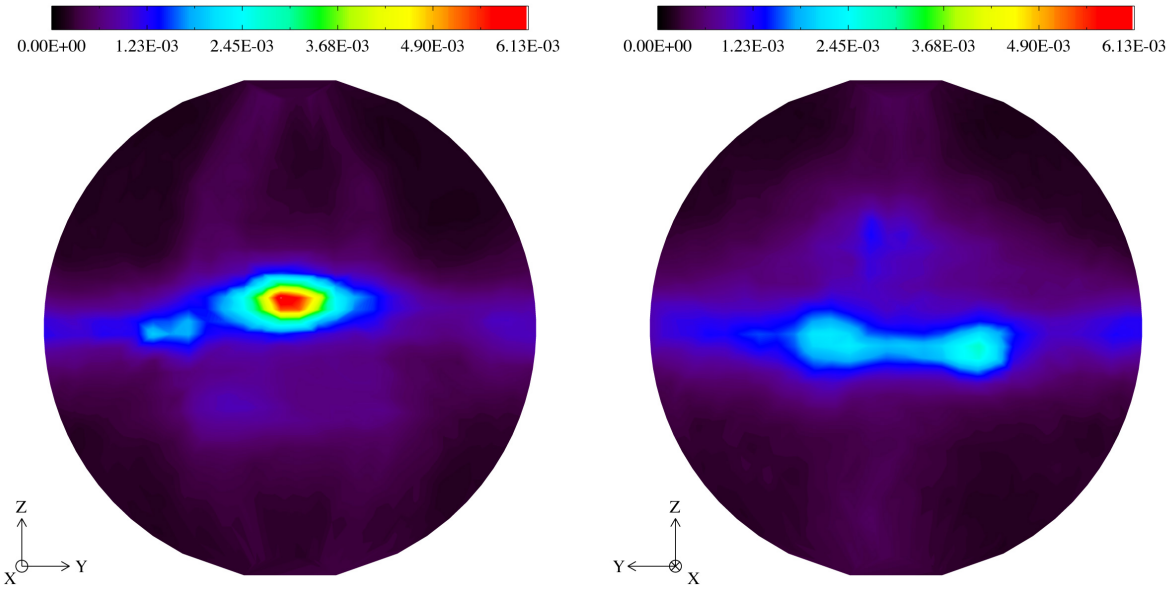

Figure 6.28. IND for the dense region of the 486 min coarsened sample.

in the x-y plane so as to center the primary peak in the middle of each plot. This corresponds to a rigid body rotation of the microstructure and does not effect the results in any other way. The colorbar in all four figures has the same scale to facilitate comparison. As with the ISDs, the maximum value of the colorbar is set to the maximum peak value in all plots.

When comparing the INDs for the four coarsening times, it is clear that there is an increase in directionality with coarsening, as the peak value in each plot gets progressively higher. At each time, there is a primary peak near the center of each plot. Since these are projections along the x-axis, a peak at this position indicates that the normals are parallel to the x-direction, hence the interface itself is parallel to z. This corresponds to the primary dendrite stalks which become more prominent with time as the dendrite arms disappear.

The primary stalks do not, however, become cylinders in this time period, as a perfect cylinder running in the z-direction would appear on these projections as a horizontal line of equal intensity through the center of the plot. While there is a horizontal line at later times, most of the probability is concentrated into one or two peaks along that line. This indicates that the primary stalks have some directionality in the x-y plane as well. Figure 6.33 shows that there is one strong peak in the near-hemisphere projection and two weaker symmetric peaks in the far-hemisphere projection for the 486 minute coarsened dense sample. Similar instances of the single peak/dual peaks has also been observed in this system with higher volume fraction alloys [**56**]. It can be attributed to the roughly triangular shape of the primary dendrite stalks. This shape is visible in Figure 6.29. As the figure shows, and is more clear in Figure 5.8, the primary dendrites grow closely

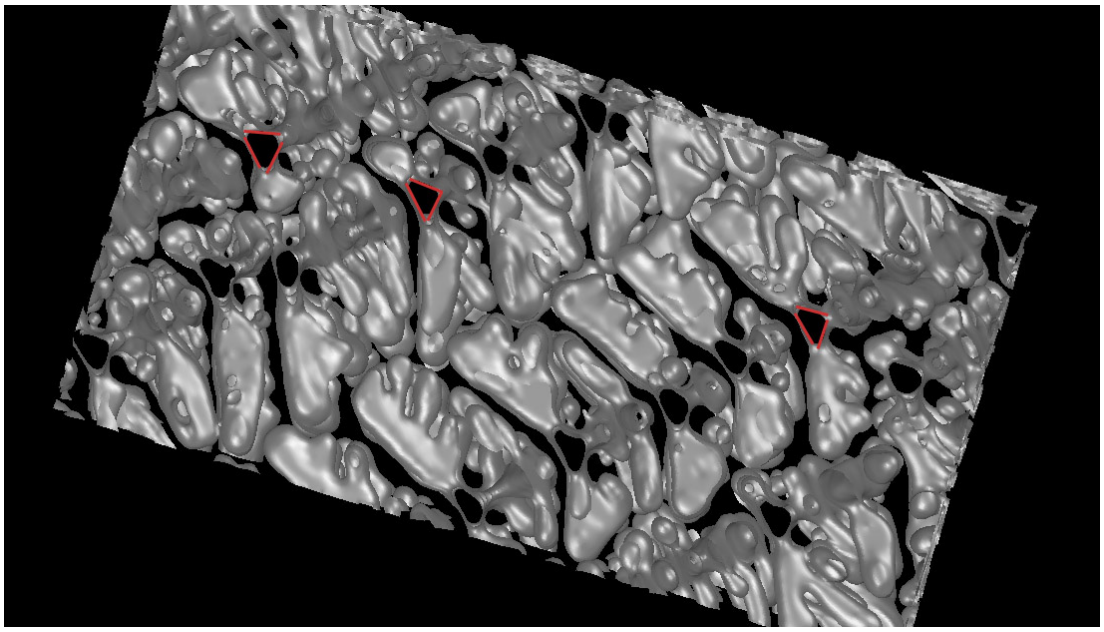

Figure 6.29. The dense 28 minute coarsened sample, where the three-sided nature of the primary stalks is clear. Several instances are marked in red.

spaced in parallel sheets. This is a phenomenon that has been observed for some time in tin dendrites [**61**]. It means that the secondary arms have the most room to grow in a direction perpendicular to the plane of the sheet. A smaller set of secondary arms also form in the plane of the primary sheet, but only on one side of each stalk. Thus, the triangular shape is a result of these three sets of secondary arms, and the peak seen in the INDs indicates the alignment of the primary sheet. When this morphology was discussed previously in higher volume fractions of this alloy, it was noted that the shape persists with coarsening for an extended time [**14**] before evolving to cylindrical tubes. This persistence was attributed to the relatively lower mean curvature of the stem which therefore coarsens at the expense of the surrounding regions.

While there are primary peaks in each of the four sets of INDs, there is also a region or regions of low-level (blue or purple) probability spread over a larger area. At the shortest

coarsening time, Figure 6.25, there are diffuse purple lines which run both vertically and horizontally across the plot. After 28 minutes of coarsening, Figure 6.26, there is only a vertical purple line. After 100 minutes, Figure 6.27, the horizontal line returns and comes to dominate the background probability by 486 minutes, Figure 6.28. Because these are projections taken along the z-axis, the vertical line comes from solid cylinders aligned along the y-direction, while the horizontal line is the result of solid cylinders aligned along the z-direction. This confirms what was discussed earlier in Section 6.3, that the structure is initially a complex combination of second, third and fourth-order arms aligned in all three primary planes. With increased coarsening, the higher-order arms disappear, leaving the structure to be dominated by second and third-order arms aligned in the x-y plane (thus the vertical purple stripe). In the later two coarsening times, the INDs show the vertical line fade away as the arms coarsen, leaving the vertically-aligned primary stalks and consequently a horizontal line across the IND plots. Thus, while the ISDs for the dense regions of the samples do not show much change over this range of coarsening times, when studied in conjunction with the three-dimensional reconstructions and the INDs, we see that it is different pieces of the morphology which are contributing to the similar shapes observed in the plots.

6.4.3. INDs of Non-dense Regions

The INDs for the non-dense region of each sample are shown in Figures 6.30-6.33. The plots are dominated by a pair of vertical stripes at each coarsening time except the first, where there is only one stripe of probability in each hemisphere. At 28 and 100 minutes of coarsening time, this dual stripe is attributed to the clusters of secondary and tertiary branches which grow generally in the x-y plane with a fixed angle between them (see Figure 6.22a). Thus, one stripe comes from the secondary arms and the other from the tertiary arms. At 3 minutes of coarsening time, the IND is very diffuse because of the many higher-order branches, and the single stripe probably corresponds to the direction in which most of the large secondary arms are growing. At 486 minutes of coarsening time, the tertiary arms are nearly gone, so the dual stripe must be attributable to something else. Examination of the sample from which these plots were constructed (shown in Figure 6.11) reveals that the region captured by the reconstruction contains secondary dendrite arms from two different sheets of primary dendrite stalks, and the angle formed by these sheets is comparable to the angle formed by secondary and tertiary arms. Thus the IND looks similar to previous coarsening times, but for a different reason. The angle between the two sheets in Figure 6.11, as well as many of the angles between sheets in Figure 5.8, is similar to the angles measured between dendrite arms, indicating that these sheets may originate from branching arms growing off a single primary stalk.

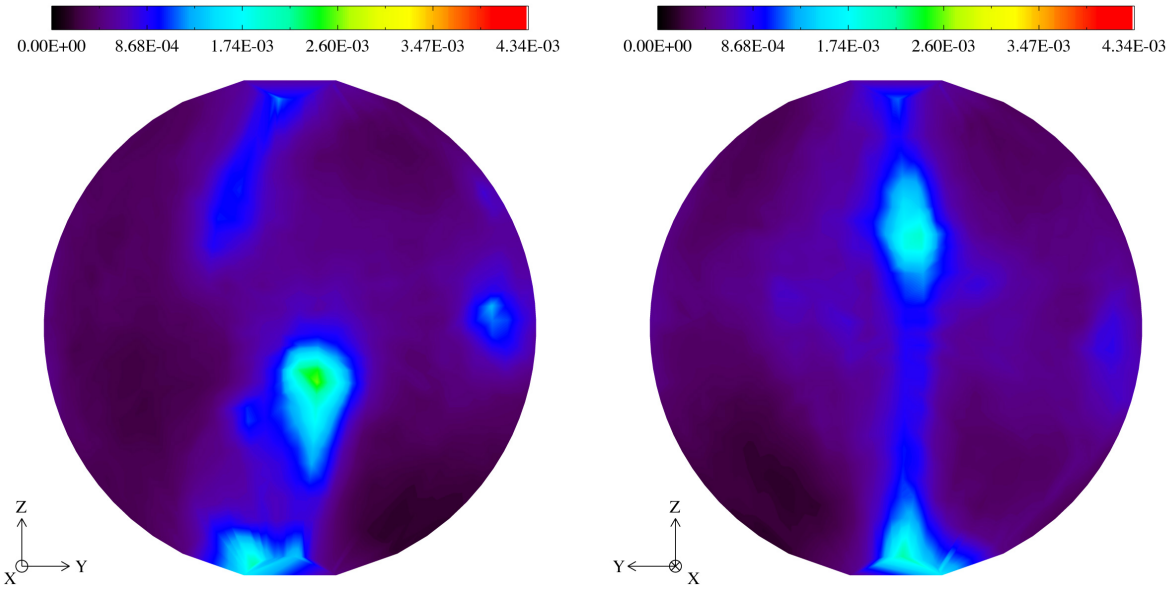

Figure 6.30. IND for the non-dense region of the 3 min sample.

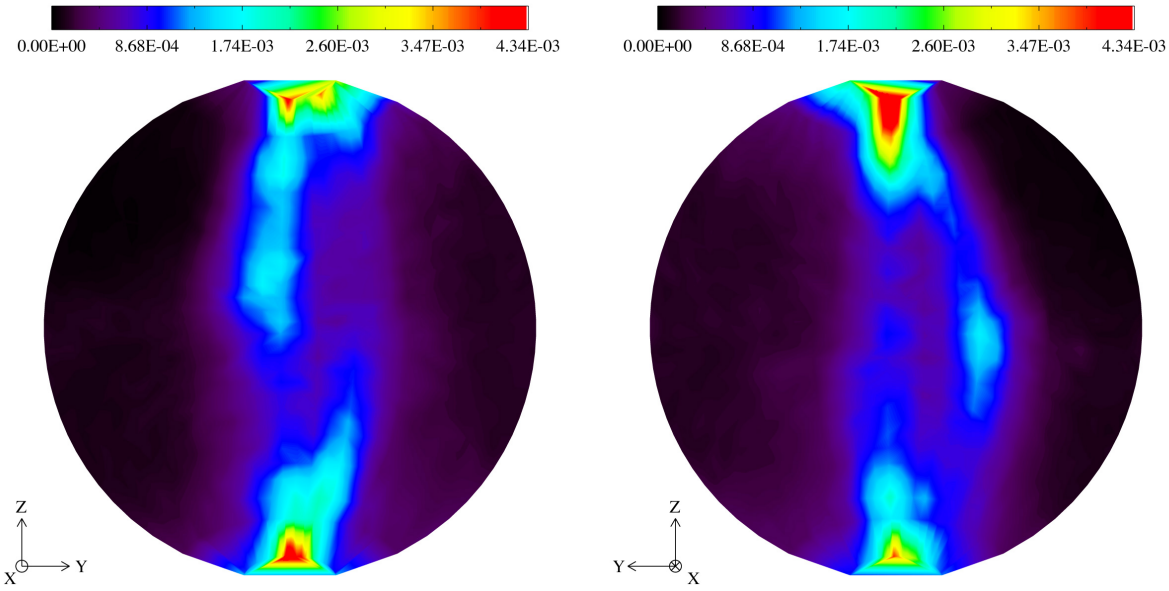

Figure 6.31. IND for the non-dense region of the 28 min sample.

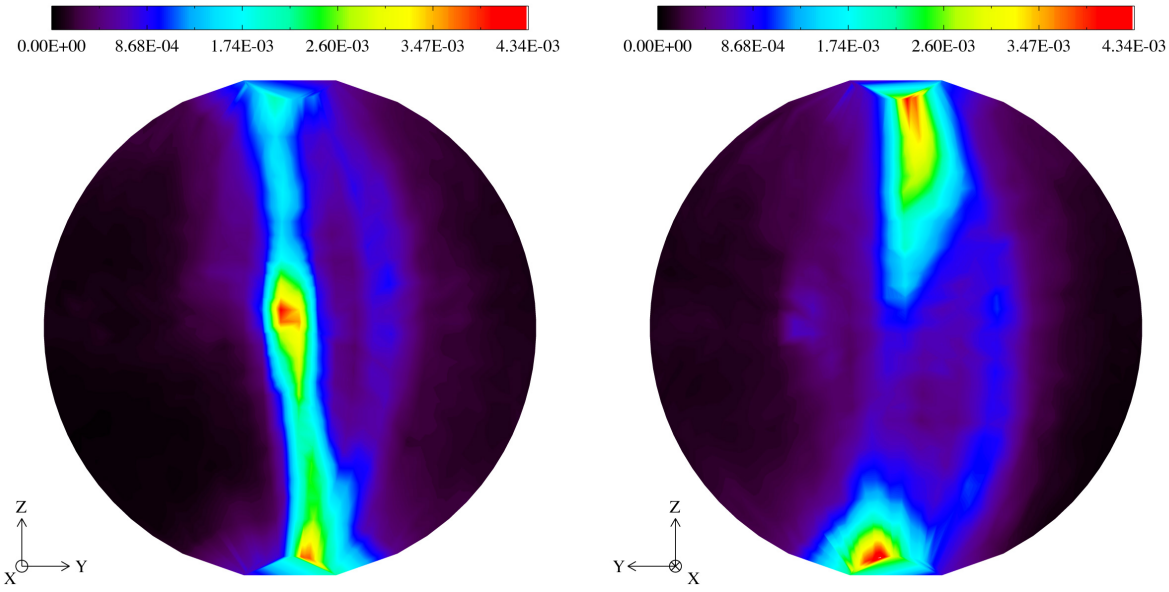

Figure 6.32. IND for the non-dense region of the 100 min sample.

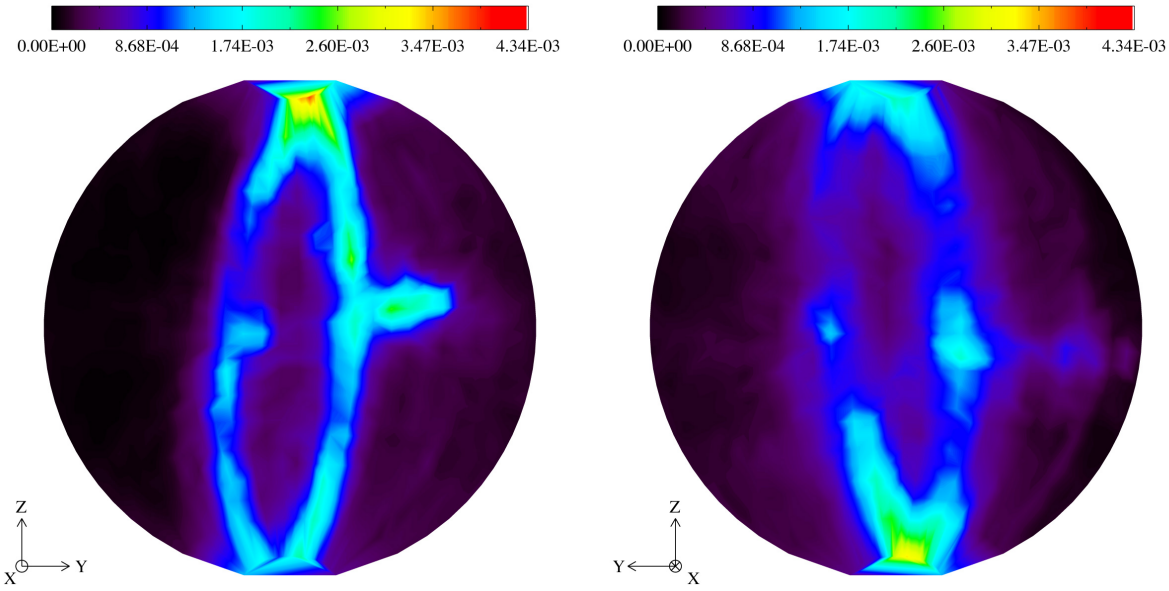

Figure 6.33. IND for the non-dense region of the 486 min sample.

6.5. Conclusions and Discussion

The Pb-69.1wt.%Sn alloy produced as described in Chapter 5 was qualitatively and quantitatively analyzed in three dimensions after 3 minutes, 28 minutes, 100 minutes and 486 minutes (approximately 8 hours) of coarsening time. Because the volume fraction of solid was not enough to fill the entire volume of the sample, the dendritic structure was analyzed both inside one of the dense dendritic regions and along the edge of these dense regions where the dendrite arms could develop more fully. The 3D reconstructions of the dendritic microstructures show the transition from a highly complex structure with many higher-order branches, to one dominated by fan-like clusters of secondary and tertiary dendrite arms growing in the x-y plane, to one in which the side branches have mostly disappeared and the structure is becoming primarily tubes aligned along the growth direction (z-axis). The Interface Shape Distributions of the dense regions show primarily solid cylinders with hemispherical caps and saddle-shaped regions where the cylinders (i.e., dendrite arms) connect to each other. By connecting regions of probability on the ISDs to specific microstructural locations, we see that quite often the dendrite arms are not cylindrical but slightly flattened due to space constraints. The ISDs of the non-dense regions showed structures which were almost exclusively solid cylinders (or cylindrical-like rods), which decreased in diameter as the structure went from primarily secondary and tertiary arms to primary dendrite stalks, and the arms became smaller compared to the scale of the structure. The structures were also analyzed for preferred directionality using Interface Normal Distributions. These plots confirmed the changes in the structure that were hypothesized after analysis of the ISDs and three-dimensional reconstructions. They also show that the primary dendrite stalks have a three-sided

shape and preferred orientation besides alignment in the growth direction. This secondary orientation is related to the sheet formation in which tin dendrites grow.

Due to experimental limitations, the size of the regions being sampled varied widely, particularly for the non-dense regions. Along with the difficultly in obtaining an accurate and consistently smoothed structure, the small size of some samples introduces sources of error into these measurements. While they can be used to make some observations about these types of directional dendritic structure, further work is needed to determine how significant these sources of error are. The results could be improved with better experimental data; namely by taking thinner sections to reduce the wedding cake effect and the need for such extensive smoothing. The serial sectioner used for this work has been used to produce sections as small as $3\mu m$, as compared to the nominally $5\mu m$ sections used here, however since the Pb-Sn alloy is so soft, with very thin sections, the blade has a tendency to smear the surface instead of cut it. Increasing the resolution in the z-direction also requires more time sectioning and more segmented images to sample the same volume of material. However, as this work continues, particularly if better insight into the dendrites at short coarsening times is desired, better z-resolution is probably necessary.

CHAPTER 7

Spatial Correlations in Directionally Solidified Dendrites

The method for calculating spatial correlations of curvature on complex surfaces described in Chapter 3 was applied to directionally-solidified dendrites coarsened for various lengths of time. Here, changes in spatial correlation with coarsening time and volume fraction solid are discussed. The data being used is that presented in Chapter 6 along with several other samples which were created earlier, with volume fractions of 43% and 58% solid. Complete analysis of these other volume fractions can be found in [**56**]. All samples are composed of tin dendrites in Pb-Sn eutectic which have been directionally solidified and isothermally coarsened.

There are a number of challenges when measuring spatial correlations in these experimental structures that were not present in the earlier analysis of the simulation-generated bicontinuous structures. First, as discussed previously, it is not possible to create 3D meshes that exactly reproduce the original microstructure. There will always be some degree of error due to a finite section thickness, errors during segmentation of images, and distortion due to smoothing. The spatial correlation measurements are extremely sensitive to small changes in the mesh, so one must sort out which features of the correlation plots are due to the true structure and which are not.

Secondly, the nature of the serial sectioning process and the time required to add additional images to the stack limits the size of the 3D reconstructions which can be obtained. Reconstructions tend to be much larger in the x-y plane than in the z-direction

(the sectioning direction). While the simulated structures were in a cubic volume, and the correlations could be calculated across the periodic boundaries, the available experimental structures are all quite small in the z-direction. This makes it difficult to measure three-dimensional correlations at larger radial distances. Also, as there is only one sample available for each coarsening time and volume fraction, the correlations cannot be averaged across multiple structures to reduce noise.

Despite these challenges, interesting correlation data was obtained. For these samples, 60,000 to 80,000 initial H_1 values were sampled, and the shell thickness Δr was set to $1/4(S_v^{-1})$ for increased resolution. As with the calculations in Chapters 3 and 4, the correlation functions are plotted as a function of the dimensionless curvatures $\tilde{H}_1 = H_1 S_v^{-1}$, $\tilde{H}_2 = H_2 S_v^{-1}$ and distance $\tilde{r} = r S_v^{-1}$.

7.1. Effects of Coarsening Time

The spatial correlations for two samples containing 43% solid after 24 minutes and 240 minutes of coarsening were calculated. Images of the three-dimensional reconstructions of these two samples are shown in Figures 7.1 and 7.2. The length scale increases by about 1.7 times between these two samples, which have $S_v^{-1} = 37.0$ and $62.5 \mu m$, respectively. The MCDs for these samples, Figure 7.3, show the curvature becoming more narrowly distributed about the maximum value with increasing time. A sample with the same volume fraction and 2880 minutes of coarsening was also investigated, but the S_v^{-1} was so large ($135.3 \mu m$) compared to the thickness of the sample ($475 \mu m$) that it was not possible to obtain meaningful data.

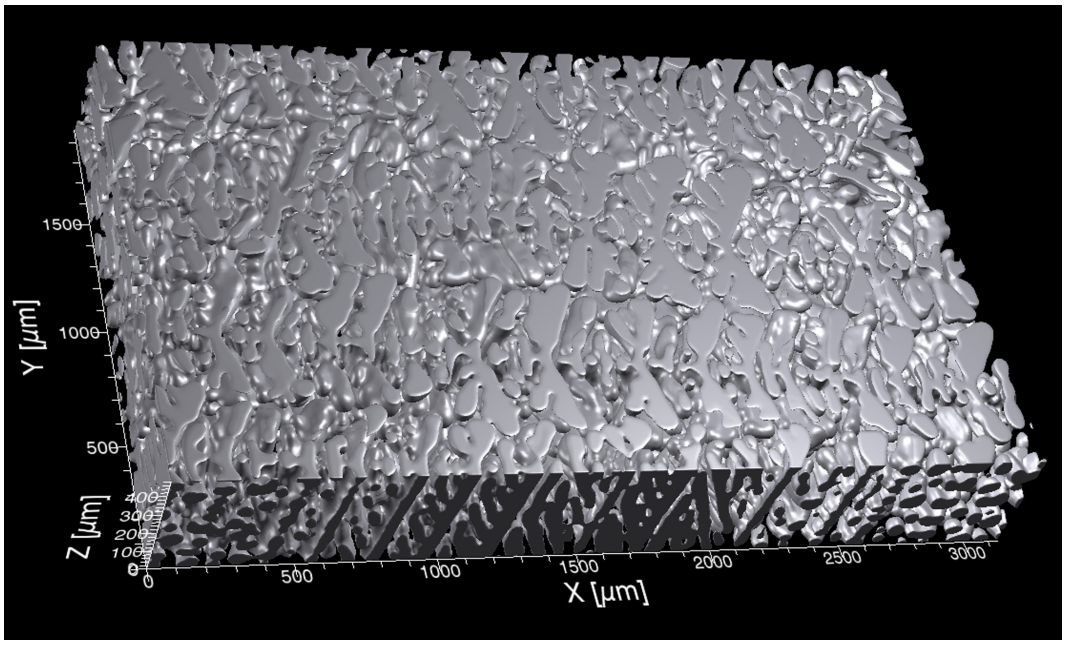

Figure 7.1. 3D reconstruction of the 43% solid sample after 24 minutes of coarsening.

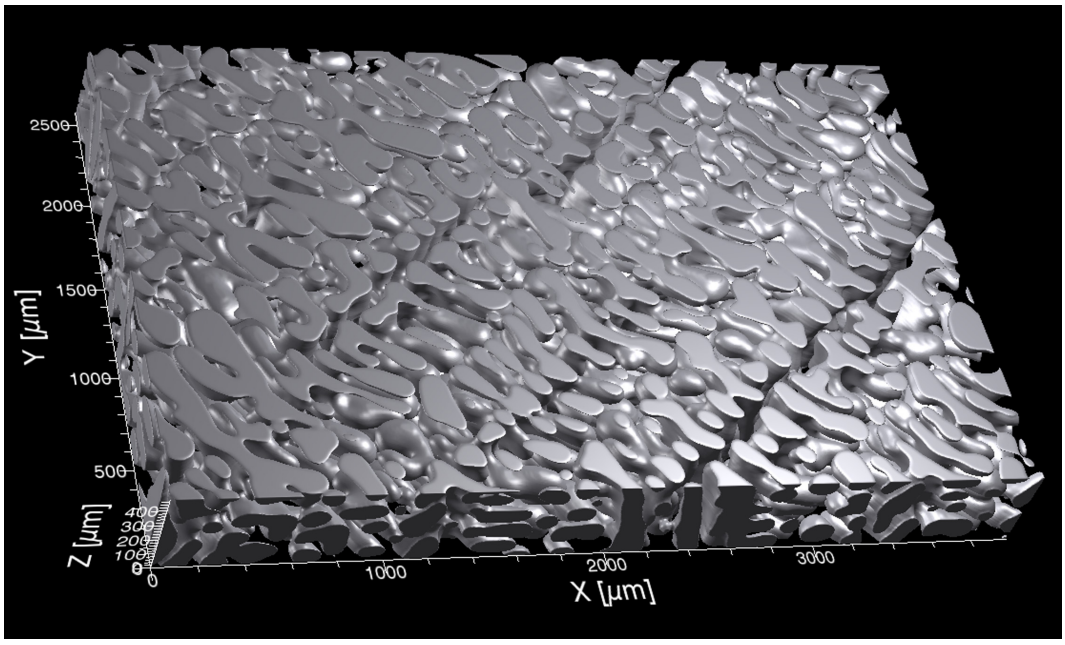

Figure 7.2. 3D reconstruction of the 43% sample after 240 minutes of coarsening.

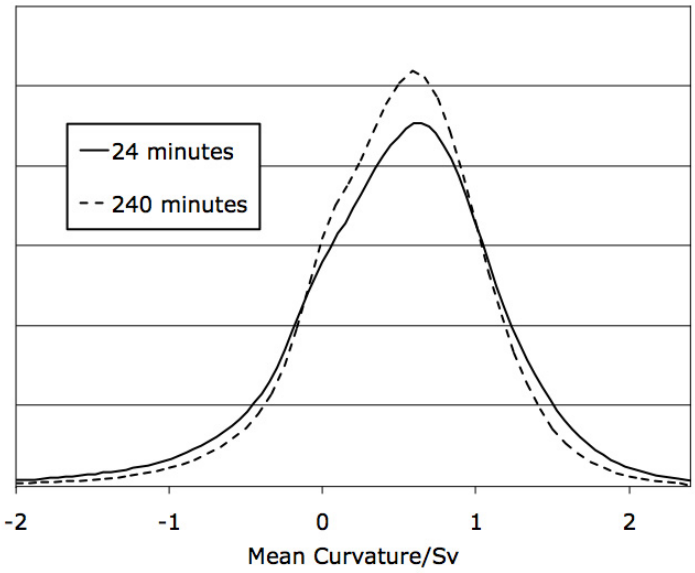

Figure 7.3. Scaled mean curvature distributions of the 43% solid structure after 24 and 240 minutes of coarsening time.

The RDFs for the two samples are shown in Figure 7.4 and 7.5 for $\tilde{r}$ = 0.25 to 2.25. Because the MCDs were quite similar in width, the plots for both samples run from $\tilde{H}$ = -2 to 2.4. This displays 99% of all curvatures in both cases. The two sets of correlations have many similar features common to this type of dendritic structure. For both samples at $\tilde{r}$ = 0.25 the plots look similar to those seen in previous chapters at very short distances, with all probability being concentrated along the $\tilde{H}_1 = \tilde{H}_2$ line. With increasing distance, this initial region of probability decreases in magnitude, with curvatures near the maximum values of the MCD ($\tilde{H}$ = 0.6) becoming uncorrelated with each other by $\tilde{r}$ = 1.5. Correlations between patches of similar large positive or large negative curvature maintain a positive correlation over longer distances, with curvatures of small negative values ($\tilde{H}$ = -1 to 0) showing the most persistent positive correlation. In both samples there is also a region of increased probability between patches of interface

having curvatures of opposite sign which appears at $\tilde{r} = 0.5$, increases as $\tilde{r}$ increases, and then decreases back to a random distribution. Finally, curvatures of $\tilde{H} = 1$ to 2 and $\tilde{H} = 0.5$ to 1 are strongly anticorrelated over the range of distances shown.

As discussed previously, the initial high probability along $\tilde{H}_1 = \tilde{H}_2$ is the result of local smoothing due to surface tension. Like the asymmetric mixture discussed in Chapter 4, these structures have less than 50% solid, so negative curvature must be relatively more correlated; thus, the plots are not symmetric across the $\tilde{H}_1 = -\tilde{H}_2$ line and two regions of negative curvature are more correlated than two regions of positive curvature with a similar magnitude. In both structures, the correlations between patches of similar negative curvature form two different peaks: one encompassing curvatures of approximately $\tilde{H} > 1.25$ and the other values of approximately $\tilde{H} < 1.25$. The more negative values are due to welding (see Figure 7.8). The welding peak disappears by $\tilde{r} = 2.5$ in 24min sample. The values closer to zero are the primary dendrite stalks (see Figure 7.6), which show the longest range correlation in the system. In the 24 minute sample, this peak is present out to $\tilde{r} = 3.75$. In the 240 minute sample, it is present until at least $\tilde{H} = 3.25$. Longer distances cannot be measured in this sample due to size constraints. It is worth noting that while the form of the correlations for the two samples are generally similar, the magnitude of the correlations and anticorrelations in the 240 minute sample are uniformly larger as the sample becomes simpler and more aligned.

While the problems with artificial welding due to over-smoothing have been extensively discussed here, examination of the original micrographs shows at least some of these to be actual events in the microstructure, at least within the resolution of the images (see Figure 7.9). If that is the case, then the structure is coarsening by arm coalescence. The

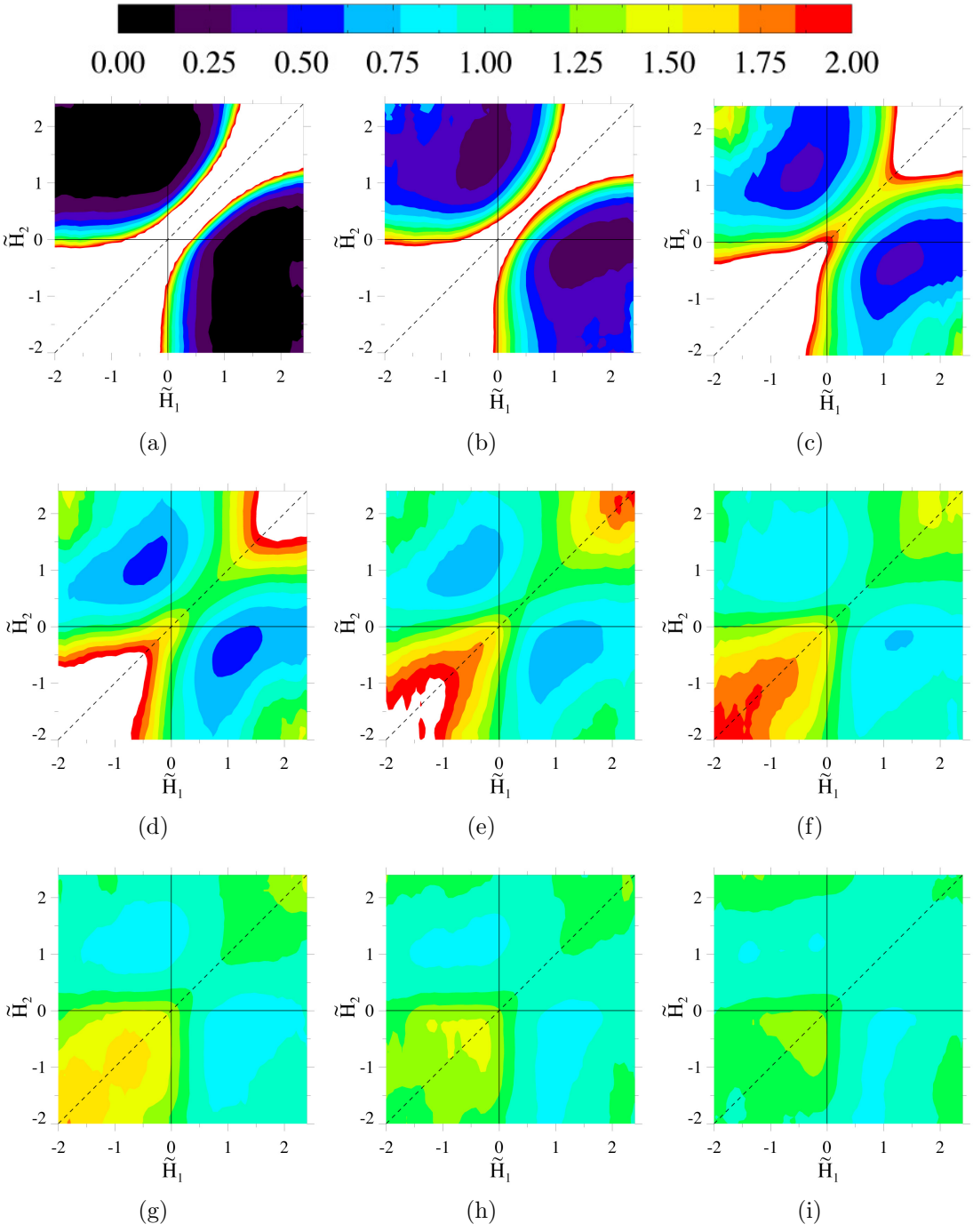

Figure 7.4. Spatial correlations of 43% solid sample after 24 minutes of coarsening for $\tilde{r}$ = a) 0.25, b) 0.50, c) 0.75, d) 1.00, e) 1.24, f) 1.50, g) 1.75, h) 2.00, i) 2.25. White indicates a probability of greater than 2.

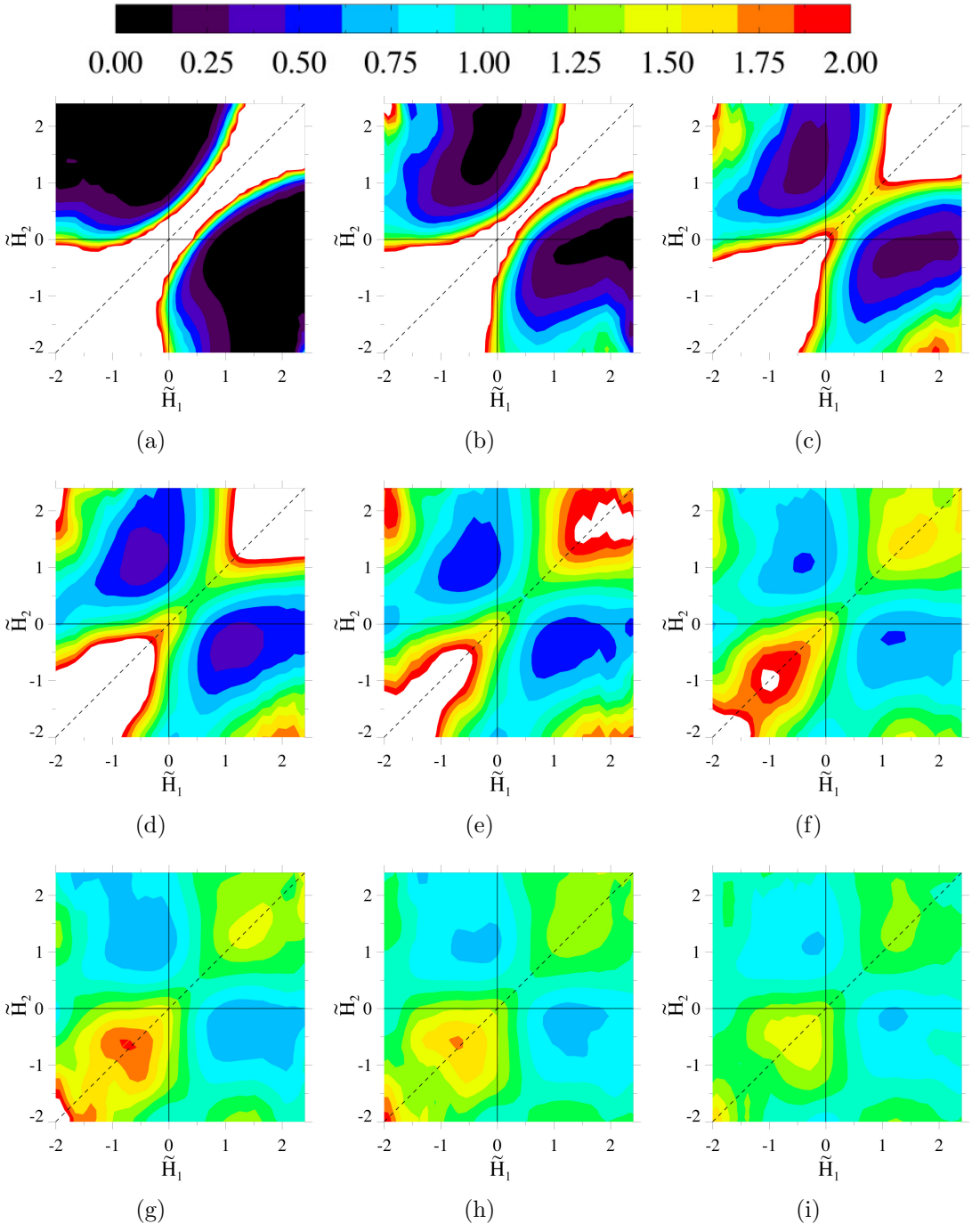

Figure 7.5. Spatial correlations of 43% solid sample after 240 minute of coarsening for $\tilde{r}$ = a) 0.25, b) 0.50, c) 0.75, d) 1.00, e) 1.24, f) 1.50, g) 1.75, h) 2.00, i) 2.25. White indicates a probability of greater than 2.

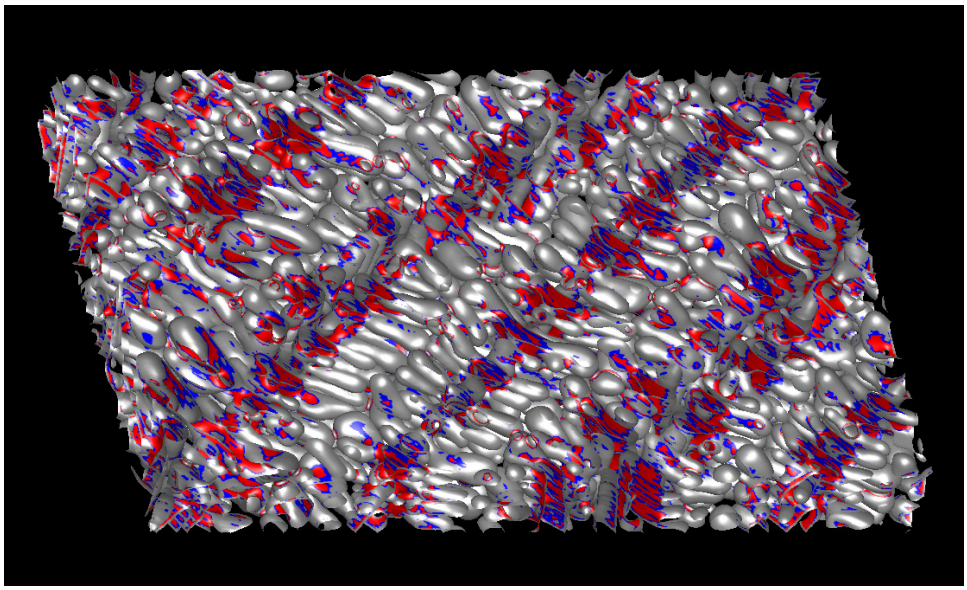

Figure 7.6. 240 minute sample with curvatures of $\tilde{H}$ = -1.25 to 0 highlighted in red and $\tilde{H} = 0$ to 0.2 highlighted in blue. Together, these curvatures correspond to the primary dendrite stalks which run in parallel sheets through the structure.

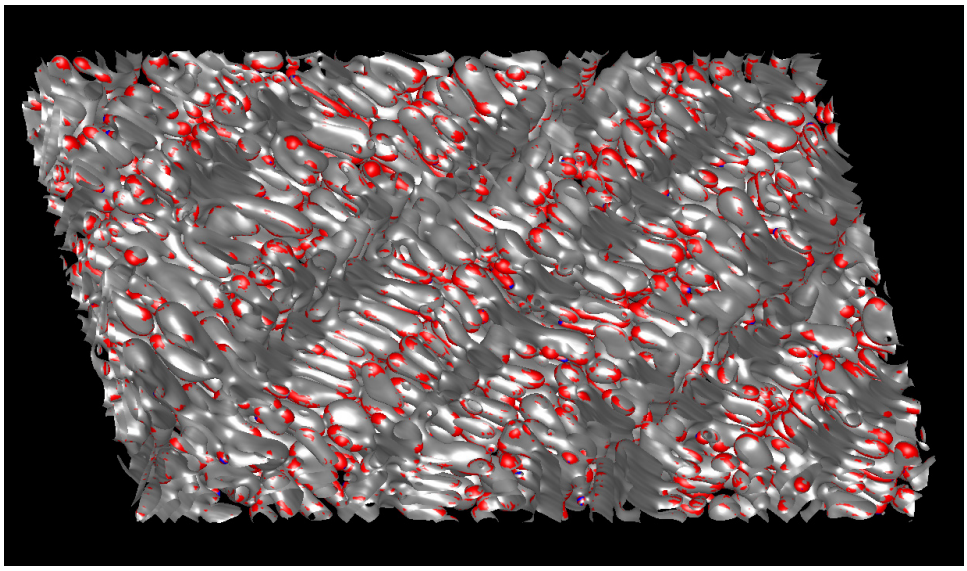

Figure 7.7. 240 minute sample with curvatures of $\tilde{H} > 1$ highlighted. These curvatures correspond to the tips of the dendrite arms.

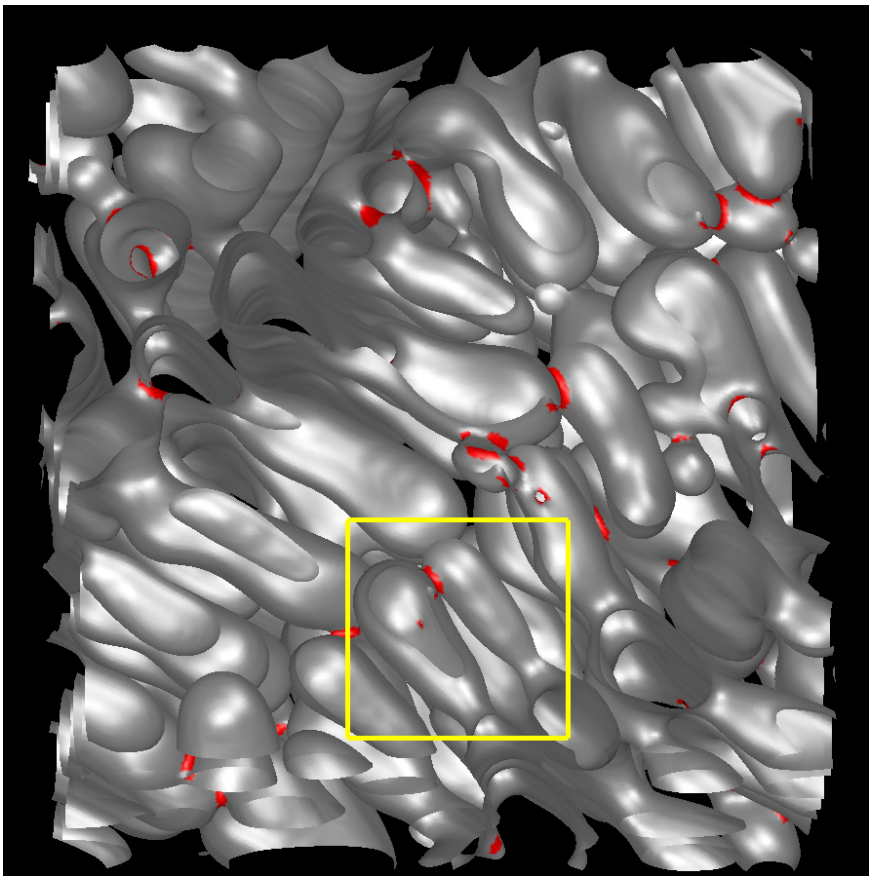

Figure 7.8. 240 minute sample with curvatures of $\tilde{H} < -1.2$ highlighted. These curvatures correspond to the neck region where two interfaces have become welded together. The box indicates a region of coalescence by tear-drop shaped arms.

region indicated by the box in Figure 7.8 looks very similar to Model 4 in Figure 2.1 which depicts dendrite arms obtaining tear-drop shapes which touch near the tips where the arms are the widest and then coalesce. Visual examination of the structures indicates that Model 2, axial remelting, is also a coarsening method used by these systems. This makes for a very different coarsening process than what was described earlier for the bicontinuous structures that coarsen by pinching events.

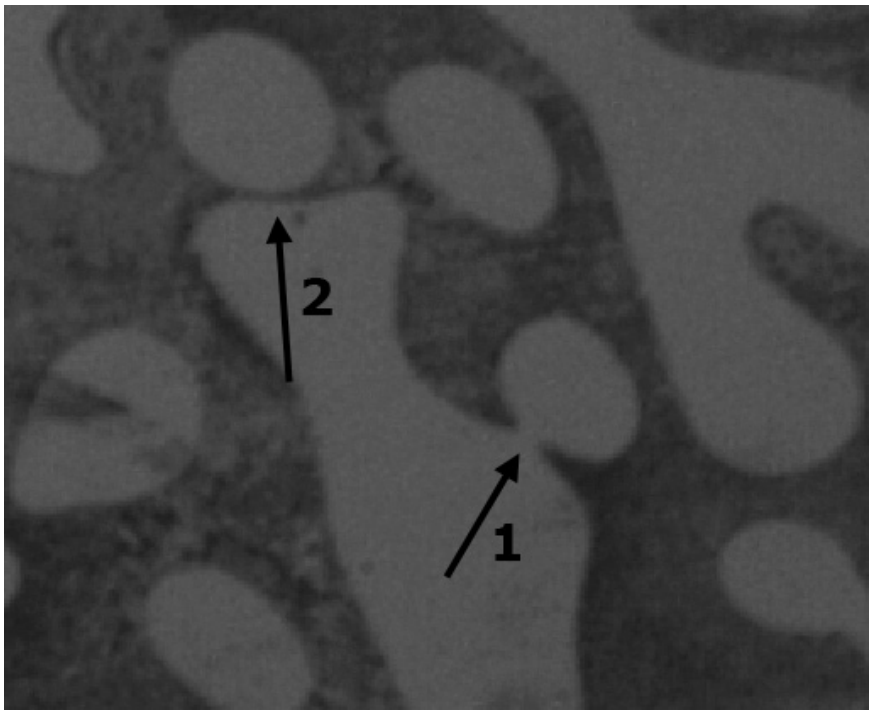

Figure 7.9. An original micrograph of the 240 minute sample, with arrow 1 indicating a region of actual coalescence, while arrow 2 indicates a region that would likely become welded during smoothing.

The regions of low negative curvature associated with the stalks show a strong anti-correlation with regions of moderate to high positive curvature. These positive regions correspond to the tips of the dendrite arms (Figure 7.7). Thus, the length over which this anticorrelation persists contains information about the average length of the dendrite arms. In the 240 minute sample, the anticorrelation persists to at least $\tilde{r} = 3.25$ which is the longest distance measurable in this sample. $\tilde{r} = 3.25$ corresponds to a distance of $220\mu m$. The secondary dendrite arm length was measured to be approximately $300\mu m$. Thus, we speculate that if the correlations could be measured for longer distances, the anticorrelation would disappear shortly and then likely become positively correlated. In

the 24 minute sample, the anticorrelation persists to a distance of 70-80μm, which corresponds to the average distance from the stalk to the tip of the first tertiary arm. As the anticorrelation disappears, a positive correlation between stalks ($\tilde{H} = -1$ to 0) and tips ($\tilde{H} > 2$) appears for $\tilde{r} > 2.5$. Most of these tertiary arms have disappeared by 240 minutes and there is very little curvature of $\tilde{H} > 2$.

The positive correlation between regions of similar positive curvature is due to clustering of dendrite tips. This correlation region has a very high value initially and then exhibits a uniform decay with increasing distance. There appears to be no oscillation which would indicate an average spacing between individual arms. Either there is too much variation in spacing between arms to pick up an average value, or with the current noise level and colorbar scaling, the plots are not sensitive enough to pick it up.

The correlation between positive and negative regions is due to spacing between dendrite tips and welded regions. For the 240 minute sample, two things about this peak confirm that the welding events are occuring between the highly curved dendrite tips. First, this peak appears at a very short distance ($\tilde{r} = 0.5$) and shows the strongest correlation from $\tilde{r}$ =0.75 to 1.25. Second, the peak is initially centered about a positive value of $\tilde{H} = 2$ and with increasing distance $\tilde{r}$ shifts downwards towards $\tilde{H} = 1$, indicating that the most highly curved interfaces are nearest the welds. This is less clear for the 24 minute coarsened sample, as there is much more welding which occurs between entire arms (see Figure 7.10) of a variety of sizes. Therefore the weld regions are not correlated to any particular curvature of the arms except the very highest curvature found on the tips of all tertiary arms. More work is necessary to determine how much of this extensive welding is the result of over-smoothing. However, even if the welding is due to over-smoothing,

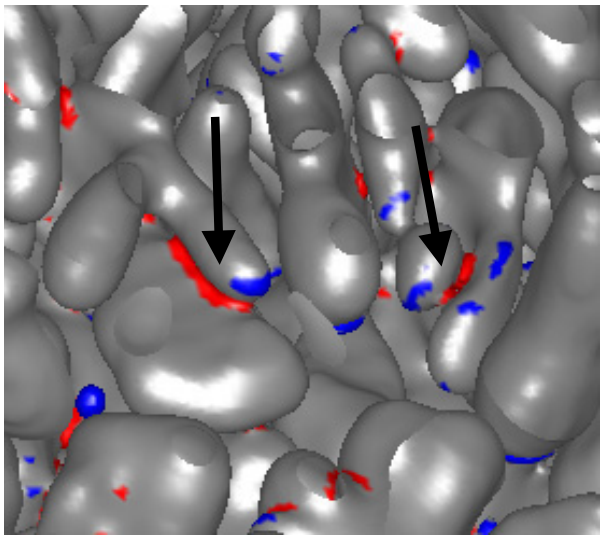

Figure 7.10. 24 minute sample showing the extensive welding in this structure. Red highlights $\tilde{H} < -1.2$ and blue highlights $\tilde{H} > 2$. Arrows indicates the type of region which causes the correlation between very high negative and positive curvatures.

it does indicate that the arms in these regions are very close to each other, within a few voxels.

7.2. Dense versus Non-dense Regions

The RDFs for the dense and non-dense regions of the Pb-69.1wt%Sn sample (3D reconstructions shown in Figures 6.5 and 6.9) are given in Figure 7.11 and 7.12 for $\tilde{r} =$ 0.25 to 2.25. To be consistent with the plots in the previous section, the axes are scaled from $\tilde{H} = -2$ to 2.4. This displays 98% of all curvatures for both regions. The MCDs for these two samples are given in Figure 7.13. At longer distances for the non-dense region, Figure 7.12(f)-(i), the plots are not symmetric across the $\tilde{H}_1 = \tilde{H}_2$ line but exhibit a sort of horizontal smearing effect. This is due to the limited size of the sample, particularly in the z-direction. Although the sample is still thicker than twice the radial distance being measured, in order to keep the measurements inside the sample, the possible $\tilde{H}_1$ values which can be used are very limited. This causes a distortion of the probability plots, but previous work using the larger bicontinuous structures has shown that the general trends are still correctly displayed.

The correlation plots in Figures 7.11 and 7.12 show many of the features discussed in the previous section. While at the shortest distances, all probability falls along the $\tilde{H}_1 = \tilde{H}_2$ line, and the correlation is very strong for all values of $\tilde{H}$, the samples are less than 50% solid and so the negative curvatures exhibit the highest correlations. At moderate distances, there is a positive correlation between regions of large positive curvature and large negative curvature. In the dense region, this peak indicates a correlation between welded regions and the dendrite arm tips, as discussed above. In the non-dense sample, however, the high-magnitude negative curvature does not correspond to welding but to the regions between tertiary arms, as illustrated in Figure 7.14. Thus this peak represents the correlation between the tips of the tertiary arms and the bases of those arms. The

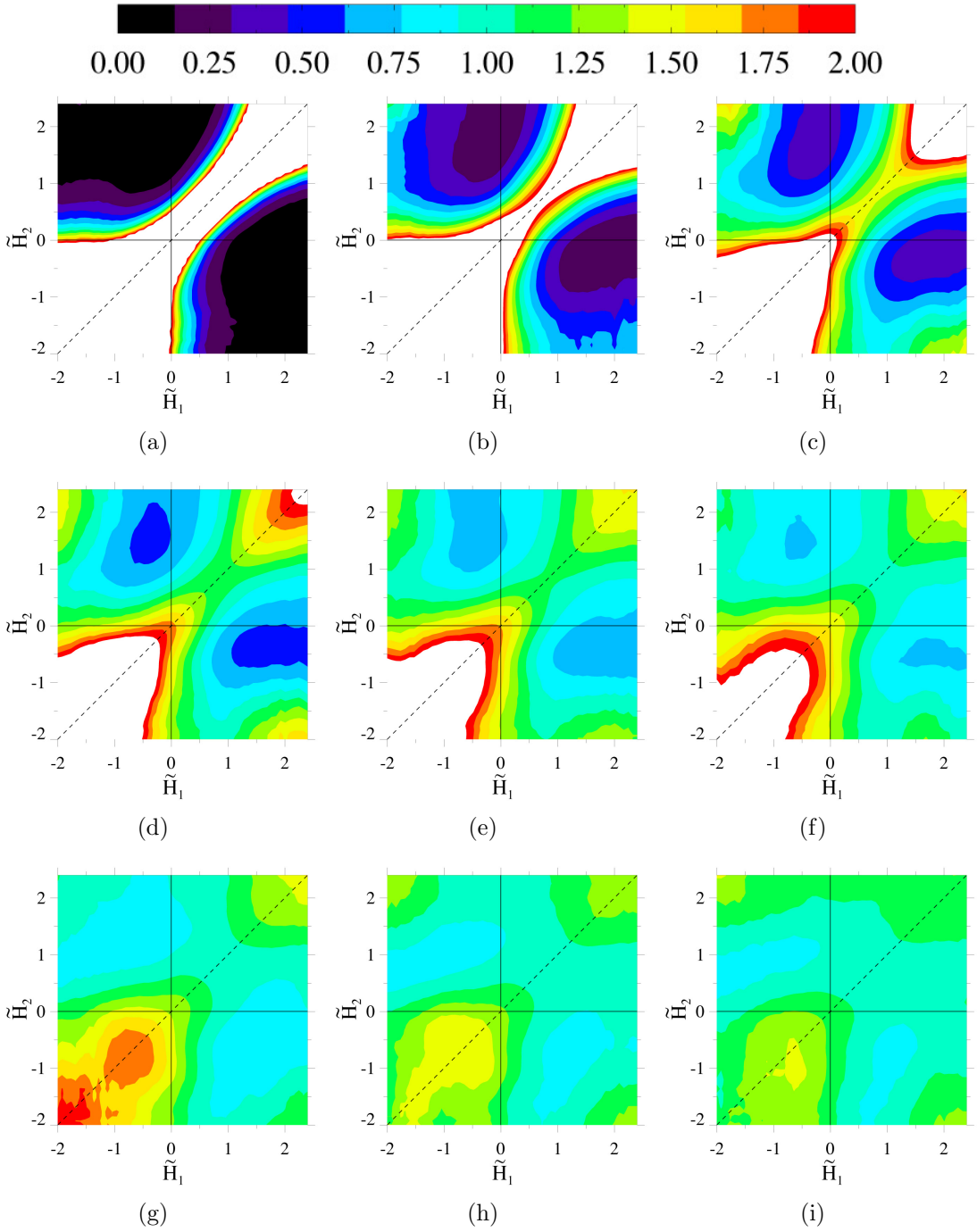

Figure 7.11. Spatial correlations of dense region after 28 minutes of coarsening. Plots were constructed using a shell of thickness 1/4 at $\tilde{r}$ = a) 0.25, b) 0.50, c) 0.75, d) 1.00, e) 1.24, f) 1.50, g) 1.75, h) 2.00, i) 2.25. White indicates a probability of greater than 2.

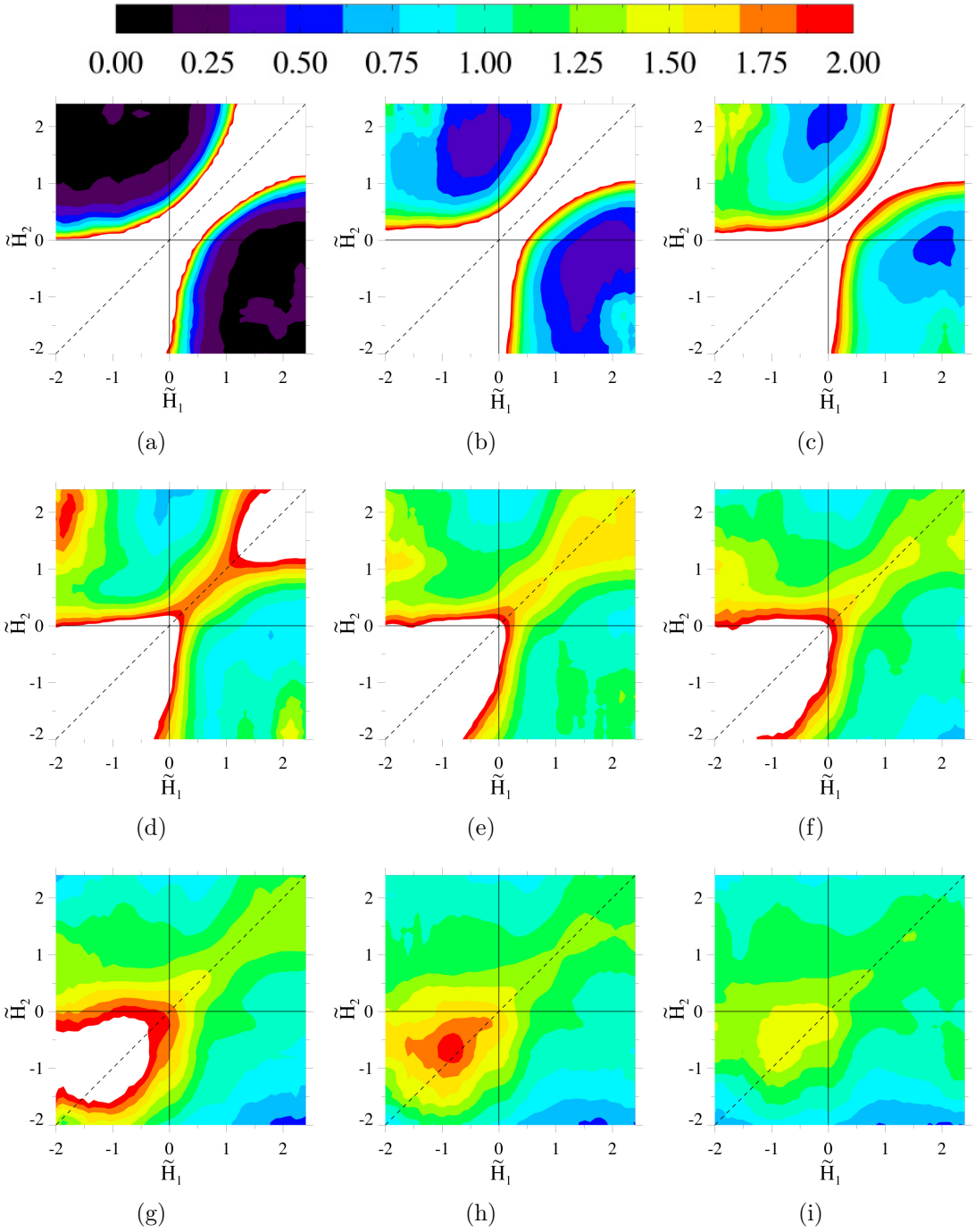

Figure 7.12. Spatial correlations of non-dense region of 28 minute coarsened sample. Plots were constructed using a shell of thickness 1/4 at $\tilde{r}$ = a) 0.25, b) 0.50, c) 0.75, d) 1.00, e) 1.24, f) 1.50, g) 1.75, h) 2.00, i) 2.25. White indicates a probability of greater than 2.

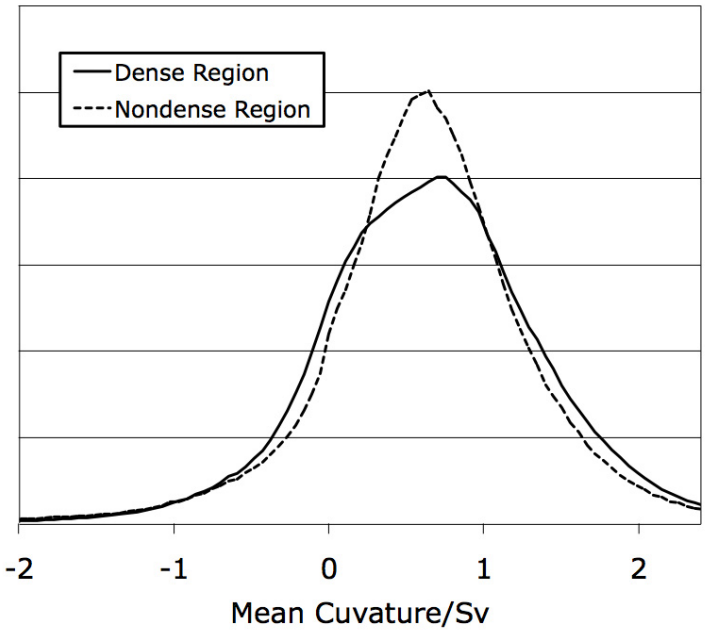

Figure 7.13. Scaled mean curvature distributions of 28 minute coarsened sample in the dense and non-dense regions.

appearance of the peak from $\tilde{r} = 0.5$ to 1.25, or 20 to 50μm suggests the range of tertiary dendrite arm lengths at this time. Notice that the peak corresponding to this phenomenon encompasses a different range of negative curvature values ($\tilde{H}$ = -1 to -2) than seen in previous peaks attributable to welding ($\tilde{H}$ < -1.5). The lack of welding is also noticeable because there is only one peak in the $\tilde{H}_1 = \tilde{H}_2$ region, just below $\tilde{H} = 0$, instead of the two peaks seen previously.

Two other differences between the dense and non-dense regions can be noted along the positive region of the $\tilde{H}_1 = \tilde{H}_2$ line. First, the positive correlation along the length of $\tilde{H}_1 = \tilde{H}_2$ line is maintained for a longer distance in the non-dense sample. In the dense sample, the curvatures nearest the maximum value of the MCD (approximately $\tilde{H} = 0.4$ to 1.2) become uncorrelated with themselves by a distance of $\tilde{r} = 1.5$ and remain uncorrelated

at all larger distances. In all previous samples, both dendritic and bicontinuous, the curvatures near the maximum of the MCD have the shortest self-correlation. In the non-dense sample, these curvatures correspond to the highly aligned tertiary dendrite arms and maintain a positive self-correlation for all currently measurable distances, while other curvatures do exhibit a random distribution.

Finally, the self-correlations for high positive curvature ($\tilde{H} > 1.5$) drop off more quickly in the non-dense structure for distances of $\tilde{r} \geq 1.5$. In the non-dense structure, the dendrites have more room to spread out, thus the tips are not as tightly clustered. In the non-dense region, there are generally no more than one or two immediately surrounding tips which create the positive correlation between regions of large positive curvature. In the dense region, there may be as many as five or six tips packed into the area being sampled by $\tilde{r} = 2.25$.

7.3. Effects of Changing Volume Fraction

From the data already presented, Figure 7.4, 43% solid after 24 minutes of coarsening, and Figure 7.11, locally 37% solid after 28 minutes of coarsening, can be compared. These two samples have S_v^-1 values of 0.0270 and 0.0248 $1/\mu m$, respectively, a difference of about 8%. The difference is likely due to the slight differences in coarsening time and volume fraction, as well as different amounts of welding due to different initial segmentation and thresholding. The smoothing process was nearly identical. The correlation plots are quite similar, although the positive correlations in Figure 7.11 have slightly higher values, particularly for the self-correlations of negative curvatures. This indicates that, in general, despite the fact that the sample in Figure 7.11 comes from an alloy where

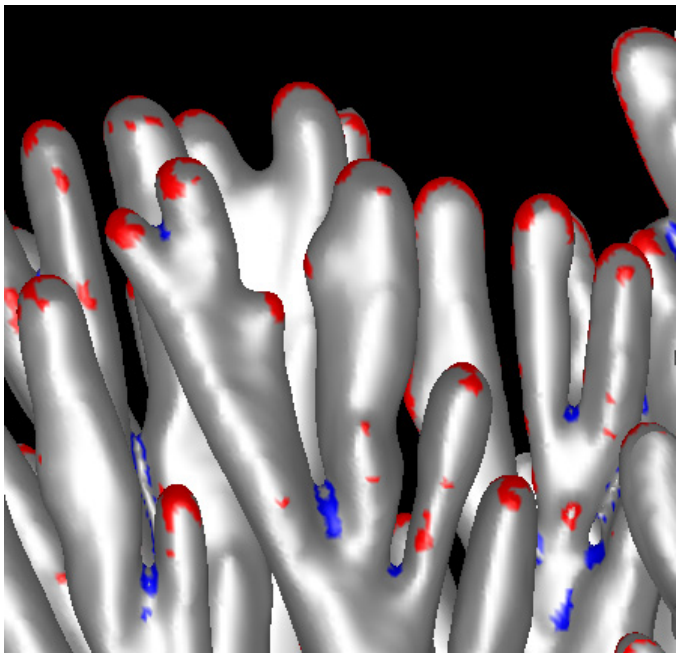

Figure 7.14. Illustration of correlation between tips and bases of tertiary dendrite arms. Curvatures of $\tilde{H} = 1.5$ to 3 highlighted in red and curvatures of $\tilde{H}$ = -1 to -2 highlighted in blue.

the overall volume fraction is just 22% solid and the solid is not uniformly distributed throughout the sample, the growth in the dense regions is comparable to that in fully-dense samples.

There is also data available for the Pb-Sn system for directionally solidified samples of 58% solid and 81% solid at a variety of coarsening times, as well as the 43% and 22% (locally 37% in the dense regions) samples already discussed. It remains to future work to probe further the changes in spatial correlation with increasing volume fraction.

7.4. Correlations after Long Coarsening Times

After very long coarsening times, all secondary dendrite arms disappear and the structure becomes vertically aligned tubes of increasingly circular crosssection. Figure 7.15

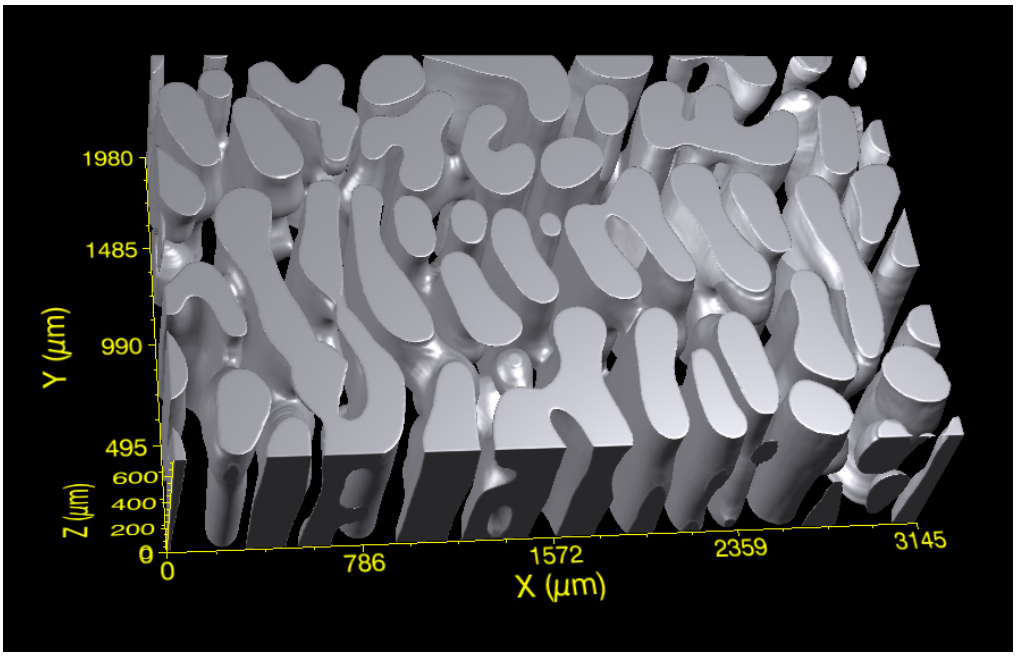

Figure 7.15. 3D reconstruction of the 58% solid sample after 4320 minutes (3 days) of coarsening.

shows a 58% solid sample after three days of coarsening time, which consists of strongly aligned, horizontally elongated solid tubes. The RDF for this structure is shown in Figure 7.17. These plots cannot be directly compared to previous ones because axes are scaled slightly differently, from $\tilde{H}$ = -1.8 to 1.8. The increased noise is not due to error in the 3D mesh, as the large structure is easier to smooth and so more accurately represents the original microstructure. However, the very large increase in length scale (S_v^{-1} is 2 to 4 times larger than all other structures discussed here) means that the sample size is relatively smaller and therefore less data is available to sample.

The plots show three primary positive correlations, always between regions of similar curvature. These three regions are highlighted in Figure 7.16. Curvature with large positive values corresponds to the highly curved sides of the elongated tubes. Curvature

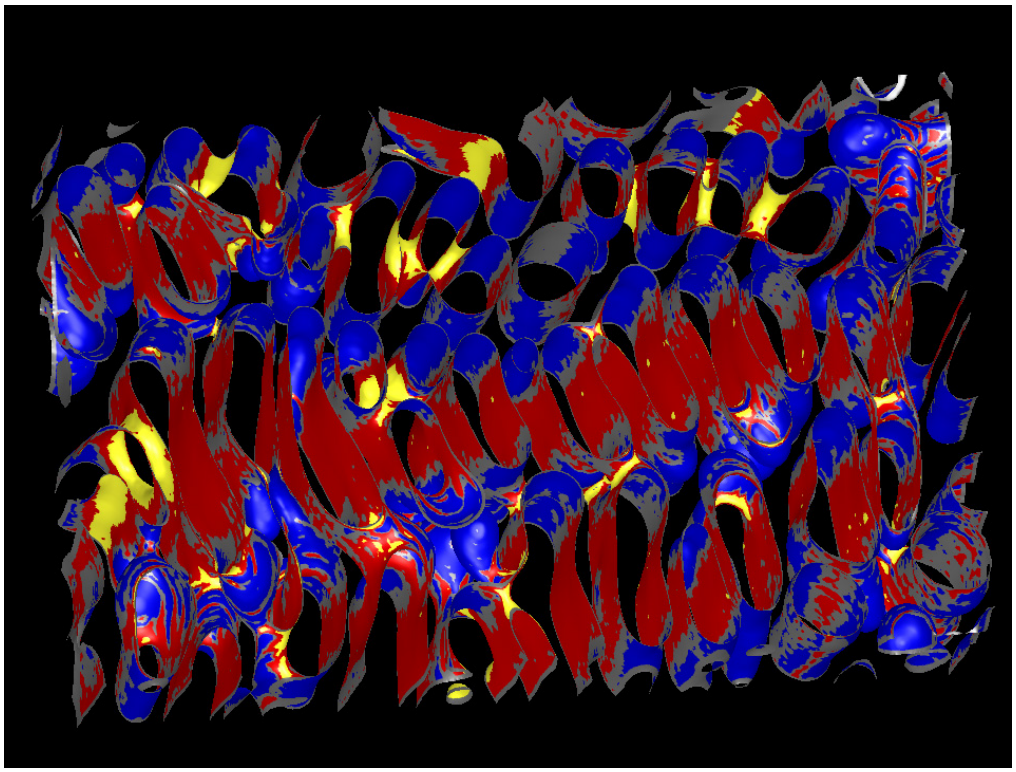

Figure 7.16. Sample shown in previous figure with blue highlighting $\tilde{H} >$ 0.5, yellow highlighting $\tilde{H} >$-0.5 and red highlighting $\tilde{H} =$ -0.5 to 0.2. These are the three primary regions showing positive correlation for this structure.

with large negative values corresponds to regions of horizontal interface which connect some of the vertical tubes. These regions have self-correlation values which persist over the longest distance. There is also a small peak for $\tilde{H}$ just below 0, which corresponds to the large flat sides of the elongated tubes.

The smearing effect in the plots due to small sample size begins at $\tilde{r} = 2$, and $\tilde{r}$ can only be measured out to a distance of $\tilde{r} = 2.5$, even though this sample is 1.5 times thicker than any of the other dendritic samples discussed here. Since it is not feasible to go back and obtain thicker samples, a new method of calculating correlations was developed for this type of large S_v^{-1}, highly-directional sample. Instead of calculating

the correlations in all three dimensions, the radial distance was taken only in the x-y plane. $\tilde{H}_1$ values were chosen throughout the thickness of the sample so that all x-y planes available were sampled and averaged together. The plane was defined to be all values which fell inside the shell of radius $\tilde{r}$ and thickness $\Delta\tilde{r}$ as defined previously, and which also had $\tilde{H}_2(z) = \tilde{H}_1(z) \pm 15\mu m$. It was hoped that this would be a way to make use of the larger dimensions of these samples without sacrificing any vital information, as the samples change very little in the z-direction. Figure 7.18 shows the correlations in the x-y plane for the same sample shown in Figure 7.15. Although noisier, the plots are quite similar to those calculated in the normal way in Figure 7.17 and, although not shown, have been calculated for distances as long as $\tilde{r} = 4.25$. More investigation is necessary to completely understand the potential of this new method.

7.5. Summary

The new technique for measuring spatial correlations of complex surfaces has been applied to directionally solidified dendritic samples. The changes with coarsening time from 24 to 240 minutes in a 43% solid sample are analyzed. The differences between the dense and non-dense region of the 22% solid sample are also discussed. Finally, the technique is adapted to the available, highly-directional samples with small z dimensions by measuring correlations only in the x-y plane. We have used the technique to identify length scales in these complicated structures such as the average distance from base to tip of dendrite arms. With more refinement, this technique, in both two and three dimensions, will be able to be used to pick up increasingly subtle features of these structures. The work presented here does prove that the technique works for a variety of morphologies,

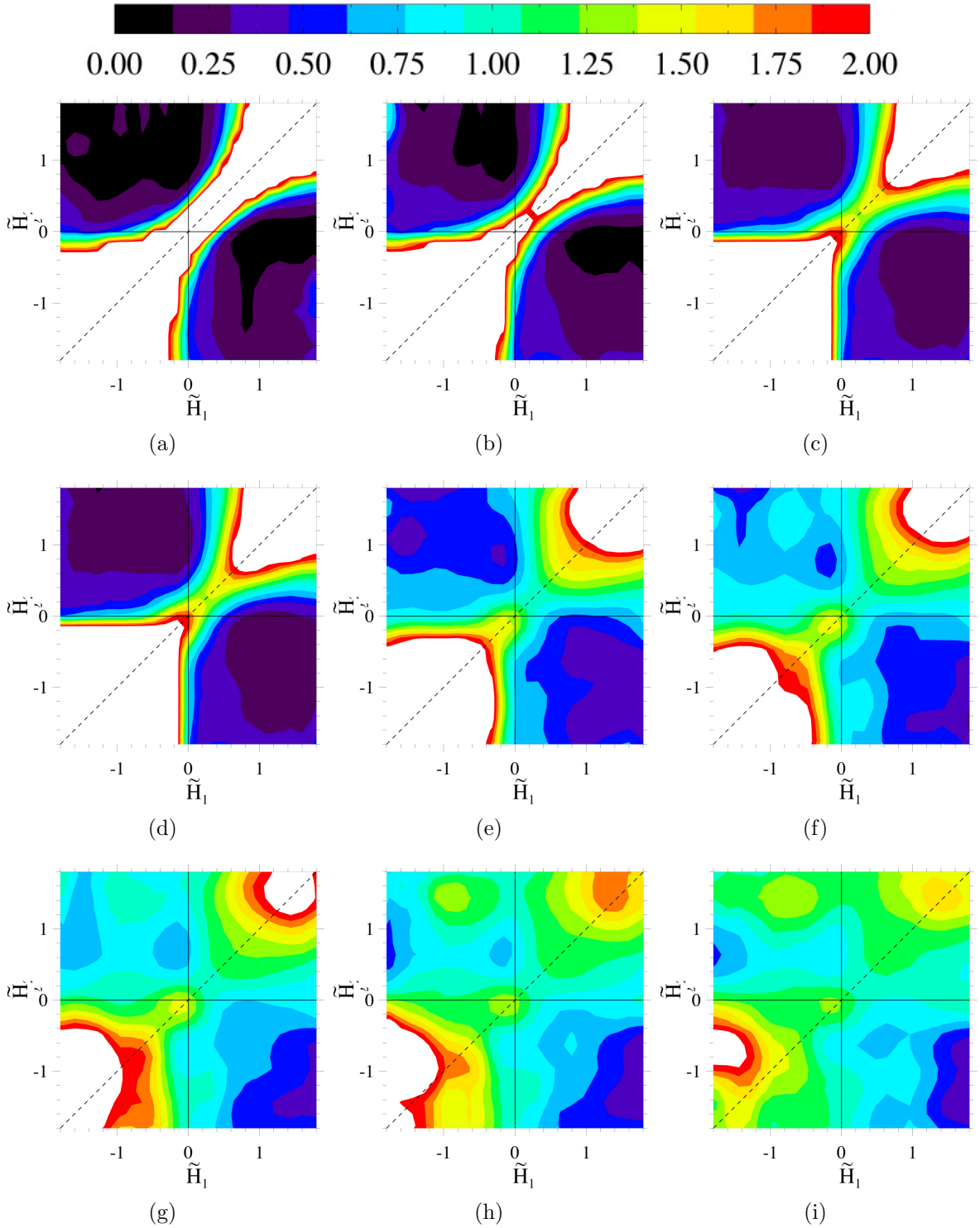

Figure 7.17. Spatial correlations of 58% solid sample after three days of coarsening for $\tilde{r}$ = a) 0.25, b) 0.50, c) 0.75, d) 1.00, e) 1.24, f) 1.50, g) 1.75, h) 2.00, i) 2.25. White indicates a probability of greater than 2.

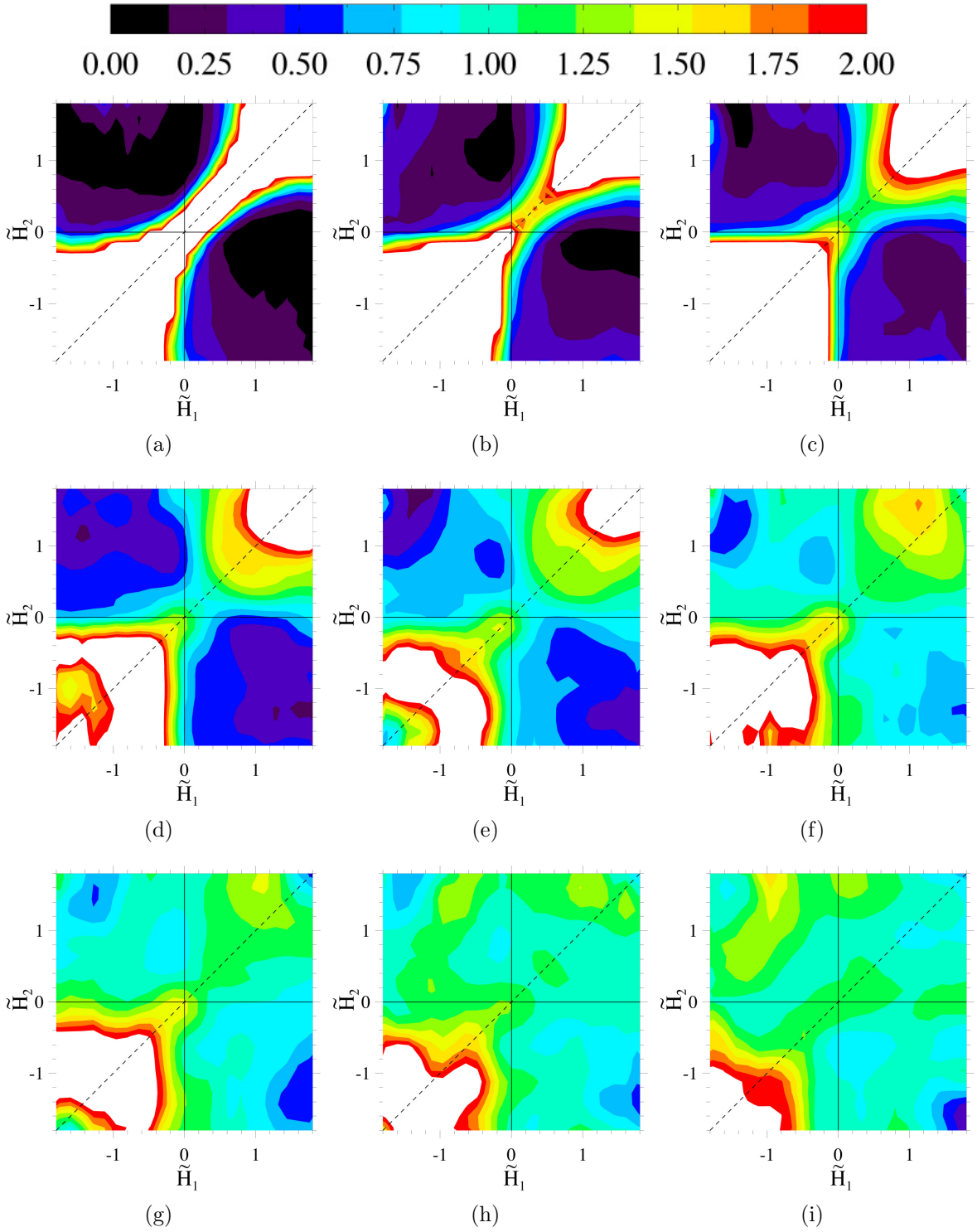

Figure 7.18. Spatial correlations in the x-y plane of the 58% solid sample after three days of coarsening for $\tilde{r}$ = a) 0.25, b) 0.50, c) 0.75, d) 1.00, e) 1.24, f) 1.50, g) 1.75, h) 2.00, i) 2.25. White indicates a probability of greater than 2.

and the potential for future work and impact is great. The use of other techniques, such as x-ray tomography, to obtain larger and more accurate three-dimensional meshes for analysis will also provide a great leap forward.

CHAPTER 8

Conclusions

Two different types of microstructures were subjected to quantitative three-dimensional analysis. First, simulated bicontinuous mixtures were used to develop a new method of quantifying the morphology of topologically complex interfaces by calculating the spatial correlation of interfacial curvature. Second, three-dimensional reconstructions of directionally solidified and isothermally coarsened dendritic samples were created using serial sectioning, and analyzed using a variety of techniques including the newly developed method of calculating spatial correlations.

This method for calculating spatial correlations of interfacial curvature uses a radial distribution function (RDF) calculated directly from the surfaces of a three-dimensional structure. This method is independent of morphology and can be used for any type of structure. The usefulness of such a calculation is demonstrated by calculating correlations of two bicontinuous, two-phase mixtures produced using phase field modeling with conserved and nonconserved dynamics, respectively. It was found that the long-range diffusive interactions resulting from conserved dynamics yield positive correlations which display a decreasing oscillation with increasing distance between regions of similar curvature and regions of opposite curvature. These correlations were observed out to a distance of seven times the characteristic length of the system and indicate regularly spaced regions of positive and negative curvature which is a new characteristic length scale for

this structure. Despite the local nature of the interfacial evolution process in the nonconserved case, positive correlations between similar curvature were observed on a relatively long scale (greater than two times the characteristic length of the system). These correlations are attributed to the persistence of high curvature tunnels in the structure, with the spacing between these tunnels constituting a new characteristic length scale for these structures. The time independence of both the scaled spatial correlation functions and the interface shape distributions indicate that the interfacial morphologies in these cases assume a unique time-independent form.

Spatial correlations were also compared for symmetric and asymmetric bicontinuous mixtures produced using conserved dynamics. This analysis was performed by calculating the RDF for correlations between all existing values of curvature at a single radial distance, and also between specific curvature values identified as primary correlation regions. The observed correlations are attributed to interfacial smoothing effects at short distances, diffusional constraints at intermediate distances, and the repeating nature of the structure at longer distances. The correlation analysis of the asymmetric mixture has provided important details about the nature of changes to a spinodal structure as it moves away from a critical quench, and possibly the nature of the breakup of such structures. The asymmetric mixture also showed correlations out to a distance of about seven times the characteristic length, with particularly strong correlations between patches of negative curvature. The negative curvature must be highly clustered to stable: diffusion would eliminate smaller patches very quickly, and some negative curvature is geometrically necessary to have a three-dimensional, bicontinuous structure.

On the experimental side, a Pb-69.1wt.%Sn alloy was created and directionally solidified, then coarsened just above the eutectic temperature for 3 minutes, 28 minutes, 100 minutes, 486 minutes and 3 days. The 3 day sample was not analyzed because it had undergone complete sedimentation. Because the volume fraction of solid was not enough to fill the entire volume of the sample, the dendritic structure was analyzed both inside one of the dense dendritic regions and along the edge of these dense regions where the dendrite arms could develop more fully. The 3D reconstructions of the dendritic microstructures show a transition from a highly complex structure with many higher-order branches, to one dominated by fan-like clusters of secondary and tertiary dendrite arms growing in the x-y plane, to one in which the side branches have mostly disappeared and the structure is becoming primarily tubes aligned along the growth direction (z-axis). The Interface Shape Distributions of the dense regions show primarily solid cylinders with hemispherical caps and saddle-shaped regions where the cylinders (i.e., dendrite arms) connect to each other. By connecting regions of probability on the ISDs to specific microstructural locations, we see that quite often the dendrite arms are not cylindrical but slightly flattened due to space constraints. The ISDs of the non-dense regions showed structures which were almost exclusively solid cylinders (or cylindrical-like rods), which decreased in diameter as the structure went from primarily secondary and tertiary arms to primary dendrite stalks, and the arms became smaller compared to the scale of the structure. The structures were also analyzed for preferred directionality using Interface Normal Distributions. These show that the primary dendrite stalks have a three-sided shape and preferred orientation besides alignment in the growth direction. This secondary orientation is related to the sheet formation in which tin dendrites grow.

Finally, the new technique for measuring spatial correlations of complex surfaces was also applied to directionally solidified dendritic samples, including some of the samples discussed above. The RDFs show correlations of curvature due to the dendrite stalks, the arm tips, and coalescence events. The extent of a strong anticorrelation between curvatures associated with the stalks and the tips gives provides information about the average secondary dendrite arm length. The changes with coarsening time from 24 to 240 minutes in a 43% solid sample are analyzed. At the shorter time, correlations are seen between the base and tips of tertiary arms, while at the longer time, the tertiary arms have mostly disappeared and the correlations show the distance between the base and tips of secondary arms. More coalescence between highly-curved dendrite tips is also seen after 240 minutes. The differences between the dense and non-dense region of the 22% solid sample are also analyzed. Most notably, it was found that in the non-dense sample, the curvature values corresponding to the maximum value of the mean curvature distribution (MCD) do not have the shortest self-correlation distance, as is the case for all other sampled which have been studied. This is due to the strong alignment of tertiary dendrite arms in this sample, which contribute the curvature at the center of the MCD. The feasibility of adapting the technique to measure spatial correlations only in the x-y plane for use with highly-directional, long coarsening time samples with small z dimensions is shown.

References

[1] H. Jinnai, H. Watashiba, N. Ishizuka, and et. al. Surface curvatures of trabecular bone microarchitecture. *Bone*, 30(1):191–194, 2002.

[2] A. Onuki. *Phase Transition Dynamics*. Cambridge University Press, 2002.

[3] M. Fiałkowski and R. Hołyst. Morphological changes during the order-disorder transition in the two- and three-dimensional systems of scalar nonconserved order parameters. *Phys. Rev. E*, 66:046121, 2002.

[4] O. Hellwig, A. Berger, and E.E. Fullerton. Domain wall in antiferromagnetically coupled multilayer films. *Phys. Rev. Lett.*, 91(19):197203, 2003.

[5] R. Mendoza, I. Savin, K. Thornton, and P.W. Voorhees. Topological complexity and the dynamics of coarsening. *Nature Mater.*, 3(6):385–388, 2004.

[6] J.R. Wilson, W. Kobsiriphat, R. Mendoza, H.Y. Chen, J.M. Hiller, D.J. Miller, K. Thornton, P.W. Voorhees, S.B. Adler, and S.A. Barnett. Three-dimensional reconstruction of a solid-oxide fuel-cell anode. *Nature Mater.*, 5(7):541–544, 2006.

[7] D. Gostovic, J.R. Smith, D.P.Kundinger, K.S. Jones, and E.D. Wachsman. Three-dimensional reconstruction of porous lscf cathodes. *Electrochem. Solid-State Lett.*, 10(12):B214–B217, 2007.

[8] H. Jinnai, H. Watashiba, T. Kajihara, and M. Takahashi. Connectivity and topology of a phase-separating bicontinuous structure in a polymer mixture: Direct measurements of coordination number, inter-junction distances and euler characteristic. *J. Chem. Phys.*, 119(14):7554–7559, 2003.

[9] E. Scholten, L.M.C. Sagis, and E. van der Linden. Coarsening rates of bicontinuous structures in polymer mixtures. *Macromolecules*, 38(1):339–346, 2005.

[10] P. Fratzl and R. Weinkamer. Nature's hierarchical materials. *Prog. Mater. Sci.*, 52:1263–1334, 2007.

[11] G. Yu, J. Gao, J.C. Hummelen, F. Wudl, and A.J. Heeger. Polymer photovoltaic cell - enhanced efficiencies via a network of internal donor-acceptor heterojunctions. *Science*, 270(5243):1789–1791, 1995.

[12] C.W. Tanner, K.Z. Fung, and A.V. Virkar. The effect of porous composite electrode structure on solid oxide fuel cell performance. *J. Electrochem. Soc.*, 144(1):21–30, 1997.

[13] Y. Nishikawa, H. Jinnai, T. Koga, T. Hashimoto, and S.T. Hyde. Measurements of interfacial curvatures of bicontinuous structure from three-dimensional digital images. *Langmuir*, 14:1242–1249, 1998.

[14] D. Kammer and P.W. Voorhees. The morphological evolution of dendritic microstructures during coarsening. *Acta Mater.*, 54:1549–1558, 2006.

[15] R. Mendoza, J. Alkemper, and P.W. Voorhees. The morphological evolution of dendritic microstructures during coarsening. *Metall. Trans. A*, 34:481–489, 2003.

[16] J. Brozovsky and P. Pankaj. Towards modelling of a trabecular bone. *Comput. Struct.*, 85(9):512–517, 2007.

[17] S. Basu, R. Pollack, and M.F. Roy. Computing the euler-poincare characteristics of sign conditions. *Comput. Complex.*, 14(1):53–71, 2005.

[18] O. Krichevsky and J. Stavans. Correlated ostwald ripening in 2 dimensions. *Phys. Rev. Lett.*, 70(10):1473–1476, 1993.

[19] S. Torquato. *Random heterogeneous materials: microstructure and macroscopic properties*. New York:Springer, 2002.

[20] V.A. Snyder, J. Alkemper, and P.W. Voorhees. The development of spatial correlations during ostwald ripening: a test of theory. *Acta Mater.*, 48:2689–2701, 2000.

[21] A.D. Rollett, S.-B. Less, R. Campman, and G.S. Rohrer. Three-dimensional characterization of microstructure by electron back-scatter diffraction. *Annu. Rev. Mater. Research*, 37:627–658, 2007.

[22] S. Yang, A. Tewari, and A.M. Gokhale. Modeling of non-uniform spatial arrangement of fibers in a ceramic matrix composite. *Acta Mater.*, 45(7):3059–3069, 1996.

[23] H. Singh, A.M. Gokhale, Y. Mao, and J.E. Spowart. Computer simulations of realistic microstructures of discontinuously reinforced aluminum alloy (DRA) composites. *Acta Mater.*, 54:2131–2143, 2006.

[24] J.S. Pedersen. Small-angle scattering from precipitates - analysis by use of a polydisperse hard-sphere model. *Phys. Rev. B*, 47(2):657–665, 1993.

[25] P.A. Rikvold and J.D. Gunton. Scaling function for the structure factor in 1st-order phase-transitions. *Phys. Rev. Lett.*, 49(4):286–289, 1982.

[26] W.R. White and Pierre Wiltzius. Real space measurement of structure in phase separating binary fluid mixtures. *Phys. Rev. Lett.*, 75(16):3012–3015, 1995.

[27] N. Akaiwa and P.W. Voorhees. Late-stage pase separations: Dynamics, spatial correlations, and structure functions. *Phys. Rev. E*, 49(5):3860–3880, 1994.

[28] C.W.J. Beenakker. Numerical simulation of diffusion-controlled droplet growth: Dynamical correlation effects. *Phys. Rev. A*, 33(6):4482–4486, 1986.

[29] K.G. Wang, M.E. Glicksman, and C. Lou. Correlations and fluctuations in phase coarsening. *Phys. Rev. E*, 73(6):061502, 2006.

[30] I.M. Lifshitz and V.V. Slyozov. The kinetics of precipitation from superstaurated solid solutions. *J. Phys. Chem. Solids*, 19:35–50, 1961.

[31] C. Wagner. Theorie der alterung von niederschlägen durch umlösen. *Z. Elektrochem.*, 65:581–591, 1961.

[32] A. Papapetrou. Untersuchengen über dendritisches Wachstum von Kristallen. *Z. Kristallogr.*, 92:89–130, 1935.

[33] M. Kahlweit. On the aging of dendrites. *Scr. Metall.*, 2:251–254, 1968.

[34] J.J. Reeves and T.Z. Kattamis. A model for isothermal coarsening. *Scripta Metall.*, 5:223–230, 1971.

[35] M. Chen and T.Z. Kattamis. Dendrite coarsening during directional solidification. *Mater. Sci. Eng., A*, A247:239–247, 1998.

[36] A.A. Chernov. *Kristallografiya*, 1(5):583–587, 1956.

[37] M.O. Klia. *Kristallografiya*, 1(5):576–581, 1956.

[38] D.H. Kirkwood. A simple model for dendrite coarsening during solidification. *J. Mater. Sci. Eng.*, 73:L1–L4, 1985.

[39] K.P. Young and D.H. Kirkwood. The dendrite arm spacings of Aluminum-Copper alloys solidified under steady-state conditions. *Metall. Trans. A*, 6A:197–205, January 1975.

[40] T.Z. Kattamis, J.C. Coughlin, and M.C. Flemings. Influence of coarsening on dendrite arm spacing of Aluminum-Copper alloys. *Trans. Metall. Soc. AIME*, 239:1504–1511, October 1967.

[41] S.P. Marsh and M.E. Glicksman. Overview of geometric effects on coarsening of mushy zones. *Metall. Mater. Trans.*, 27A:557–567, 1996.

[42] T.F. Bower, H.D. Brody, and M.C. Flemings. Measurements of solute redistribution in dendritic solidification. *Trans. Metall. Soc. AIME*, 236:624–634, May 1966.

[43] D. Feijóo and H.E. Exner. Surface curvature distributions of growing dendritic crystals. *J. Cryst. Growth*, 113:449–455, 1991.

[44] D. Feijóo, B. Bauer, and H.E. Exner. Determination of local surface curvature and its frequency distribution by computer-assisted stereometry. *J. Comput. Assist. Microsc.*, 2(1):3–23, 1985.

[45] Y. Kwon, K. Thornton, and P.W. Voorhees. Coarsening of bicontinuous structures via nonconserved and conserved dynamics. *Phys. Rev. E*, 75(2):021120, 2007.

[46] V.A. Snyder, J. Alkemper, and P.W. Voorhees. Transient ostwald ripening and the disagreement between steady-state coarsening theory and experiment. *Acta Mater.*, 49:699–709, 2001.

[47] Yongwoo Kwon. *Morphology and topology of interfaces during coarsening via nonconserved and conserved dynamics*. PhD in materials science and engineering, Northwestern University, 2007.

[48] K. Kawasaki, T. Ohta, and D. Jasnow. Universal scaling in the motion of random interfaces. *Phys. Rev. Lett.*, 49(17):1223–1226, 1982.

[49] D.A. Drew. Evolution of geometric statistics. *SIAM J. Appl. Math*, 50:649–666, 1990.

[50] Y. Kwon, K. Thornton, and P.W. Voorhees. Coarsening of bicontinuous structures via conserved dynamics in asymmetric mixtures. In preparation, 2008.

[51] A.L. Genau and P.W. Voorhees. The morphology of topologically complex interfaces. Submitted, 2008.

[52] S.C. Hardy, G.B. McFadden, S.R. Coriell, P.W. Voorhees, and R.F. Sekerka. Measurement and analysis of grain-boundry grooving by volume diffusion. *J. Cryst. Growth*, 114(3):467–480, 1991.

[53] S. Ohara. Controlled growth of tin dendrites. *Acta Met.*, 15(2):231–236, 1967.

[54] B. Chalmers. Melting and freezing. *Trans. AIME.*, 200:519–532, 1954.

[55] J. Alkemper, V.A. Snyder, N. Akaiwa, and P.W. Voorhees. Dynamics of late-stage phase separation: a test of theory. *Phys. Rev. Lett.*, 82(13):2725–2728, 1998.

[56] Dimitris Kammer. *Three-Dimensional Analysis and Morphological Characterization of Coarsened Dendritic Microstructures*. PhD in materials science and engineering, Northwestern University, 2006.

[57] J. Alkemper and P.W. Voorhees. Quantitative serial sectioning analysis. *J. Microsc.*, 201:388–394, 2001.

[58] D. Kammer, R. Mendoza, and P.W. Voorhees. Cylindrical domain formation in topologically complex structures. *Scripta Mater.*, 55(1):17–22, 2006.

[59] H. Jinnai, T. Koga, Y. Nishikawa, T. Hashimoto, and S. Hyde. Curvature determination of spinodal interface in a condensed matter system. *Phys. Rev. Lett.*, 78(11):2248–2251, 1997.

[60] G. Lavoué, F. Dupont, and A. Baskurt. Constant curvature region decomposition of 3D-meshes by a mixed approach vertex-triangle. *J. WSCG*, 12:245–252, 2004.

[61] J.C. Warner and J.D. Verhoeven. Morphology of tin dendrites in near-eutectic alloys. *Met. Trans.*, 3(4):1001–1002, 1972.